

**Characterization of 308L Stainless Steel Coatings
Fabricated by Laser Cladding**

(レーザークラッド法により作製した 308L ステンレス鋼の
特性評価)

*Department of Mechanical Science and Engineering
Graduate School of Engineering
Hiroshima University, Japan*

Advisor: Prof. Gen Sasaki

LI WENQUAN

CONTENTS

| | |
|------------------------------|------|
| CONTENTS | i |
| List of Figures | v |
| List of Tables | viii |

Chapter 1 Background and Objective

| | |
|---|----|
| 1.1 Introduction..... | 2 |
| 1.2 Laser cladding process..... | 3 |
| 1.2.1 Process Principle..... | 3 |
| 1.2.2 Filling material system..... | 6 |
| 1.2.3 Laser hot wire cladding process..... | 9 |
| 1.2.4 Applications of laser cladding..... | 9 |
| 1.3 Experimental study on laser cladding..... | 11 |
| 1.3.1 Exploration of processing parameters..... | 12 |
| 1.3.2 Geometric shape..... | 14 |
| 1.3.3 microstructure..... | 16 |
| 1.3.4 Mechanical properties..... | 18 |
| 1.4 Study on 308L stainless steel..... | 20 |
| 1.5 Numerical simulation study of laser cladding..... | 21 |
| 1.6 Objective of this thesis..... | 23 |
| 1.7 Outline of this thesis..... | 24 |
| 1.8 References..... | 26 |

Chapter 2 Microstructure Evolution and Mechanical Properties of 308L Stainless Steel Coatings

| | |
|---------------------------------|----|
| 2.1 Introduction..... | 43 |
| 2.2 Experimental procedure..... | 45 |

| | | |
|-------|---|----|
| 2.3 | Results..... | 47 |
| 2.3.1 | Macro-morphologies and microstructures | 47 |
| 2.3.2 | EBSD results..... | 51 |
| 2.3.3 | XRD | 54 |
| 2.3.4 | Mechanical properties..... | 55 |
| 2.4 | Discussion..... | 59 |
| 2.4.1 | Solidification mode..... | 59 |
| 2.4.2 | Detailed grain structures and crystallographic texture..... | 60 |
| 2.5 | Summary..... | 62 |
| 2.6 | References..... | 63 |

Chapter 3 Research on Interface Characteristics of 308L Stainless Steel Coatings

| | | |
|-------|---|----|
| 3.1 | Introduction..... | 69 |
| 3.2 | Material and methods..... | 71 |
| 3.3 | Results | 74 |
| 3.3.1 | Macro morphologies..... | 74 |
| 3.3.2 | Microstructures..... | 74 |
| 3.3.3 | Grain structure and texture..... | 78 |
| 3.3.4 | Chemical Composition Across the Interfaces..... | 84 |
| 3.3.5 | Phase compositions in the HAZ and the first cladding layer..... | 86 |
| 3.3.6 | Microhardness..... | 87 |
| 3.4 | Discussion..... | 89 |
| 3.4.1 | Phase transformations..... | 89 |
| 3.4.2 | The relationship between mechanical properties and microstructural features | 92 |
| 3.4 | Summary..... | 95 |
| 3.5 | References..... | 96 |

Chapter 4 Temperature Field Simulation and Solidification Structure During Laser Hot Wire Cladding Process

| | | |
|-------|---|-----|
| 4.1 | Introduction..... | 103 |
| 4.2 | Finite element modeling..... | 105 |
| 4.2.1 | Heat conduction equation and heat source model..... | 105 |
| 4.2.2 | Laser hot wire cladding process..... | 106 |
| 4.2.3 | Model description..... | 107 |
| 4.2.4 | Laser cladding simulation procedure..... | 107 |
| 4.3 | Results and discussion..... | 108 |
| 4.3.1 | Temperature field simulation results..... | 108 |
| 4.3.2 | Experimentally obtained microstructure..... | 111 |
| 4.3.3 | Crystal orientation..... | 113 |
| 4.4 | Summary..... | 115 |
| 4.5 | References..... | 116 |

Chapter 5 Conclusions

| | |
|---|-----|
| Acknowledgements | 123 |
| Published Papers in Regards to This Thesis..... | 124 |
| Presentations..... | 125 |

List of Figures

Figure 1-1. (a) Schematic diagram of UV-A laser engineered net shaping system set-up; (b) and (c) schematic diagram of 3D view and top view of EC field-assisted LC process; (d) schematic diagram of the underwater LC system; (e) schematic diagram of laser-material interaction in underwater LC process; (f) actual manufacturing process of underwater LC process.

Figure 1-2. Schematic diagrams of the LC processing mode: (a) coaxial powder feeding method; (b) pre-placed powder method; (c) off-axis powder feeding method; (d) wire feeding method

Figure 1-3. TEM images of the CFs distributed in coatings: (a) 3 vol%, (b) 6 vol% and (c)(d) 9 vol%.

Figure 1-4. Comparison between yield strength and density of various materials

Figure 1-5. Parameters of the laser cladding process.

Figure 1-6. The trajectory, temperature, and velocity profile of powder particle flow.

Figure 1-7. The calculation method for dilution rate.

Figure 1-8. The cross section of K403 superalloy coatings with different laser powers. (D, h, H and W denote weld pool depth, coating height, overall height, and coating width, respectively.)

Figure 1-9. Bar chart for microhardness of alloys and clad materials.

Figure 1-10. Variation of wear as a function of normal load at a sliding speed of 0.1 m/s.

Figure 1-11. Polarization curves for laser clad samples in 3.5% NaCl solution.

Figure 1-12. Simulated shape of a bead under the influence of 0.5 kW Gaussian laser beam 0.8 s after the laser was turned on and a structure of metal flows inside the bead.

Figure 1-13. The comparison of microstructure formation of simulation and experimental deposited bead with different inclining angle.

Figure 2-1. Schematic diagram of LHWC experimental device.

Figure 2-2. Schematic diagram of sampling location and size of tensile samples.

Figure 2-3. Macroscopic morphologies of 308 L stainless steel sample with three layers.

Figure 2-4. Microstructures of 308L stainless steel sample with three layers: (a-b) 3rd layer, (c-d) junction line between 2nd and 3rd layer, (e) 2nd layer, (f-g) junction line between 1st and 2nd layer, (h-j) 1st layer, (k) Fusion line, (l) HAZ, and (m) substrate.

Figure 2-5. EBSD maps of 308 L stainless steel sample with three layers: (a) IPF map, (b) grain boundary map, and (c) KAM map

Figure 2-6. Grain size of 308 L stainless steel sample with three layers.

Figure 2-7. XRD patterns of the 308 L stainless steel sample with three layers.

Figure 2-8. Microhardness profile of the 308 L stainless steel sample with three layers.

Figure 2-9. Tensile results of the 308 L stainless steel sample with three layers.

Figure 2-10. Typical tensile test fracture morphologies in different regions: (a) cladding layer, (b) the cladding layer side near the fusion line, (c) HAZ side near the fusion line, and (d) matrix.

Figure 2-11. IPF map, grain boundary map, KAM map and grain size statistical histogram in different regions: (a) central of 1st layer, (b) bottom of 1st layer, (c) HAZ, and (d) matrix.

Figure 2-12. Texture of different regions in the 308 L stainless steel sample with three layers.

Figure 3-1. Schematic diagram of LHWC experimental equipment.

Figure 3-2. (a) Macroscopic morphologies of 308 L stainless steel samples with three layers, (b) dimension of Sample 2.

Figure 3-3. Microstructures of 308 L stainless steel: (a-d) Microstructure under low power microscope, (e-h) Microstructure under high power microscope.

Figure 3-4. Microstructures with different magnifications in different positions of HAZ.

Figure 3-5. Microstructures of substrate material.

Figure 3-6. EBSD maps of the interface: (a) IPF map by LAM, (b), (c), (d) IPF maps of the three regions A, B, and C, (e), (f), and (g) grain boundary maps of the three regions A, B, and C, and (h), (i), (j) KAM maps of the three regions A, B, and C.

Figure 3-7. (a), (b), and (c) Phase maps corresponding to the regions of A, B, and C; (d), (e), and (f) Schematic diagrams of martensite corresponding to the regions of A, B, and C.

Figure 3-8. The pole figures corresponding to the part of the cladding layer in the A, B, and C area.

Figure 3-9. The pole figures corresponding to the part of the HAZ in the A, B, and C area.

Figure 3-10. The grain size distribution map and average grain size map of the A, B, and C region.

Figure 3-11. SEM-EDS line scan distribution of major elements across the interface.

Figure 3-12. The corresponding EDS mappings for (a) Fe, (b) Cr, (c) Mn, and (d) Ni.

Figure 3-13. XRD patterns of the cladding layers and the HAZ in the substrate.

Figure 3-14. Microhardness profile of different areas across the interface.

Figure 3-15. Schaeffler diagram.

Figure 3-16. The inverse pole figures of BCC corresponding to the part of the HAZ in the A, B, and C area.

Figure 3-17. The inverse pole figures of FCC corresponding to the part of the cladding layer in the A, B, and C area.

Figure 4-1. The schematic diagram of LHWC process used in this study.

Figure 4-2. The established three-dimensional finite element model.

Figure 4-3 The schematic diagram of LHWC performed using a stepwise activated approach.

Figure 4-4. Temperature field simulation with different layers.

Figure 4-5. Thermal cycles at specific points of the cross-section.

Figure 4-6. Temperature change during cooling of the first cladding layer.

Figure 4-7. The microstructure of the cladding layers specific area obtained by the experiment.

Figure 4-8. Temperature gradient from edge to the center.

Figure 4-9. Total Euler angle diagram in the cross-section of the three-layer sample.

Figure 4-10. Grain size distribution in the cross-section of the three-layer sample.

List of Tables

Table 1-1. Comparison of surface modification techniques.

Table 1-2. Cladding material systems.

Table 1-3. Some applications of LC.

Table 2-1. Chemical composition of KD-40 substrate and 308L stainless steel wire (wt%).

Table 2-2. Parameters of the experiment settings.

Table 3-1 Chemical composition of 308L wire and KD-40 substrate (wt%).

Table 3-2 Parameters of the experiment settings.

Table 3-3 The grain statistics from the A, B, and C region (μm).

Table 3-4 The calculated yield strength of the regions of A, B, and C (MPa).

Table 4-1 Coefficients for density, specific heat and conductivity of 308L wire and KD-40 substrate.

Table 4-2 Parameters of the heat source model.

Chapter 1

Background and Objective

| | | |
|-------|--|----|
| 1.1 | Introduction..... | 2 |
| 1.2 | Laser cladding process..... | 3 |
| 1.2.1 | Process Principle..... | 3 |
| 1.2.2 | Filling material system..... | 6 |
| 1.2.3 | Laser hot wire cladding process..... | 9 |
| 1.2.4 | Applications of laser cladding | 9 |
| 1.3 | Experimental study on laser cladding..... | 11 |
| 1.3.1 | Exploration of processing parameters..... | 12 |
| 1.3.2 | Geometric shape | 14 |
| 1.3.3 | microstructure | 16 |
| 1.3.4 | Mechanical properties..... | 18 |
| 1.4 | Study on 308L stainless steel..... | 20 |
| 1.5 | Numerical simulation study of laser cladding | 21 |
| 1.6 | Objective of this thesis..... | 23 |
| 1.7 | Outline of this thesis | 24 |
| 1.8 | References..... | 26 |

1.1 Introduction

Low carbon low alloy steel has many advantages, such as good plasticity and toughness, excellent welding performance, and low price, so it is widely used in many engineering fields such as automobiles, rail transportation, bridges, etc.^[1-3]. However, with industry development, the application of mild steel has gradually expanded to corrosive and abrasive environments. The disadvantages of poor wear resistance and corrosion resistance limit mild steel application in these fields. To solve this problem, researchers have developed various surface treatment processes, such as vapor deposition(VD)^[4, 5], carburizing^[6], surfacing^[7], plasma spraying^[8], etc.

In recent years, the global countries have vigorously promoted "carbon neutrality", actively advocating the green development of the manufacturing industry and sustainable development^[9-11]. Laser cladding (LC), as a new high efficiency and low pollution "green" coating preparation technology, has been developing continuously since its introduction in the 1970s and has been applied in many industries^[12-14]. LC can significantly improve the wear resistance, corrosion resistance, heat resistance, oxidation resistance, or electrical properties of the surface of the base material, thus achieving surface modification or repair, meeting the specific performance requirements of the material surface while saving a lot of material costs^[15-17]. A comparison of the characteristics of LC and other surface strengthening processes is shown in Table 1-1. Compared to surface strengthening processes such as surfacing and vapor deposition, LC has the following advantages: (1) small dilution of the clad layer with a dense organization; (2) metallurgical bonding properties between the coating and the substrate; (3) finer microstructure and good comprehensive mechanical properties; (4) more materials suitable for cladding, high material utilization, energy-saving, and environmental protection, etc.^[18, 19]. Therefore, LC has an increasingly wide range of research and applications in preparing high-performance coatings and additive manufacturing of complex structural metal parts^[20-23].

Table 1-1. Comparison of surface modification techniques^[24].

| Characteristic | LC | Welding | Thermal spray | Ion implantation | VD |
|---------------------------|---------------------------|-------------|---------------|------------------------|------------------------|
| Bonding strength | High | High | Moderate | High | Low |
| Dilution | High | High | Moderate | Low | Nil |
| Thickness | 50 μm ~2 mm | ≥ 1 mm | 0.1–0.5 mm | ≤ 1 μm | 0.05 ~10 μm |
| Repeatability | Moderate~ High | Moderate | Moderate | Moderate | High |
| Heat-affected zone | Low | High | High | Low | Low |
| Controllability | High | Low | Moderate | Moderate | Moderate |
| Cost | High | Moderate | Moderate | Moderate | High |

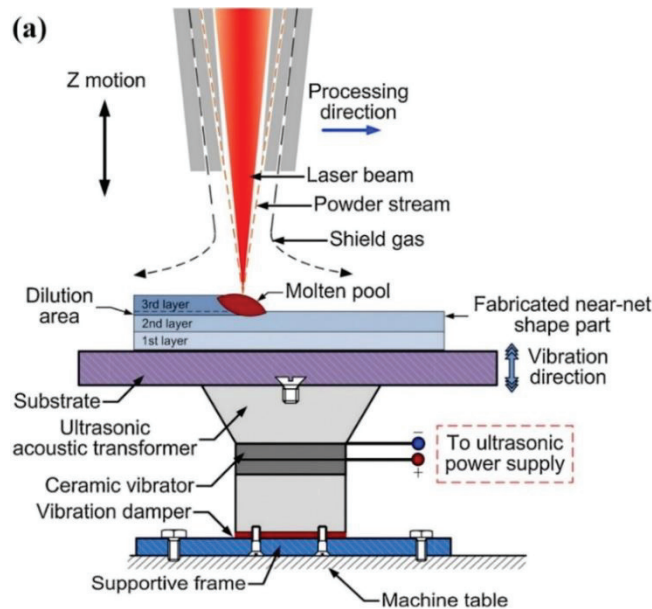
As one of the pillar materials of modern industry, stainless steel has become an indispensable material in modern industry and engineering construction by its high corrosion and heat resistance, high strength, high hardness, etc. It plays an important role in automotive, chemical, catering, construction, nuclear power, medical, etc. With its excellent mechanical properties and corrosion resistance, the 308L stainless steel is widely used in oil, gas, shipbuilding, mining, and other fields^[25]. Using the 308L stainless steel as the coating material, the laser melting process to improve the wear resistance and corrosion resistance of mild steel is of great significance in extending the application range of mild steel and enhancing the material life.

1.2 Laser cladding process

1.2.1 Process Principle

Laser cladding is a process in which an external material is added to the molten pool formed by laser irradiation of the substrate through simultaneous or pre-set material. The two are rapidly solidified together to form a cladding layer^[26, 27]. There are four common ways of adding cladding materials: coaxial powder feeding, pre-

placed powder, off-axis powder feeding, and wire feeding methods^[28-31], as shown in Fig. 1-1. In the coaxial powder feeding and off-axis powder feeding system, the powder is delivered to the substrate by the powder feeding system. The laser irradiates the substrate to form a molten pool, as shown in Fig. 1-1a and c. The powder is placed on the substrate in advance in the pre-placed powder system, as shown in Fig. 1-1b. Transferring the wire to the substrate surface and forming a molten pool after laser irradiation is called the wire feeding method, as shown in Fig. 1-1d. During solidification of the molten pool, the surface tension coefficient increases as the temperature decreases, i.e., a surface tension gradient is created between the center of the pool and the edge that drives the fluid flow. This fluid flow is called Marangoni flow^[30, 32]. LC processing methods have gained great attention in recent years, with innovations based on the original process and an ever-expanding range of applications. In 2017, researchers successfully developed ultra-high-speed LC technology to improve production efficiency while reducing costs^[33]. In addition, researchers introduced external physical fields such as ultrasonic vibration (UV), electromagnetic compound (EC), and underwater process into the LC process to improve its quality and expand its application^[34-38], as shown in Fig. 1-2.



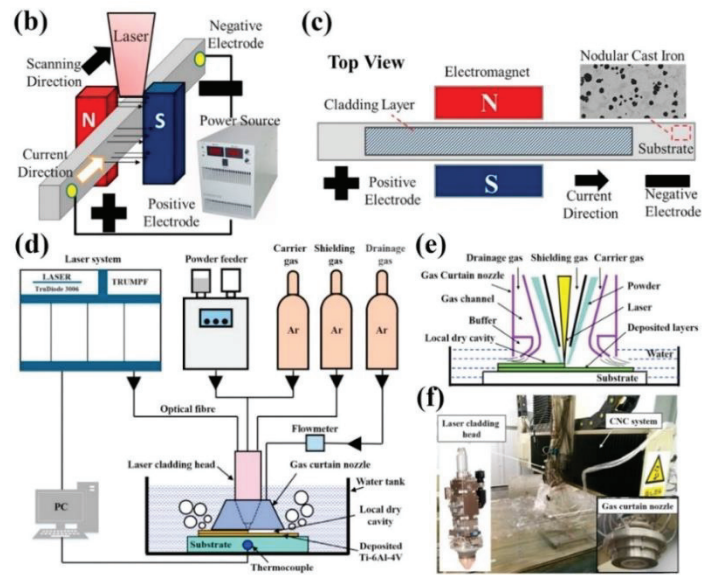


Figure 1-1. (a) Schematic diagram of UV-A laser engineered net shaping system set-up; (b) and (c) schematic diagram of 3D view and top view of EC field-assisted LC process; (d) schematic diagram of the underwater LC system; (e) schematic diagram of laser-material interaction in underwater LC process; (f) actual manufacturing process of underwater LC process^[34-38].

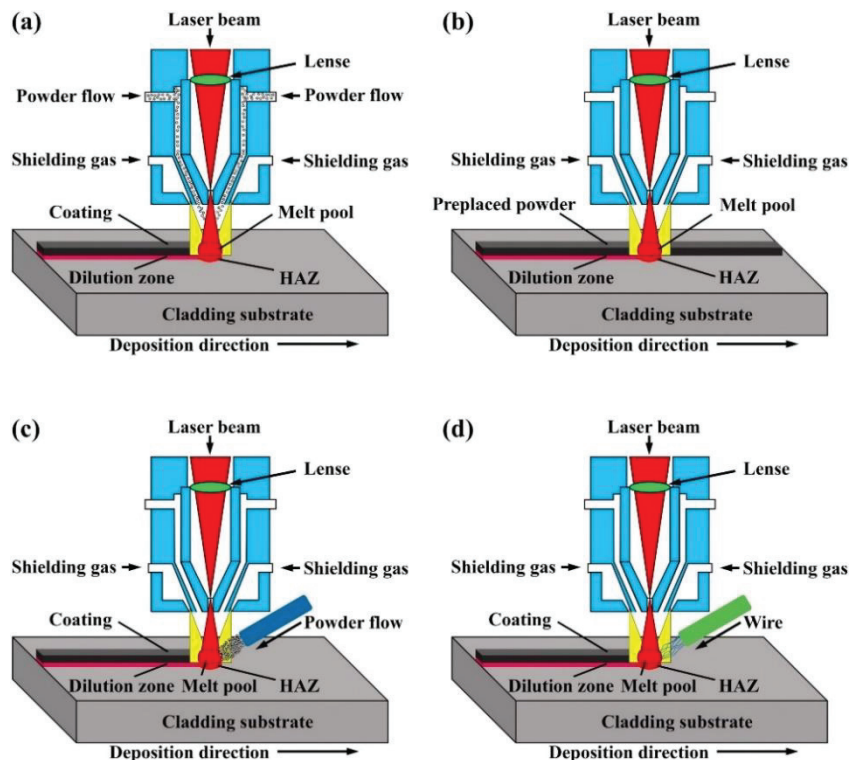


Figure 1-2. Schematic diagrams of the LC processing mode: (a) coaxial powder feeding method; (b) pre-placed powder method; (c) off-axis powder feeding method; (d) wire feeding method^[24].

1.2.2 Filling material system

Currently, the powder is widely used as a cladding material. The advantage of powder materials is a large range of materials to choose from. Alloy powder systems, composite systems, high-entropy alloy systems, and ceramic additive systems have been used in the laser cladding process. The properties of these materials are shown in Table 1-2^[39-42].

Table 1-2. Cladding material systems^[39, 40, 42].

| Type | Advantages | Disadvantages |
|----------------------------------|---|--------------------------------|
| Ni-based | Good toughness, great heat and oxidation resistance, and high corrosion resistance | Poor high-temperature property |
| Co-based | Good high-temperature resistance, excellent heat resistance, excellent wear, and corrosion resistance | High cost |
| Fe-based | Low cost | Poor oxidation resistance |
| Composite materials | Wide application scope and excellent properties | Complex analysis |
| High-entropy alloy | Simple phase structure and excellent properties | Complex chemical composition |
| Rare earth oxide additive | Excellent fine grain strengthening effect | Difficult content control |

Single metal or alloy powder is the most commonly used filler material for powder laser cladding. Common alloy powders include iron-based, nickel-based, cobalt-based self-fluxing alloy powders^[43, 44]. Nickel-based composite coatings prepared on titanium alloy substrates can effectively improve the hardness and wear resistance of the substrate, thus strengthening the substrate^[45]. Iron-base alloy powder is widely used in low carbon steel and cast iron surface strengthening due to its low cost and good wear resistance^[46, 47]. Cobalt-based alloy powder is used a lot in high-temperature environments because of its excellent wear resistance and resistance to high-temperature oxidation^[48].

Metal matrix composites have been widely used in the laser cladding process due to their high strength and wear resistance^[49]. Two types of reinforcing phases are

commonly used for metal matrix composites, ceramic particle reinforced phases such as vanadium carbide (VC), titanium carbide (TiC), and tungsten carbide (WC)^[50, 51], and fiber-reinforced phases such as carbon fibers^[52]. Zhang et al.^[53] prepared metal matrix composite coatings on low carbon steel A36 composed of VC, TiC, and WC mixed with AISI 420 stainless steel powder, respectively. The erosion resistance of the coating at different angles was investigated. The results showed that the VC-reinforced coating exhibited the best erosion resistance at all impact angles for all coatings. Due to its special physical properties, carbon fiber is mainly used to reduce the friction coefficient of the coating. Shi et al.^[54] investigated the effect of the content of carbon fibers on the mechanical properties of the molten cladding layer, as shown in Fig. 1-3. It is shown that when the carbon fiber content is 6 vol%, the carbon fiber has the most uniform distribution in the cladding layer and the highest microhardness and tensile strength. Too much or too little carbon fiber has a negative effect on the performance of the cladding layer.

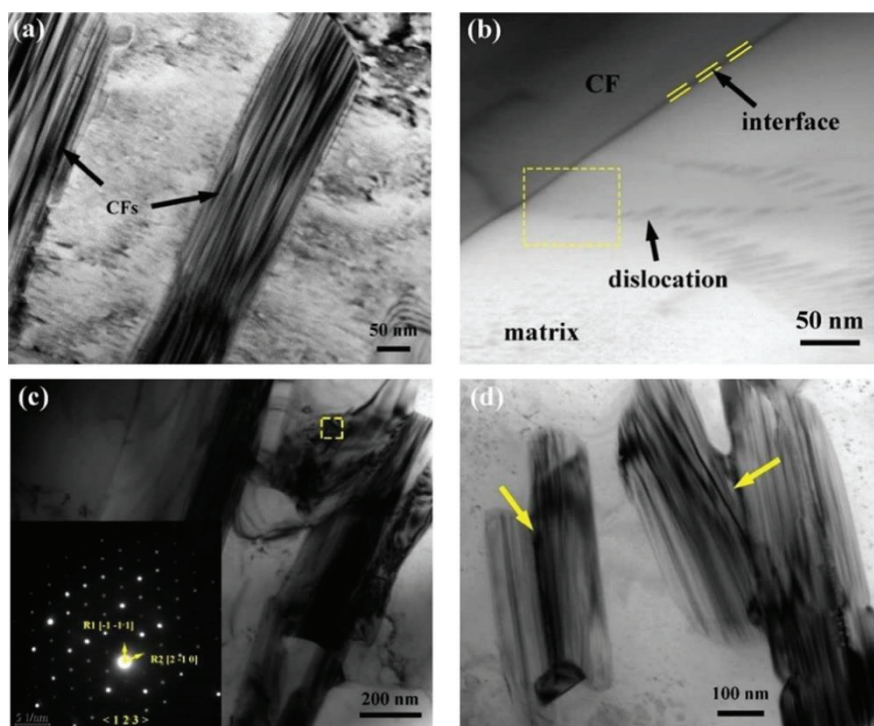


Figure 1-3. TEM images of the CFs distributed in coatings^[54]: (a) 3 vol%, (b) 6 vol% and (c)(d) 9 vol%.

High-entropy alloys (HEA) are alloys formed from five or more metals in equal or approximately equal amounts. HEAs are highly valued in materials science and

engineering because of their unique composition, microstructure, and tunable properties, which may have many desirable properties^[55]. A comparison of specific strength and density of various materials is shown in Fig. 1-4^[56]. Compared to stainless steel, HEA has a higher yield strength at a similar density and greater application potential. HEA material has been widely used in laser cladding technology, and many studies have shown that HEA material can improve the hardness, wear-resistance, and corrosion resistance of substrate^[57-62]. An important reason for this enhancement is the supersaturated solid solution reinforced phases with lattice distortion in the HEA coatings prepared using laser cladding. Due to the late start of research on laser cladding technology for preparing HEA coatings, the relevant results are still in development. In addition, related process parameters, such as laser power, scanning speed, spot diameter, etc., are still in the exploration and optimization stage, and there is still much room for future research.

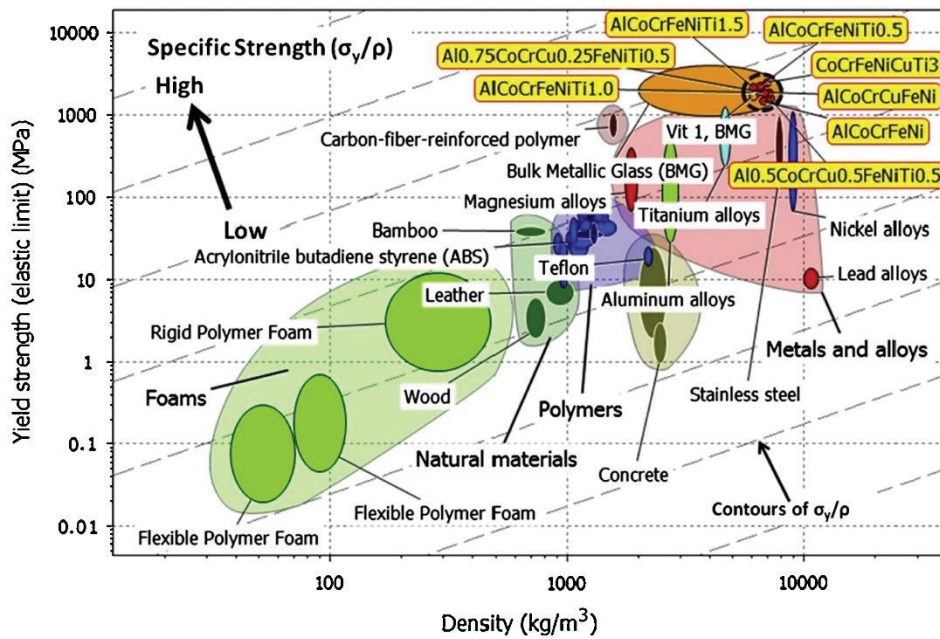


Figure 1-4. Comparison between yield strength and density of various materials^[56].

1.2.3 Laser hot wire cladding process

Although powder has been widely used as a cladding material, some disadvantages of powder materials, such as low material utilization and low deposition efficiency, have limited their application in industry. To meet the demands of rapid industrial development, it is necessary to improve material utilization and efficiency. Laser wire cladding is widely used due to the advantages of high material utilization, high cladding efficiency, no dust pollution, good metallurgical bonding performance, low surface roughness, good stability, etc.^[63-66]. Studies have shown that the material utilization rate of laser wire cladding is close to 100%, while the utilization rate of powder material is only 40-60 wt%^[67, 68]. The deposition efficiency of laser cladding is related to the heat input, and the limited laser power limits the deposition efficiency. To further improve the deposition efficiency, the researchers developed the laser hot wire cladding (LHWC) process^[69]. Compared with LWC, LHWC adds a resistance heating device for heating the wire. The preheated wire can be melted quickly after laser irradiation, greatly improving the wire feeding speed and thus the deposition efficiency^[70]. It has been shown^[71] that laser hot wire cladding can improve efficiency while ensuring the quality of the cladding.

The researchers compared the effects of cold wire, hot wire, and powder material on the laser cladding process. They found that the laser energy is mainly used to form a molten pool in the substrate, and the heat input to the laser cladding process is mainly from the resistant heat. With the help of resistance heat, the deposition efficiency of LHWC can be increased by up to 4 times^[72]. Many researchers have investigated the position, orientation, and angle of the wire and the process parameters for various materials to produce reliable laser cladding products using various materials^[73, 74].

1.2.4 Applications of laser cladding

The current application of laser cladding is mainly used in three aspects: First, the surface modification of materials, such as combustion turbine blades, rolls, gears, etc.^[75-77]; Second, the surface repair of products, such as rotors, molds, etc.^[78-80]. The

information shows that the strength of the repaired parts can reach more than 90% of the original strength, and the repair cost is less than 1/5 of the replacement price. More importantly, it shortens the maintenance time and solves the rapid repair of rotating parts that must be solved for the continuous and reliable operation of major sets of equipment in large enterprises^[76, 81, 82]. In addition, the surface of key components can be laser coated with super wear-resistant corrosion-resistant alloy, which can greatly improve the service life of the components without deforming the surface of the components; Laser cladding of mold surfaces not only improves mold strength but also reduces manufacturing costs by 2/3 and shortens manufacturing cycle time by 4/5^[63-65]. For some special parts, the researchers have also developed an in situ-based repair technique^[83]. The third is laser additive manufacturing. By feeding powder or wire, laser coating is performed layer by layer to obtain parts with a three-dimensional structure^[84-87]. This technology can also be called laser fusion deposition, laser metal deposition, and direct fusion deposition. Table 1-3 lists some of the applications of LC.

Table 1-3. Some applications of LC^[88-92].

| Clad/Alloy and Substrate materials | Application | Reason for Development |
|--|--|--|
| CMSX-4 (Ni-based superalloy) | Repairing of turbine blades | Formation of monocrystalline CMSX-4 |
| Stellite-6/WC on B27 boron steel substrate | Repairing of tools used in soil cultivation. | Enhanced wear resistance due to the formation of intermetallic compounds |
| Ni40 and Ni60 on C60 steel substrate | Upgrading of a barrel-screw system used in plastic injection molding | Improvement in microhardness due to Ni. |
| CPM9V steel on H13 tool steel substrate | Repairing of molds and dies employed in hot and cold working | Formation of the martensite phase induced compressive stresses. |
| Grade C wheel U75V rail with 316L, 420, 410 | Repairing of railway wheels | Increased hardness of the clad materials reduced wear. |
| Titanium hydroxyapatite on Nitinol substrate | Replacement for natural bone | Nickel release reduction using hydroxyapatite coating. |

| Clad/Alloy and Substrate materials | Application | Reason for Development |
|--------------------------------------|---|--|
| Mg-Zn-Dy alloy cast and laser melted | Improved tissue integration of implants | Enhancement in vitro degradation owing to creation of insoluble protective layer. |
| Co29Cr9W3Cu alloy | SLM is used to develop Co29Cr9W3Cu alloy joint prostheses | The beginning of a crack is checked due to plastic deformation by the strain-induced martensitic transformation. |
| Ti powder on the Ti6Al4V | Biocompatibility improvement of Ti deposits for medical implants. | The in vitro test in Hank's solution confirmed that leaching was inside the preferred values. |

1.3 Experimental study on laser cladding

Researchers have comprehensively investigated the process parameters of the laser cladding process through experiments to gain a comprehensive understanding of the laser cladding process. The processing parameters are mainly inputs and processes, such as laser power, feeding system, environmental characteristics, etc.; outputs are some parameters that reflect the machining quality and product performance, such as geometry, microstructure, mechanical properties etc., as shown in Fig. 1-5.

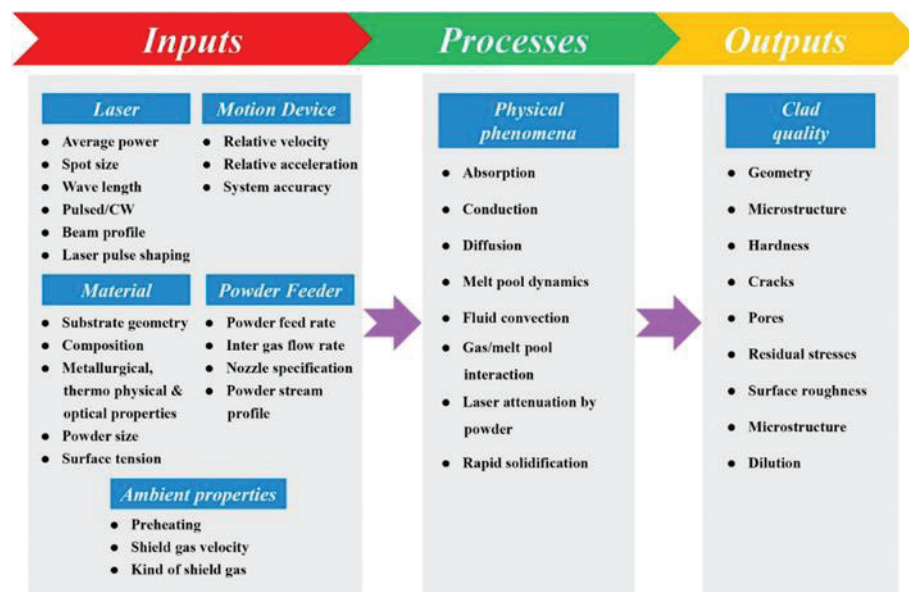


Figure 1-5. Parameters of the laser cladding process^[93].

1.3.1 Exploration of processing parameters

Several parameters are involved in the laser hot wire cladding process. Some are related to the laser energy and resistive heat, while others are related to the wire filling. Shuang et al.^[68, 94] investigated the stability of Inconel 625 alloy wire during LHWC using a spectrometer. The range of energy required in the LHWC process was determined by varying the voltage, and finally, the appropriate process parameters were determined. The authors believe that the applied energy should ideally allow the wire to be heated to a temperature close to the melting point, which will ensure that the wire can be melted quickly upon contact with the laser. Wen et al.^[81, 95] summarized the effects of various parameters on the cladding layer's quality and explored the optimal process parameters. The testing and discussion of the microstructure and mechanical properties of the cladding layer proved its reliable quality. Zhang et al.^[70] monitored the LHWC process using a CMOS high-speed camera, investigated the relationship between wire feeding speed and the resistance heat applied to the wire, and discussed the effect of process parameters on geometric parameters such as melt pool width and length. The study of S. Nowotny et al.^[96] showed that the deposition efficiency can be effectively improved by increasing the resistance heat. The functional relationship between the process parameters and the cladding layer geometry was clarified, which indicated that the process parameters related to energy directly influence the cladding layer geometry. Yamamoto et al.^[97] investigated the effects of wire feeding speed, laser spot diameter, and resistive thermal energy on the properties of the cladding layer. Good morphology of the cladding layer was obtained when the wire was heated to the proper temperature.

With the rapid development of computer and sensing technology, more and more researchers have begun to use computer technology to monitor the temperature field, molten pool shape, and the interaction process between powder and laser. Methods such as Taguchi Method and Response surface method were successively developed to optimize the process parameters. To obtain the best shape and quality of the cladding layer^[98-101]. Gulyaev et al.^[102] investigated the effect of transport gas flow rate on the

motion of powder jets using an optical diagnostic system. The dynamics of particle heating in the laser radiation field were analyzed. The possibility of modern optical diagnostic systems for studying physical phenomena in direct laser deposition was demonstrated, as shown in Fig. 1-6.

It can be seen from the above research that the process parameters have a significant effect on product performance. Therefore, before any formal experiment, exploratory experiments are conducted to determine the optimal process parameters by optimizing laser power, angle, and wire feeding speed.

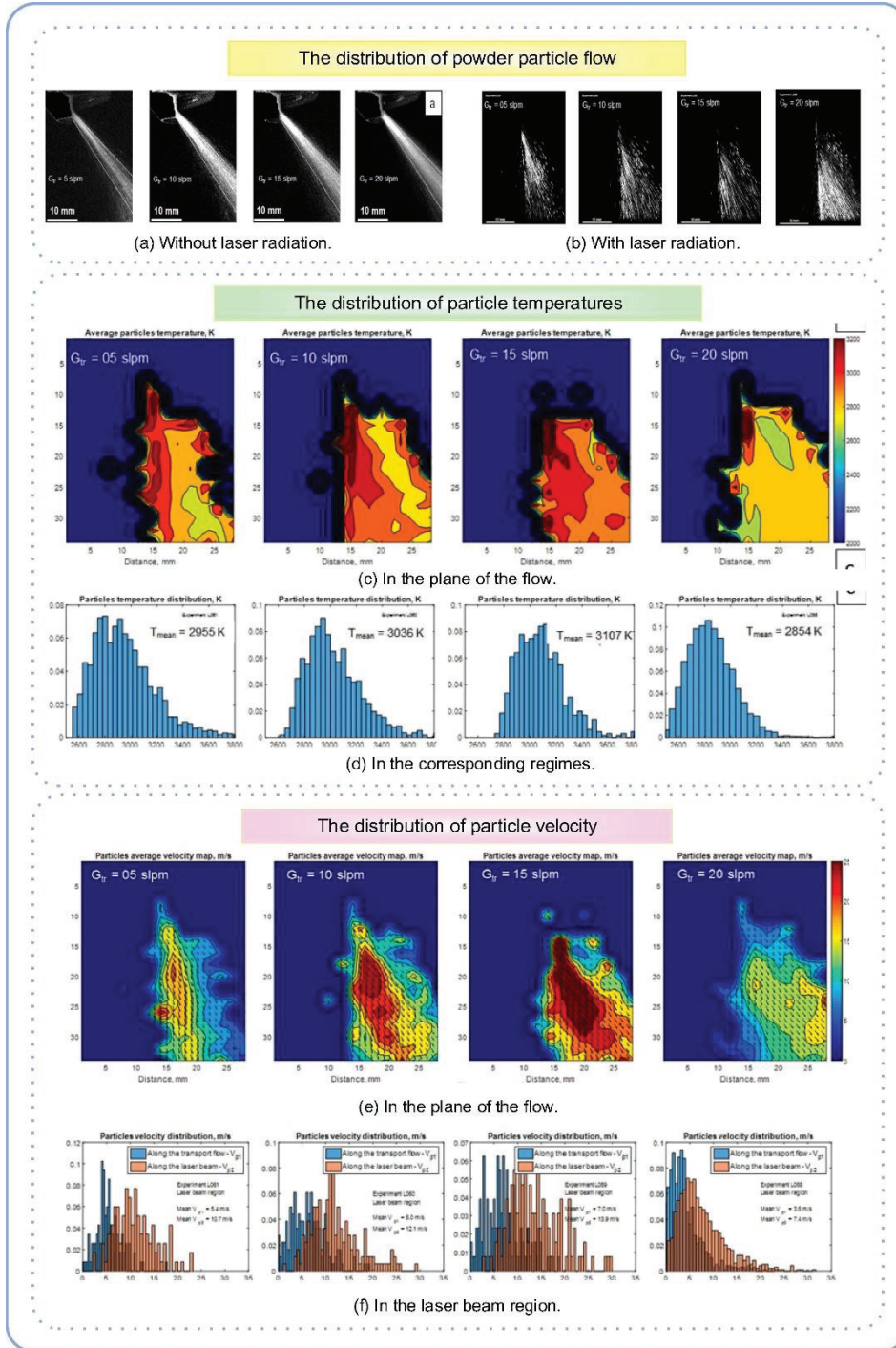


Figure 1-6. The trajectory, temperature, and velocity profile of powder particle flow [82].

1.3.2 Geometric shape

Some geometric parameters such as Dilution Rate (DR), Aspect Ratio (AR), and Clad Angle (CA) can be calculated based on the sample size of the cladding layer. These are some of the indicators to evaluate the quality of the cladding.

DR is an indicator to evaluate the mixing degree between the cladding layer and substrate, and the calculation method is shown in Fig. 1-7. The research of Harooni et al.^[103] showed that DR increases with increasing unit laser energy. Morville et al.^[104] demonstrated that DR was affected by many factors by simulating the deposition process of laser cladding. The increase of laser power, the increase of scanning speed, and the decrease of powder feeding speed all increased the value of DR. Other researchers found that DR would decrease if the composite electromagnetic field was used during laser cladding^[105-108].

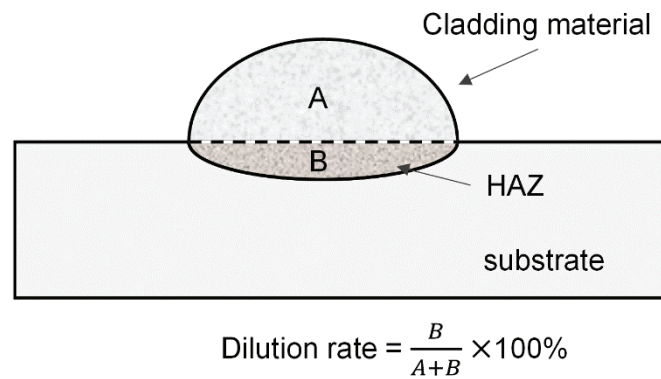


Figure 1-7 The calculation method for dilution rate.

AR can reflect the distribution of coating in the direction of height. The value of AR is not suitable, either too high or too low. Too high will lead to the insufficient height of the cladding layer and affect the processing efficiency; too low will reduce the bonding strength of the cladding layer and the substrate. The AR is calculated as follows^[109]:

$$AR = w/h \quad (1-1)$$

Where w is width, h is height. The research of Riquelme et al.^[110] proved that increasing laser power and scanning speed will increase AR. The higher the input laser energy, the wider the width of the cladding layer when other conditions are constant. If the laser energy per unit area decreases due to changes in other factors (such as increasing the amount of powder fed), the AR will decrease.

CA is the angle between the substrate and the cladding layer and is used to evaluate the size of porosity in the clad layer. The calculation of CA is shown below:

$$CA = 180 - 2 \tan^{-1} \left(\frac{2h}{w} \right) \quad (1-2)$$

Where w is width, h is height. Harooni et al.^[111] studied the relationship between CA and porosity. They found that porosity is lower in multilayer cladding layers if CA is greater than 100° . On the other hand, RA increases with increasing laser scanning speed and decreases with powder delivery speed. Similar conclusions have been obtained by other researchers^[112, 113].

1.3.3 microstructure

The microstructure is an important indicator of product performance. The temperature gradient (G) and the solidification rate (R) are the key factors that determine the microstructure^[114-116]. When G/R is large, the microstructure is dominated by planar crystals. As G decreases and R increases, the microstructure shifts from planar crystals to columnar crystals. When G/R is small, the formation of an equiaxed dendritic structure is favored. Muvvala et al.^[29] found that the laser scanning speed and cooling rate significantly affected the microstructure of the molten layer. In addition, they observed that the pulsed and continuous laser modes also have important effects on the microstructure. The microstructure in continuous laser mode has obvious directionality, while the directionality of the microstructure in pulsed laser mode is not obvious.

Laser power is another important parameter that affects the microstructure. Proper laser power can reduce the generation of cracks and voids and improve the quality of the cladding layer. Choosing too high or too low laser power will affect the quality of the cladding layer. Song et al.^[117] studied the influence of laser power on the microstructure of the cladding layer, as shown in Fig. 1-8. It can be seen from the figure that both the height and width of the cladding layer increase with the increase of laser power. Grain size and crystal type also vary with the laser power—the higher the laser power, the slower the cooling rate, which leads to larger grain sizes.

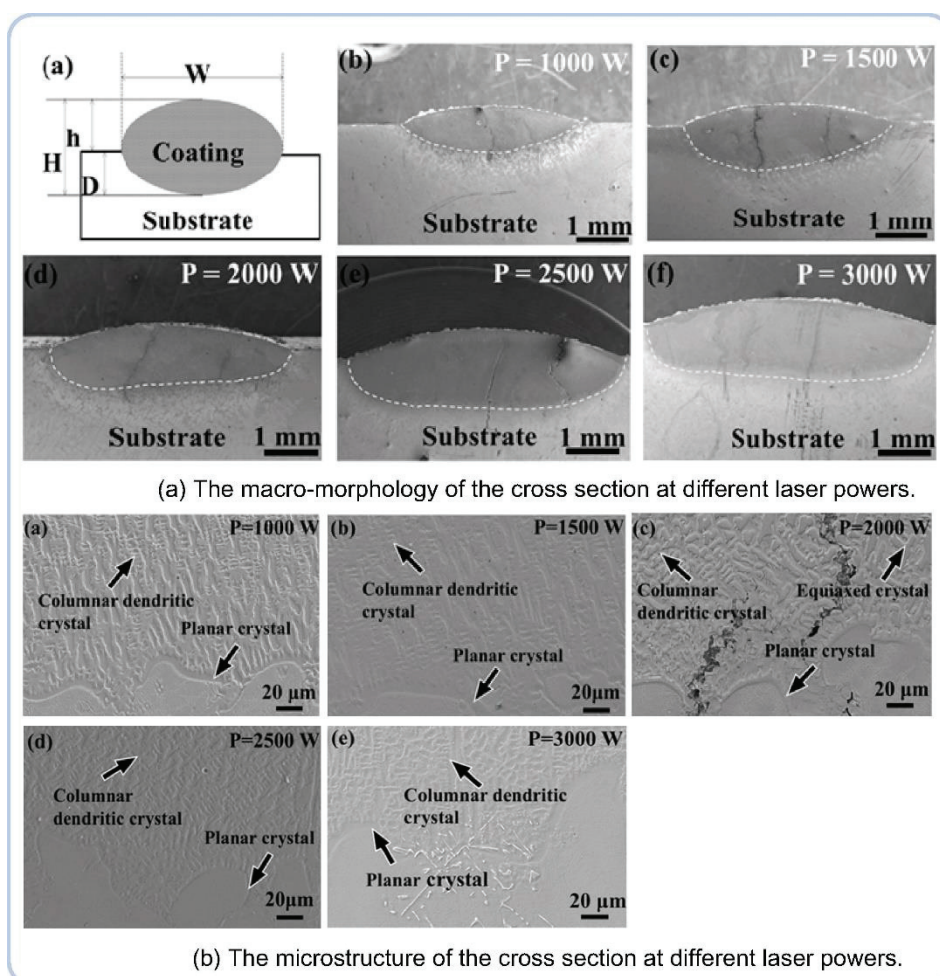


Figure 1-8. The cross section of K403 superalloy coatings with different laser powers ^[96]. (D , h , H and W denote weld pool depth, coating height, overall height, and coating width, respectively.)

The laser scanning speed also affects the microstructure. Yi et al.^[118] John found that reducing the laser scanning speed resulted in finer graphite structures. This is due to the higher heat of the low scan rate, which accelerates the diffusion of the elemental carbon.

Many factors influence microstructure, and they do not act independently but together as a whole. Therefore, it is necessary to obtain the optimal combination of process parameters by various optimization algorithms and empirical formulas. Yu et al.^[119] used Taguchi-gray correlation analysis to optimize the processing parameters of laser power, scanning speed, and powder feeding speed. The best combination of process parameters that can achieve the maximum melt width, minimum melt height, and appropriate dilution rate was found. Bax et al.^[120] offered guidelines to evaluate process parameter maps for single tracks. This method established the relationship

between the process parameters and the geometrical characteristics of the cladding layer and can quantify the shape of a single orbit. Reddy et al.^[121] established a model between process parameters and product quality and verified it through experiments, proving the reliability of this model.

1.3.4 Mechanical properties

Conventional materials usually have a short service life in harsh environments due to the limitations of their mechanical properties. Therefore, the surface needs to be strengthened by other means to enhance the performance. The laser cladding process is an effective surface strengthening process. Laser cladding can significantly improve the hardness, corrosion resistance, wear resistance, oxidation resistance, and other properties of the substrate^[92, 122, 123]. Labban et al.^[124] obtained higher hardness coatings on tool steel surfaces using VC powder due to the reinforcing effect of uniformly distributed VC particles. Xiang et al.^[125] prepared a high-entropy alloy coating on a pure titanium substrate and characterized and analyzed the microstructure and microhardness of the coating. It was shown that the hardness of the coating reached 8.3 times that of the substrate after the addition of Nb, which is the result of the combination of solid solution strengthening, fine grain strengthening, and the Laves phase with fine lamellar morphology. Gao et al.^[126] observed and studied the solidification behavior of coating. The results showed that the cooling rate could significantly affect the properties of laser cladding coating. Previous studies^[127-130] have shown that the laser cladding process has a significant effect on the hardness of the substrate, as shown in Fig. 1-9. Guo et al.^[131] prepared HfB₂/Ni based composite coating on a titanium substrate to study the wear resistance of the composite coating. The wear amount is shown in Fig. 1-10^[131]. The results show that the wear resistance of HfB₂ clad coatings can reach 200 times that of the substrate. Study shows that HfB₂/Ni based composite coating enhances the wear resistance of different materials^[132-135]. Corrosion resistance is also an important indicator to evaluate the material's performance, which reflects the material's ability to resist oxidation. Nabhani et al. prepared Ti6Al4V coatings at different laser

powers, and it was clear from the measurements that the rapid solidification of the martensite and coaxial phases formed in the coatings improved the corrosion resistance of the laser-fused samples, and the polarization curves are shown in Fig. 1-11^[136].

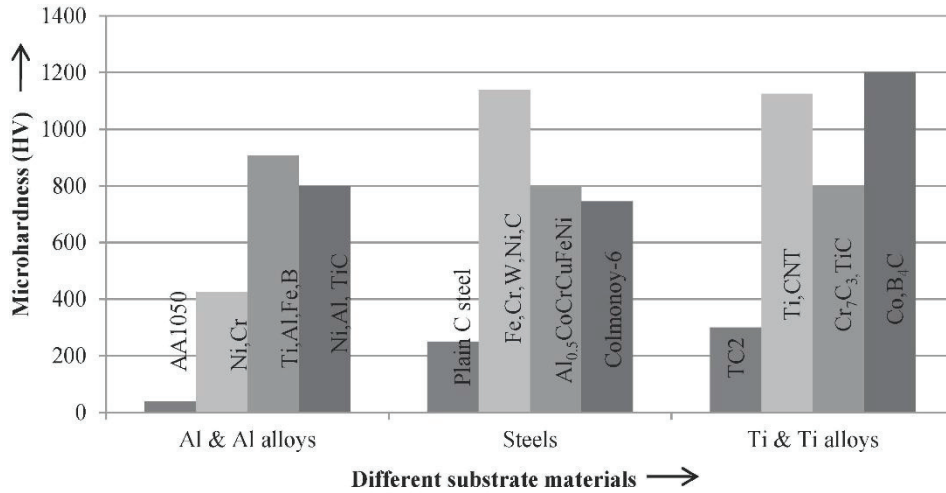


Figure 1-9. Bar chart for microhardness of alloys and clad materials.

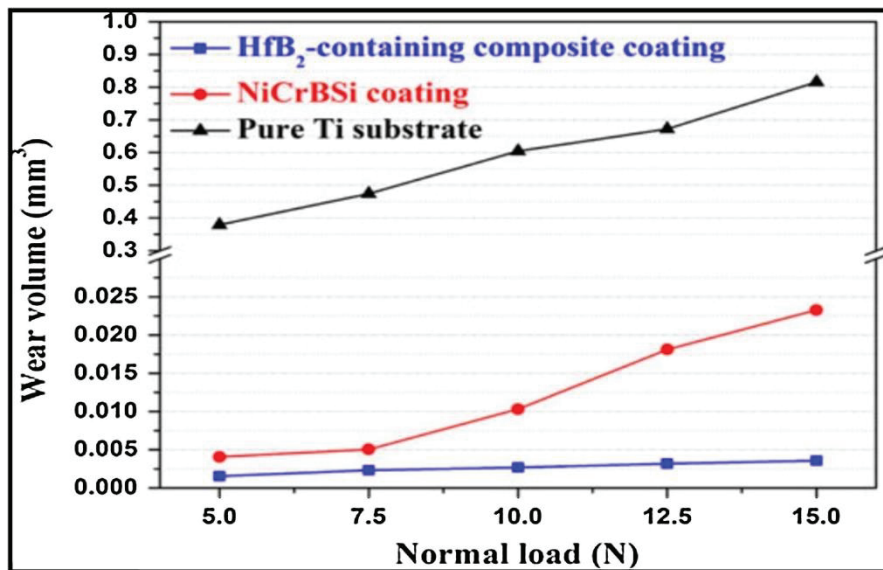


Figure 1-10. Variation of wear as a function of normal load at a sliding speed of 0.1 m/s.

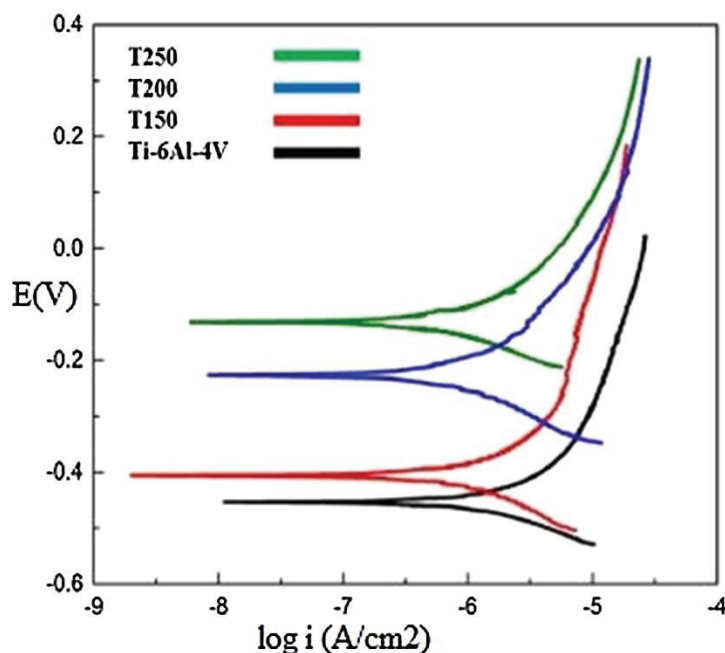


Figure 1-11. Polarization curves for laser clad samples in 3.5% NaCl solution^[136].

1.4 Study on 308L stainless steel

In previous studies, stainless steel materials used for laser cladding coating are mainly 316L stainless steel and 304 stainless steel^[137-139], and 308L has been less studied. 308L stainless steel is an austenitic stainless steel with low carbon content, high mechanical properties, and high corrosion resistance, which is used in the gas, oil, automotive and marine industries. Yilmaz and Uglu^[140] reported the effect of processing parameters on the microstructure of 308L molten cladding layers. Their study showed that travel speed significantly affected the texture and grain size of residual ferrite; grain size was mainly affected by wire feeding speed. Abioye et al.^[141] prepared multilayer 308L stainless steel cladding layer using laser wire deposition technology, and the microstructure of the cladding layer was columnar dendrites growing along the construction direction. Li et al.^[79] showed that the microstructure differs in different locations, with the bottom and middle parts consisting mainly of columnar dendrites and the top part consisting of equiaxed crystals. Le et al.^[142] investigated the effect of cooling methods (natural and active cooling) on coatings' shape, organization, and properties. The study showed that active cooling was an effective way to improve the

quality and productivity of the parts.

1.5 Numerical simulation study of laser cladding

The distribution of temperature and flow fields during the laser cladding process has an important influence on the cladding layer's macrostructure, microstructure, and mechanical properties^[143-145]. It is difficult to directly observe the temperature and flow field changes during the laser cladding process by the existing technical method. Therefore, using numerical simulation techniques to simulate the laser cladding process is important to optimize the process parameters in the laser cladding process^[146, 147].

At present, many researchers have simulated the deposition process, temperature field, stress field, and microstructure of the cladding layer based on fluid dynamics and physical phase-field processes^[148, 149]. Khamidullin et al.^[150] simulated the laser melting process using a two-dimensional finite element model to obtain the distribution of temperature and flow fields, as shown in Fig. 1-12 and 1-13. The simulation results show that the distribution of temperature, flow, and velocity fields are visible, which clearly and intuitively predicts the formation process of the cladding layer. Liu et al.^[151] simulated the effect of the coaxial nozzle and scanning direction angle variation on the macroscopic size of the melt pool and microstructure of the cladding layer. The results showed that the height of the clad layer decreased as the nozzle tilt angle was raised, and the experimental results verified this.

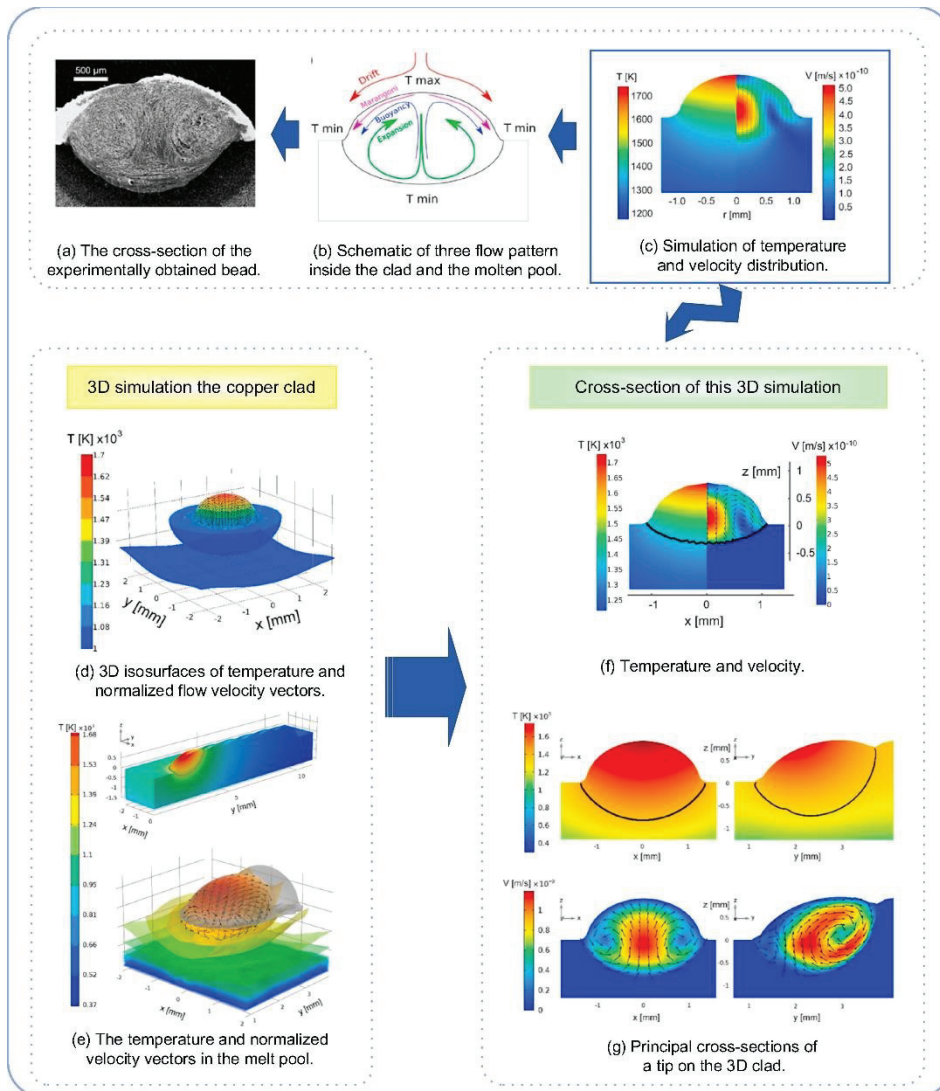


Figure 1-12. Simulated shape of a bead under the influence of 0.5 kW Gaussian laser beam 0.8 s after the laser was turned on and a structure of metal flows inside the bead [150].

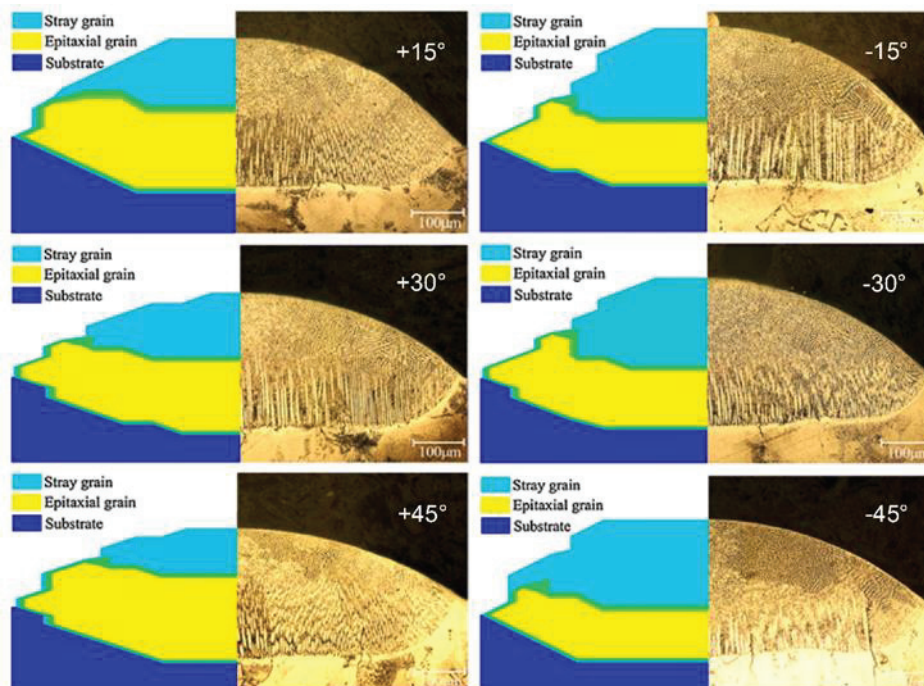


Figure 1-13. The comparison of microstructure formation of simulation and experimental deposited bead with different inclining angle^[150].

1.6 Objective of this thesis

Laser hot wire cladding (LHWC) has proven to be a very efficient laser cladding manufacturing process with the advantages of fast deposition speed, high material utilization, and no environmental pollution. 308L stainless steel is widely used in petroleum, natural gas, shipbuilding, mining, and other fields owing to its excellent mechanical properties and corrosion resistance. Most current research on LHWC technology to prepare stainless steel coatings mainly focuses on optimizing the process parameters during the preparation process. Although there have been studies on the microstructure and mechanical properties, few studies have been conducted on the microstructure and performance of the matrix and the HAZ. There is also a lack of systematic research on the bonding properties of heterogeneous materials in laser cladding processes.

However, in practical applications, the substrate and cladding layer are applied as a whole, so it is not enough to study only the cladding layer, especially when the

substrate and the cladding layer are different materials, the combination of the substrate and the cladding layer is also very important. To comprehensively analyze the laser welding process, it is needed to study not only the cladding layer, but also the bonding process of the matrix and the cladding layer. It is necessary to characterize the microstructure and properties of each region separately, including the matrix, HAZ, and the cladding layer. These regions are then combined to completely characterize the microstructure evolution and mechanical properties of the products prepared using LHWC technology.

In this study, multi-layer 308L stainless steel samples were prepared using the LHWC technique. To comprehensively evaluate the samples, OM, EBSD, and other characterization techniques were used to determine the microstructure and crystal orientation of the whole sample section. The microstructure evolution of the matrix, HAZ, and the cladding layer, as well as the mechanical properties such as hardness and tensile properties of the multi-layer sample, were studied in detail. The solidification process was simulated in combination with numerical simulation techniques to determine the solidification mode of 308L stainless steel coating. In addition, the connection between microstructure and mechanical properties was explored, revealing the microstructure evolution law during the LHWC process. This study provides the theoretical basis for the 308L stainless steel coating application.

1.7 Outline of this thesis

Chapter 1 Background and Objective

This chapter introduces the background of the process principle, development history, and application of the laser cladding process. The main research directions and contents of current research on laser cladding, such as processing parameters, microstructure, mechanical properties, and numerical simulation, are discussed. Finally, the research objectives of this paper are explained.

Chapter 2 Microstructure evolution and mechanical properties of 308L

stainless steel coatings

In this chapter, multiple layers of 308L stainless steel coating samples were successfully prepared by LHWC technology. Optical microscopy, electron backscatter diffraction (EBSD), and other characterization techniques were used to determine the microstructure and crystal orientation of the whole sample section. The microstructure evolution of the matrix, HAZ, and the cladding layer, as well as the mechanical properties such as hardness and tensile properties of the multi-layer sample were studied in detail. The evolution of the microstructure during LHWC was revealed, and the solidification mode of the coating layer was determined, which provided a theoretical basis for the application of 308L stainless steel using the LHWC process.

Chapter 3 Research on interface characteristics of 308L stainless steel coatings

In this chapter, multilayer laser cladding samples were prepared using the LHWC technique with 308L stainless steel wire. The microstructure, crystal orientation characteristics, and mechanical properties near the interface were investigated using optical microscopy (OM), electron backscatter diffraction (EBSD), microhardness, and other analytical techniques. The relationship between microstructure and mechanical properties was discussed, which provided a theoretical basis for evaluating the mechanical properties.

Chapter 4 Temperature field simulation and solidification structure during laser hot wire cladding process

In this chapter, the temperature field evolution during the LHWC process was obtained, and the formation process of solidified microstructure was analyzed based on the microstructure obtained in the experiment. The influence of temperature field on the properties of solidified microstructure (grain morphology, grain size, and crystal orientation) was discussed.

Chapter 5 Conclusions

The results from the studies mentioned above are summarized in this chapter.

1.8 References

- [1] CAI M, CHEN L, FANG K, et al. The effects of a ferritic or martensitic matrix on the tensile behavior of a nano-precipitation strengthened ultra-low carbon Ti–Mo–Nb steel [J]. *Materials Science and Engineering: A*, 2021, 801: 140410.
- [2] GAO C, WANG Y, CHENG X, et al. Excellent tensile local deformability and toughness of a tempered low carbon-low alloy steel with multilevel boundaries [J]. *Materials Science and Engineering: A*, 2022, 844: 143195.
- [3] LIN Y-C, MCCARROLL I E, LIN Y-T, et al. Hydrogen trapping and desorption of dual precipitates in tempered low-carbon martensitic steel [J]. *Acta Materialia*, 2020, 196: 516-27.
- [4] CHO Y S, LIAO L K, HSU C H, et al. Effect of substrate bias on biocompatibility of amorphous carbon coatings deposited on Ti6Al4V by PECVD (Reprinted from *Surface & Coatings Technology*, vol 357, pg 212-217, 2019) [J]. *Surface & Coatings Technology*, 2019, 376: 90-5.
- [5] BAI Y Y, XI Y T, GAO K W, et al. Brittle coating effects on fatigue cracks behavior in Ti alloys [J]. *International Journal of Fatigue*, 2019, 125: 432-9.
- [6] TSUJI N, TANAKA S, TAKASUGI T. Evaluation of surface-modified Ti-6Al-4V alloy by combination of plasma-carburizing and deep-rolling [J]. *Materials Science and Engineering a-Structural Materials Properties Microstructure and Processing*, 2008, 488(1-2): 139-45.
- [7] BELEI C, FITSEVA V, DOS SANTOS J F, et al. TiC particle reinforced Ti-6Al-4V friction surfacing coatings [J]. *Surface & Coatings Technology*, 2017, 329: 163-73.
- [8] KUO T Y, CHIN W H, CHIEN C S, et al. Mechanical and biological properties of graded porous tantalum coatings deposited on titanium alloy implants by vacuum plasma spraying [J]. *Surface & Coatings Technology*, 2019, 372: 399-409.
- [9] YU S, ZHENG S, LI X, et al. China can peak its energy-related carbon emissions before 2025: Evidence from industry restructuring [J]. *Energy Economics*, 2018, 73: 91-107.

- [10] TANG B, LI R, YU B, et al. How to peak carbon emissions in China's power sector: A regional perspective [J]. *Energy Policy*, 2018, 120: 365-81.
- [11] WEI Y-M, CHEN K, KANG J-N, et al. Policy and management of carbon peaking and carbon neutrality: A literature review [J]. *Engineering*, 2022.
- [12] KHORRAM A, JAMALOEI A D, PAIDAR M, et al. Laser cladding of Inconel 718 with 75Cr(3)C(2)+25(80Ni20Cr) powder: Statistical modeling and optimization [J]. *Surface & Coatings Technology*, 2019, 378.
- [13] CHEN T, WU W N, LI W P, et al. Laser cladding of nanoparticle TiC ceramic powder: Effects of process parameters on the quality characteristics of the coatings and its prediction model [J]. *Optics and Laser Technology*, 2019, 116: 345-55.
- [14] BOURAHIMA F, HELBERT A L, REGE M, et al. Laser cladding of Ni based powder on a Cu-Ni-Al glassmold: Influence of the process parameters on bonding quality and coating geometry [J]. *Journal of Alloys and Compounds*, 2019, 771: 1018-28.
- [15] LIU H, LIU J, CHEN P J, et al. Microstructure and high temperature wear behaviour of in-situ TiC reinforced AlCoCrFeNi-based high-entropy alloy composite coatings fabricated by laser cladding [J]. *Optics and Laser Technology*, 2019, 118: 140-50.
- [16] NI C, SHI Y, LIU J, et al. Characterization of Al_{0.5}FeCu_{0.7}NiCoCr high-entropy alloy coating on aluminum alloy by laser cladding [J]. *Optics and Laser Technology*, 2018, 105: 257-63.
- [17] LU M Y, MCCORMICK P, ZHAO Y T, et al. Laser deposition of compositionally graded titanium oxide on Ti6Al4V alloy [J]. *Ceramics International*, 2018, 44(17): 20851-61.
- [18] LIU C M, LI C G, ZHANG Z, et al. Modeling of thermal behavior and microstructure evolution during laser cladding of AlSi10Mg alloys [J]. *Optics and Laser Technology*, 2020, 123.
- [19] MAJUMDAR J D, GALUN R, MORDIKE B L, et al. Effect of laser surface melting on corrosion and wear resistance of a commercial magnesium alloy [J]. *Materials Science and Engineering a-Structural Materials Properties Microstructure*

and Processing, 2003, 361(1-2): 119-29.

[20] ZHU L D, XUE P S, LAN Q, et al. Recent research and development status of laser cladding: A review [J]. *Optics and Laser Technology*, 2021, 138.

[21] SIDDIQUI A A, DUBEY A K. Recent trends in laser cladding and surface alloying [J]. *Optics and Laser Technology*, 2021, 134.

[22] WU H, FAHY W P, KIM S, et al. Recent developments in polymers/polymer nanocomposites for additive manufacturing [J]. *Progress in Materials Science*, 2020, 111.

[23] SONG J F, SHE J, CHEN D L, et al. Latest research advances on magnesium and magnesium alloys worldwide [J]. *Journal of Magnesium and Alloys*, 2020, 8(1): 1-41.

[24] LIU Y, DING Y, YANG L, et al. Research and progress of laser cladding on engineering alloys: A review [J]. *Journal of Manufacturing Processes*, 2021, 66: 341-63.

[25] LE V T, MAI D S, DOAN T K, et al. Wire and arc additive manufacturing of 308L stainless steel components: Optimization of processing parameters and material properties [J]. *Engineering Science and Technology, an International Journal*, 2021.

[26] NAD M, KOLIKOVA L, ROLNIK L, et al. Investigation of vibration effects and tool shape on edge chipping phenomenon occurring during rotary ultrasonic drilling [J]. *Journal of Sound and Vibration*, 2019, 439: 251-9.

[27] BARTKOWSKI D, MLYNARCZAK A, PIASECKI A, et al. Microstructure, microhardness and corrosion resistance of Stellite-6 coatings reinforced with WC particles using laser cladding [J]. *Optics and Laser Technology*, 2015, 68: 191-201.

[28] DEVOJNO O G, FELDSHTEIN E, KARDAPOLAVA M A, et al. On the formation features, microstructure and microhardness of single laser tracks formed by laser cladding of a NiCrBSi self-fluxing alloy [J]. *Optics and Lasers in Engineering*, 2018, 106: 32-8.

[29] MUVVALA G, KARMAKAR D P, NATH A K. Online monitoring of thermo-cycles and its correlation with microstructure in laser cladding of nickel based super alloy [J]. *Optics and Lasers in Engineering*, 2017, 88: 139-52.

- [30] HOFMAN J T, DE LANGE D F, PATHIRAJ B, et al. FEM modeling and experimental verification for dilution control in laser cladding [J]. *Journal of Materials Processing Technology*, 2011, 211(2): 187-96.
- [31] HUNG C F, LIN J M. Solidification model of laser cladding with wire feeding technique [J]. *Journal of Laser Applications*, 2004, 16(3): 140-6.
- [32] GOUGE M F, MICHALERIS P, PALMER T A. Fixturing Effects in the Thermal Modeling of Laser Cladding [J]. *Journal of Manufacturing Science and Engineering-Transactions of the Asme*, 2017, 139(1).
- [33] SCHOPPHOVEN T, GASSER A, WISSENBACH K, et al. Investigations on ultra-high-speed laser material deposition as alternative for hard chrome plating and thermal spraying [J]. *Journal of Laser Applications*, 2016, 28(2).
- [34] WANG Z D, SUN G F, LU Y, et al. High-performance Ti-6Al-4V with graded microstructure and superior properties fabricated by powder feeding underwater laser metal deposition [J]. *Surface & Coatings Technology*, 2021, 408.
- [35] NING F D, CONG W L. Ultrasonic vibration-assisted (UV-A) manufacturing processes: State of the art and future perspectives [J]. *Journal of Manufacturing Processes*, 2020, 51: 174-90.
- [36] HU Y, WANG L, YAO J H, et al. Effects of electromagnetic compound field on the escape behavior of pores in molten pool during laser cladding [J]. *Surface & Coatings Technology*, 2020, 383.
- [37] WEN X, JIN G, CUI X F, et al. Underwater wet laser cladding on 316L stainless steel: A protective material assisted method [J]. *Optics and Laser Technology*, 2019, 111: 814-24.
- [38] CONG W L, NING F D. A fundamental investigation on ultrasonic vibration-assisted laser engineered net shaping of stainless steel [J]. *International Journal of Machine Tools & Manufacture*, 2017, 121: 61-9.
- [39] RAMIRO P, ALBERDI A, ORTIZ M, et al. Characteristics of Fe-, Ni- and Co-based Powder Coatings Fabricated by Laser Metal Deposition without Preheating the base Material [J]. *Procedia CIRP*, 2018, 68: 381-6.
- [40] GAO W Y, ZHAO S S, LIU F L, et al. Effect of defocus manner on laser cladding

- of Fe-based alloy powder [J]. *Surface & Coatings Technology*, 2014, 248: 54-62.
- [41] TONG X, LI F H, LIU M, et al. Thermal fatigue resistance of non-smooth cast iron treated by laser cladding with different self-fluxing alloys [J]. *Optics and Laser Technology*, 2010, 42(7): 1154-61.
- [42] LI Q, ZHANG D W, LEI T Q, et al. Comparison of laser-clad and furnace-melted Ni-based alloy microstructures [J]. *Surface & Coatings Technology*, 2001, 137(2-3): 122-35.
- [43] HAROONI A, IRAVANI M, KHAJEPOUR A, et al. Mechanical properties and microstructures in zirconium deposited by injected powder laser additive manufacturing [J]. *Additive Manufacturing*, 2018, 22: 537-47.
- [44] RAMAKRISHNAN A, DINDA G P. Microstructural control of an Al-W aluminum matrix composite during direct laser metal deposition [J]. *Journal of Alloys and Compounds*, 2020, 813.
- [45] SUN R L, LEI Y W, NIU W. Laser clad TiC reinforced NiCrBSi composite coatings on Ti-6Al-4V alloy using a CW CO₂ laser [J]. *Surface & Coatings Technology*, 2009, 203(10-11): 1395-9.
- [46] LU P, LEWIS S R, FRETWELL-SMITH S, et al. Laser cladding of rail; the effects of depositing material on lower rail grades [J]. *Wear*, 2019, 438.
- [47] ROY T, ABRAHAMS R, PARADOWSKA A, et al. Evaluation of the mechanical properties of laser clad hypereutectoid steel rails [J]. *Wear*, 2019, 432-433: 202930.
- [48] WENG F, CHEN C, YU H. Research status of laser cladding on titanium and its alloys: A review [J]. *Materials & Design*, 2014, 58: 412-25.
- [49] ZHU L, XUE P, LAN Q, et al. Recent research and development status of laser cladding: A review [J]. *Optics & Laser Technology*, 2021, 138: 106915.
- [50] QI C Q, ZHAN X H, GAO Q Y, et al. The influence of the pre-placed powder layers on the morphology, microscopic characteristics and microhardness of Ti-6Al-4V/WC MMC coatings during laser cladding [J]. *Optics and Laser Technology*, 2019, 119.
- [51] RIQUELME A, RODRIGO P, ESCALERA-RODRIGUEZ M D, et al.

- Characterisation and mechanical properties of Al/SiC metal matrix composite coatings formed on ZE41 magnesium alloys by laser cladding [J]. *Results in Physics*, 2019, 13.
- [52] LI X F, CHU H J, CHEN Y T, et al. Microstructure and properties of the laser cladding ODS layers on CLAM steel [J]. *Surface & Coatings Technology*, 2019, 357: 172-9.
- [53] ZHANG Z, KOVACEVIC R. Laser cladding of iron-based erosion resistant metal matrix composites [J]. *Journal of Manufacturing Processes*, 2019, 38: 63-75.
- [54] SHI C, LEI J B, ZHOU S F, et al. Microstructure and mechanical properties of carbon fibers strengthened Ni-based coatings by laser cladding: The effect of carbon fiber contents [J]. *Journal of Alloys and Compounds*, 2018, 744: 146-55.
- [55] GEORGE E P, CURTIN W A, TASAN C C. High entropy alloys: A focused review of mechanical properties and deformation mechanisms [J]. *Acta Materialia*, 2020, 188: 435-74.
- [56] ZHANG Y, LU Z P, MA S G, et al. Guidelines in predicting phase formation of high-entropy alloys [J]. *Mrs Communications*, 2014, 4(2): 57-62.
- [57] ZHANG G J, TIAN Q W, YIN K X, et al. Effect of Fe on microstructure and properties of AlCoCrFexNi ($x=1.5, 2.5$) high entropy alloy coatings prepared by laser cladding [J]. *Intermetallics*, 2020, 119.
- [58] GUO Y J, LI C G, ZENG M, et al. In-situ TiC reinforced CoCrCuFeNiSi_{0.2} high-entropy alloy coatings designed for enhanced wear performance by laser cladding [J]. *Materials Chemistry and Physics*, 2020, 242.
- [59] GU Z, XI S Q, SUN C F. Microstructure and properties of laser cladding and CoCr(2.5)FeNi(2)Tix high-entropy alloy composite coatings [J]. *Journal of Alloys and Compounds*, 2020, 819.
- [60] SHU F Y, ZHANG B L, LIU T, et al. Effects of laser power on microstructure and properties of laser clad CoCrBFeNiSi high-entropy alloy amorphous coatings [J]. *Surface & Coatings Technology*, 2019, 358: 667-75.
- [61] LIU J, LIU H, CHEN P J, et al. Microstructural characterization and corrosion behaviour of AlCoCrFeNiTix high-entropy alloy coatings fabricated by laser cladding [J]. *Surface & Coatings Technology*, 2019, 361: 63-74.

- [62] JUAN Y F, LI J, JIANG Y Q, et al. Modified criteria for phase prediction in the multi-component laser-clad coatings and investigations into microstructural evolution/wear resistance of FeCrCoNiAlMox laser-clad coatings [J]. *Applied Surface Science*, 2019, 465: 700-14.
- [63] LIU S, LIU W, HAROONI M, et al. Real-time monitoring of laser hot-wire cladding of Inconel 625 [J]. *Optics & Laser Technology*, 2014, 62: 124-34.
- [64] ABIOYE T E, MCCARTNEY D G, CLARE A T. Laser cladding of Inconel 625 wire for corrosion protection [J]. *Journal of Materials Processing Technology*, 2015, 217: 232-40.
- [65] HEIGEL J C, GOUGE M F, MICHALERIS P, et al. Selection of powder or wire feedstock material for the laser cladding of Inconel® 625 [J]. *Journal of Materials Processing Technology*, 2016, 231: 357-65.
- [66] LI F, GAO Z, LI L, et al. Microstructural study of MMC layers produced by combining wire and coaxial WC powder feeding in laser direct metal deposition [J]. *Optics & Laser Technology*, 2016, 77: 134-43.
- [67] LIU S, KOVACEVIC R. Statistical analysis and optimization of processing parameters in high-power direct diode laser cladding [J]. *The International Journal of Advanced Manufacturing Technology*, 2014, 74(5): 867-78.
- [68] LIU S, LIU W, KOVACEVIC R. Experimental investigation of laser hot-wire cladding [J]. *Proceedings of the Institution of Mechanical Engineers, Part B: Journal of Engineering Manufacture*, 2017, 231(6): 1007-20.
- [69] NURMINEN J. Hot-wire laser cladding: Process, materials and their properties [M]. Tampere University of Technology, 2008.
- [70] ZHANG Z, KONG F, KOVACEVIC R. Laser hot-wire cladding of Co-Cr-W metal cored wire [J]. *Optics and Lasers in Engineering*, 2020, 128.
- [71] OHNISHI T, KAWAHITO Y, MIZUTANI M, et al. Butt welding of thick, high strength steel plate with a high power laser and hot wire to improve tolerance to gap variance and control weld metal oxygen content [J]. *Science and Technology of Welding and Joining*, 2013, 18(4): 314-22.

- [72] NURMINEN J, RIIHIMÄKI J, NÄKKI J, et al. Comparison of laser cladding with powder and hot and cold wire techniques; proceedings of the International Congress on Applications of Lasers & Electro-Optics, F, 2006 [C]. Laser Institute of America.
- [73] SYED W U H, LI L. Effects of wire feeding direction and location in multiple layer diode laser direct metal deposition [J]. Applied Surface Science, 2005, 248(1): 518-24.
- [74] CAPELLO E, PREVITALI B. The influence of operator skills, process parameters and materials on clad shape in repair using laser cladding by wire [J]. Journal of Materials Processing Technology, 2006, 174(1): 223-32.
- [75] MAO K, WANG H, WU Y, et al. Microstructure-property relationship for AISI 304/308L stainless steel laser weldment [J]. Materials Science and Engineering: A, 2018, 721: 234-43.
- [76] MA C, PENG Q, MEI J, et al. Microstructure and corrosion behavior of the heat affected zone of a stainless steel 308L-316L weld joint [J]. Journal of Materials Science & Technology, 2018, 34(10): 1823-34.
- [77] WANG Q, ZHANG S, ZHANG C, et al. Microstructure evolution and EBSD analysis of a graded steel fabricated by laser additive manufacturing [J]. Vacuum, 2017, 141: 68-81.
- [78] FU Y, GUO N, ZHOU C, et al. Investigation on in-situ laser cladding coating of the 304 stainless steel in water environment [J]. Journal of Materials Processing Technology, 2021, 289.
- [79] LI M, LU T, DAI J, et al. Microstructure and mechanical properties of 308L stainless steel fabricated by laminar plasma additive manufacturing [J]. Materials Science and Engineering: A, 2020, 770.
- [80] LE V T, MAID S. Microstructural and mechanical characteristics of 308L stainless steel manufactured by gas metal arc welding-based additive manufacturing [J]. Materials Letters, 2020, 271.
- [81] WEN P, FENG Z, ZHENG S. Formation quality optimization of laser hot wire cladding for repairing martensite precipitation hardening stainless steel [J]. Optics & Laser Technology, 2015, 65: 180-8.

- [82] LI K, LI D, LIU D, et al. Microstructure evolution and mechanical properties of multiple-layer laser cladding coating of 308L stainless steel [J]. *Applied Surface Science*, 2015, 340: 143-50.
- [83] TORIMS T, BRUCKNER F, RATKUS A, et al. The application of laser cladding to marine crankshaft journal repair and renovation; proceedings of the Engineering Systems Design and Analysis, F, 2014 [C]. American Society of Mechanical Engineers.
- [84] RODRIGUES T A, DUARTE V, AVILA J A, et al. Wire and arc additive manufacturing of HSLA steel: Effect of thermal cycles on microstructure and mechanical properties [J]. *Additive Manufacturing*, 2019, 27: 440-50.
- [85] WU B, PAN Z, DING D, et al. A review of the wire arc additive manufacturing of metals: properties, defects and quality improvement [J]. *Journal of Manufacturing Processes*, 2018, 35: 127-39.
- [86] HADEN C V, ZENG G, CARTER F M, et al. Wire and arc additive manufactured steel: Tensile and wear properties [J]. *Additive Manufacturing*, 2017, 16: 115-23.
- [87] HERZOG D, SEYDA V, WYCISK E, et al. Additive manufacturing of metals [J]. *Acta Materialia*, 2016, 117: 371-92.
- [88] ZHU Y, YANG Y, MU X, et al. Study on wear and RCF performance of repaired damage railway wheels: Assessing laser cladding to repair local defects on wheels [J]. *Wear*, 2019, 430: 126-36.
- [89] CHAKRABORTY R, RAZA M S, DATTA S, et al. Synthesis and characterization of nickel free titanium-hydroxyapatite composite coating over Nitinol surface through in-situ laser cladding and alloying [J]. *Surface & Coatings Technology*, 2019, 358: 539-50.
- [90] ROTTWINKEL B, NÖLKE C, KAIERLE S, et al. Laser cladding for crack repair of CMSX-4 single-crystalline turbine parts [J]. *Lasers in Manufacturing and Materials Processing*, 2017, 4(1): 13-23.
- [91] PAUL S, THOOL K, SINGH R, et al. Experimental Characterization of Clad Microstructure and its Correlation with Residual Stresses [J]. *Procedia Manufacturing*, 2017, 10: 804-18.

- [92] BARTKOWSKI D, BARTKOWSKA A. Wear resistance in the soil of Stellite-6/WC coatings produced using laser cladding method [J]. *International Journal of Refractory Metals & Hard Materials*, 2017, 64: 20-6.
- [93] TOYSERKANI E, KHAJEPOUR A, CORBIN S F. Laser cladding [M]. CRC press, 2004.
- [94] LIU S, LIU W, HAROONI M, et al. Real-time monitoring of laser hot-wire cladding of Inconel 625 [J]. *Optics and Laser Technology*, 2014, 62: 124-34.
- [95] PENG W, JIGUO S, SHIQING Z, et al. Control of wire transfer behaviors in hot wire laser welding [J]. *The International Journal of Advanced Manufacturing Technology*, 2016, 83(9): 2091-100.
- [96] NOWOTNY S, BRUECKNER F, THIEME S, et al. High-performance laser cladding with combined energy sources [J]. *Journal of Laser Applications*, 2015, 27(S1): S17001.
- [97] YAMAMOTO M, SHINOZAKI K, KADOI K, et al. Development of hot-wire laser welding method for lap joint of steel sheet with wide gap [J]. *Quarterly journal of the Japan welding society*, 2011, 29(3): 58s-61s.
- [98] DONGXIA Y, XIAOYAN L, DINGYONG H, et al. Optimization of weld bead geometry in laser welding with filler wire process using Taguchi's approach [J]. *Optics and Laser Technology*, 2012, 44(7): 2020-5.
- [99] SUN Y, HAO M. Statistical analysis and optimization of process parameters in Ti6Al4V laser cladding using Nd:YAG laser [J]. *Optics and Lasers in Engineering*, 2012, 50(7): 985-95.
- [100] BALU P, LEGGETT P, HAMID S, et al. Multi-response optimization of laser-based powder deposition of multi-track single layer hastelloy C-276 [J]. *Materials and Manufacturing Processes*, 2013, 28(2): 173-82.
- [101] MONDAL S, PAUL C, KUKREJA L, et al. Application of Taguchi-based gray relational analysis for evaluating the optimal laser cladding parameters for AISI1040 steel plane surface [J]. *The International Journal of Advanced Manufacturing Technology*, 2013, 66(1): 91-6.
- [102] GULYAEV I P, KOVALEV O B, PINAEV P A, et al. Optical diagnostics of

radiation interaction with the powder stream laterally transported during laser cladding [J]. *Optics and Lasers in Engineering*, 2020, 126.

[103] HAROONI A, NASIRI A M, GERLICH A P, et al. Processing window development for laser cladding of zirconium on zirconium alloy [J]. *Journal of Materials Processing Technology*, 2016, 230: 263-71.

[104] MORVILLE S, CARIN M, CARRON D, et al. Numerical modeling of powder flow during coaxial laser direct metal deposition—comparison between Ti-6Al-4V alloy and stainless steel 316L; proceedings of the Proceedings of the 2012 COMSOL Conference, Milan, F, 2012 [C].

[105] ZHAI L, BAN C, ZHANG J, et al. Characteristics of dilution and microstructure in laser cladding Ni-Cr-B-Si coating assisted by electromagnetic compound field [J]. *Materials Letters*, 2019, 243: 195-8.

[106] VORA H D, RAJAMURE R S, SOUNDARAPANDIAN S, et al. Design and Optimization of Microstructure for Improved Corrosion Resistance in Laser Surface Alloyed Aluminum with Molybdenum [J]. *International Journal of Precision Engineering and Manufacturing*, 2013, 14(8): 1421-32.

[107] URBANIC R J, SAQIB S M, AGGARWAL K. Using Predictive Modeling and Classification Methods for Single and Overlapping Bead Laser Cladding to Understand Bead Geometry to Process Parameter Relationships [J]. *Journal of Manufacturing Science and Engineering-Transactions of the Asme*, 2016, 138(5).

[108] HAN T F, XIAO M, ZHANG Y, et al. Laser cladding composite coatings by Ni-Cr-Ti-B₄C with different process parameters [J]. *Materials and Manufacturing Processes*, 2019, 34(8): 898-906.

[109] SIDDIQUI A A, DUBEY A K. Recent trends in laser cladding and surface alloying [J]. *Optics & Laser Technology*, 2021, 134: 106619.

[110] RIQUELME A, RODRIGO P, ESCALERA-RODRIGUEZ M D, et al. Analysis and optimization of process parameters in Al-SiCp laser cladding [J]. *Optics and Lasers in Engineering*, 2016, 78: 165-73.

[111] DE OLIVEIRA U, OCELIK V, DE HOSSON J T M. Analysis of coaxial laser

- cladding processing conditions [J]. *Surface & Coatings Technology*, 2005, 197(2-3): 127-36.
- [112] ONWUBOLU G C, DAVIM J P, OLIVEIRA C, et al. Prediction of clad angle in laser cladding by powder using response surface methodology and scatter search [J]. *Optics and Laser Technology*, 2007, 39(6): 1130-4.
- [113] GOODARZI D M, PEKKARINEN J, SALMINEN A. Analysis of laser cladding process parameter influence on the clad bead geometry [J]. *Welding in the World*, 2017, 61(5): 883-91.
- [114] LIU Z C, LI T, NING F D, et al. Effects of deposition variables on molten pool temperature during laser engineered net shaping of Inconel 718 superalloy [J]. *International Journal of Advanced Manufacturing Technology*, 2019, 102(1-4): 969-76.
- [115] ALAM M K, EDRISY A, URBANIC J. Microstructural Analysis of the Laser-Cladded AISI 420 Martensitic Stainless Steel [J]. *Metallurgical and Materials Transactions a-Physical Metallurgy and Materials Science*, 2019, 50A(5): 2495-506.
- [116] CAI Y C, LUO Z, CHEN Y, et al. Influence of CeO₂ on tribological behaviour of TiC/Fe-based composite coating [J]. *Surface Engineering*, 2017, 33(12): 936-43.
- [117] SONG H Y, LEI J B, XIE J C, et al. Laser melting deposition of K403 superalloy: The influence of processing parameters on the microstructure and wear performance [J]. *Journal of Alloys and Compounds*, 2019, 805: 551-64.
- [118] YI P, ZHAN X H, HE Q K, et al. Influence of laser parameters on graphite morphology in the bonding zone and process optimization in gray cast iron laser cladding [J]. *Optics and Laser Technology*, 2019, 109: 480-7.
- [119] YU T B, YANG L, ZHAO Y, et al. Experimental research and multi-response multi-parameter optimization of laser cladding Fe313 [J]. *Optics and Laser Technology*, 2018, 108: 321-32.
- [120] BAX B, RAJPUT R, KELLET R, et al. Systematic evaluation of process parameter maps for laser cladding and directed energy deposition [J]. *Additive Manufacturing*, 2018, 21: 487-94.
- [121] REDDY L, PRESTON S P, SHIPWAY P H, et al. Process parameter optimisation of laser clad iron based alloy: Predictive models of deposition efficiency, porosity and

- dilution [J]. *Surface & Coatings Technology*, 2018, 349: 198-207.
- [122] BAREKAT M, RAZAVI R S, GHASEMI A. Wear Behavior of Laser-Cladded Co-Cr-Mo Coating on gamma-TiAl Substrate [J]. *Journal of Materials Engineering and Performance*, 2017, 26(7): 3226-38.
- [123] ELAHI M R, SOHI M H, SAFAEI A. Liquid phase surface alloying of AZ91D magnesium alloy with Al and Ni powders [J]. *Applied Surface Science*, 2012, 258(15): 5876-80.
- [124] EI-LABBAN H F, MAHMOUD E R I, AL-WADAI H. Formation of VC-composite surface layer on high C-Cr bearing tool steel by laser surface cladding [J]. *Journal of Manufacturing Processes*, 2015, 20: 190-7.
- [125] XIANG K, CHEN L Y, CHAI L J, et al. Microstructural characteristics and properties of CoCrFeNiNbx high-entropy alloy coatings on pure titanium substrate by pulsed laser cladding [J]. *Applied Surface Science*, 2020, 517.
- [126] GAO W Y, CHANG C, LI G, et al. Study on the laser cladding of FeCrNi coating [J]. *Optik*, 2019, 178: 950-7.
- [127] WANG T T, ZENG L G, LI Z J, et al. Influences of Laser Surface Alloying with Cr on Microstructural Characteristics and Hardness of Pure Ti [J]. *Metallurgical and Materials Transactions a-Physical Metallurgy and Materials Science*, 2019, 50A(8): 3794-804.
- [128] WANG K M, DU D, LIU G, et al. Microstructure and properties of WC reinforced Ni-based composite coatings with Y₂O₃ addition on titanium alloy by laser cladding [J]. *Science and Technology of Welding and Joining*, 2019, 24(5): 517-24.
- [129] FAROTADE G A, POPOOLA P A, POPOOLA O M. Compositional effect of Zr-containing ceramic on phase and microstructural evolution of Ti-SiC laser clad coatings [J]. *Surface Engineering*, 2019, 35(3): 266-72.
- [130] RAZA M S, HUSSAIN M, KUMAR V, et al. In Situ Production of Hard Metal Matrix Composite Coating on Engineered Surfaces Using Laser Cladding Technique [J]. *Journal of Materials Engineering and Performance*, 2017, 26(1): 76-83.
- [131] GUO C, ZHOU J S, ZHAO J R, et al. Microstructure and Tribological Properties

of a HfB₂-Containing Ni-Based Composite Coating Produced on a Pure Ti Substrate by Laser Cladding [J]. *Tribology Letters*, 2011, 44(2): 187-200.

[132] PIASECKI A, KOTKOWIAK M, MAKUCH N, et al. Wear behavior of self-lubricating boride layers produced on Inconel 600-alloy by laser alloying [J]. *Wear*, 2019, 426: 919-33.

[133] MURATOV V S, MOROZOVA E A. Formation of Structure and Properties of Titanium Under Laser Surface Alloying with Nickel and Manganese [J]. *Metal Science and Heat Treatment*, 2019, 60(9-10): 589-93.

[134] HU Y B, NING F D, WANG H, et al. Laser engineered net shaping of quasi-continuous network microstructural TiB reinforced titanium matrix bulk composites: Microstructure and wear performance [J]. *Optics and Laser Technology*, 2018, 99: 174-83.

[135] LIN P Y, ZHANG Z H, KONG S H, et al. Mechanical Properties of Vermicular Graphite Cast Iron Processed by Selective Laser Surface Alloying with Ultra-fine ZrO₂ Ceramic Particulates [J]. *Acta Metallurgica Sinica-English Letters*, 2016, 29(11): 985-92.

[136] NABHANI M, RAZAVI R S, BAREKAT M. Corrosion study of laser clad Ti-6Al-4V alloy in different corrosive environments [J]. *Engineering Failure Analysis*, 2019, 97: 234-41.

[137] LIU J, SONG Y, CHEN C, et al. Effect of scanning speed on the microstructure and mechanical behavior of 316L stainless steel fabricated by selective laser melting [J]. *Materials & Design*, 2020, 186.

[138] WANG X, MUÑIZ-LERMA J A, SÁNCHEZ-MATA O, et al. Microstructure and mechanical properties of stainless steel 316L vertical struts manufactured by laser powder bed fusion process [J]. *Materials Science and Engineering: A*, 2018, 736: 27-40.

[139] XU X, MI G, LUO Y, et al. Morphologies, microstructures, and mechanical properties of samples produced using laser metal deposition with 316 L stainless steel wire [J]. *Optics and Lasers in Engineering*, 2017, 94: 1-11.

[140] YILMAZ O, UGLA A A. Microstructure characterization of SS308LSi

components manufactured by GTAW-based additive manufacturing: shaped metal deposition using pulsed current arc [J]. *The International Journal of Advanced Manufacturing Technology*, 2017, 89(1): 13-25.

[141] ABIOYE T E, MEDRANO-TELLEZ A, FARAYIBI P K, et al. Laser metal deposition of multi-track walls of 308LSi stainless steel [J]. *Materials and Manufacturing Processes*, 2017, 32(14): 1660-6.

[142] LE V T, MAI D S, HOANG Q H. Effects of cooling conditions on the shape, microstructures, and material properties of SS308L thin walls built by wire arc additive manufacturing [J]. *Materials Letters*, 2020, 280: 128580.

[143] YA W, PATHIRAJ B, LIU S J. 2D modelling of clad geometry and resulting thermal cycles during laser cladding [J]. *Journal of Materials Processing Technology*, 2016, 230: 217-32.

[144] LEE Y, FARSON D F. Simulation of transport phenomena and melt pool shape for multiple layer additive manufacturing [J]. *Journal of Laser Applications*, 2016, 28(1).

[145] CHOI J, HAN L, HUA Y. Modeling and experiments of laser cladding with droplet injection [J]. *Journal of Heat Transfer-Transactions of the Asme*, 2005, 127(9): 978-86.

[146] YI P, LIU Y C, FAN C F, et al. Impact analysis of the thermal mechanical coupling characteristics of graphite morphologies during laser cladding of gray cast iron [J]. *Optics and Laser Technology*, 2017, 90: 52-64.

[147] JAVID Y, GHOREISHI M. Thermo-mechanical analysis in pulsed laser cladding of WC powder on Inconel 718 [J]. *International Journal of Advanced Manufacturing Technology*, 2017, 92(1-4): 69-79.

[148] ZHANG Z, FARAHMAND P, KOVACEVIC R. Laser cladding of 420 stainless steel with molybdenum on mild steel A36 by a high power direct diode laser [J]. *Materials & Design*, 2016, 109: 686-99.

[149] HUANG Y Z, KHAMESEE M B, TOYSERKANI E. A comprehensive analytical model for laser powder-fed additive manufacturing [J]. *Additive Manufacturing*, 2016,

12: 90-9.

[150] KHAMIDULLIN B A, TSIVILSKIY I V, GORUNOV A I, et al. Modeling of the effect of powder parameters on laser cladding using coaxial nozzle [J]. *Surface & Coatings Technology*, 2019, 364: 430-43.

[151] LIU Z Y, QI H, JIANG L. Control of crystal orientation and continuous growth through inclination of coaxial nozzle in laser powder deposition of single-crystal superalloy [J]. *Journal of Materials Processing Technology*, 2016, 230: 177-86.

**Microstructure Evolution and Mechanical Properties of
308L Stainless Steel Coatings**

| | | |
|-------|---|----|
| 2.1 | Introduction..... | 43 |
| 2.2 | Experimental procedure | 45 |
| 2.3 | Results..... | 47 |
| 2.3.1 | Macro-morphologies and microstructures | 47 |
| 2.3.2 | EBSD results..... | 51 |
| 2.3.3 | XRD | 54 |
| 2.3.4 | Mechanical properties..... | 55 |
| 2.4 | Discussion..... | 59 |
| 2.4.1 | Solidification mode..... | 59 |
| 2.4.2 | Detailed grain structures and crystallographic texture..... | 60 |
| 2.5 | Summary..... | 62 |
| 2.6 | References..... | 63 |

2.1 Introduction

Laser cladding technology is a very promising material manufacturing process and is widely used in automotive, aerospace, marine, and many other industrial areas^[1-3]. Most of the cladding materials used in traditional laser cladding technology are powder, owing to the high laser absorption rate, surface finish, and dimensional accuracy of powder materials^[4, 5]. However, the production efficiency of powder materials is low, and they can only produce small part^[6, 7]. To produce medium and large-sized parts more efficiently, laser wire cladding technology (LWC) using metal wire as the cladding material has been widely used in recent years^[8, 9]. Compared with powder materials, metal wires as cladding material can improve production efficiency and utilization rate, avoid dust pollution, and improve the surface quality of the finished products. Simultaneously, it has the advantages of easy automatic production and high product quality^[10, 11]. Thus, LWC technology has been successfully applied in surface protection, surface repair, and surface treatment^[12-14].

308L stainless steel is widely used in petroleum, natural gas, shipbuilding, mining, and other fields owing to its excellent mechanical properties and corrosion resistance. In previous studies, cladding layers were successfully prepared by using 308L stainless steel wire, and the microstructure and mechanical properties of the cladding layers were investigated. Li et al.^[15] used a 308L stainless steel wire to prepare a hollow cubic sample with a height of 50 mm. The microstructure analysis showed that the grain morphology at the bottom of the specimen was columnar dendritic. With increasing height, the grain morphology changed to equiaxed dendritic. Li et al.^[16] explored the microstructure evolution and mechanical properties of the three-cladding layers manufactured using 308L stainless steel. The metallurgical combination of the coating and the substrate was good, and the crystal structure of the coating region was mainly columnar dendrites. In addition, there were some planar crystals and honeycomb dendrites distributed in the bonding zone. The tensile sample of the cladding layer had good mechanical properties, and the fracture form was ductile fracture.

In recent years, the applications of LWC technology using cold wire have been

limited owing to its poor process conditions. Researchers have developed laser hot wire cladding technology (LHWC) to overcome these restrictions. Compared with LWC, LHWC technology adds an independent heat source by a resistance heating device, and the temperature of the metal wire is close to the melting point when it is in contact with the molten pool. Thus, this method can accelerate the wire feeding rate and improve the deposition efficiency and material utilization rate^[17]. Nurminen et al.^[18] demonstrated that the heat input in the LHWC process is mainly from resistant heat. In addition, compared with cold wire, the deposition speed can be increased by 2-4 times by using hot wire. Tuominen et al.^[19] prepared various metal wire cladding layers, including Inconel 625, and the results showed that the Inconel 625 cladding layers had good corrosion resistance. Wei et al.^[20] studied the tensile fracture behavior of martensitic stainless-steel coatings prepared using LHWC technology. The results showed that the fracture behavior was most likely to occur in the HAZ. Most current research on the use of LHWC technology to prepare stainless steel coatings mainly focuses on optimizing the process parameters during the preparation process. Although there have been studies on the microstructure and mechanical properties, few studies are conducted on the microstructure and performance of the matrix and the HAZ. However, in practical applications, the substrate and cladding layer are applied as a whole, so it is not enough to study only the cladding layer, especially when the substrate and the cladding layer are different materials, the combination of the substrate and the cladding layer is also very important. To comprehensively analyze the laser welding process, it is needed to study not only the cladding layer, but also the bonding process of the matrix and the cladding layer. It is necessary to characterize the microstructure and properties of each region separately, including the matrix, HAZ, and the cladding layer. These regions are then combined to completely characterize the microstructure evolution and mechanical properties of the products prepared using LHWC technology.

In this study, multiple layers of 308L stainless steel coating samples were successfully prepared by LHWC technology. OM, EBSD, and other characterization techniques were used to determine the microstructure and crystal orientation of the

wire feeding system. The laser system used a diode laser with a laser spot of 1.6*11 mm as the laser source, with a maximum power of 6 kW. The hot wire device utilized the Joule heat generated by the electric resistance to heat the cold wire to near the melting point. The gas in the shielding box was high-purity argon, which was continuously delivered to the surface of the molten pool at a rate of 30 L/min to prevent oxidation. The deposition laser head and the wire feeder were fixed on the six-axis high-precision industrial robot at a certain angle. The operation of the industrial robot could precisely control the movement of the deposition laser head and the wire feeder. The cladding phenomenon in the LWHC process could be observed and recorded through a high-speed digital camera connected to a computer. Table 2-2 listed the detailed experimental parameters. It was worth mentioning that these parameters were determined after some tentative experiments.

Table 2-2. Parameters of the experiment settings.

| Laser spot (mm) | Laser power (kW) | Process speed (m/min) | Wire feeding speed (m/min) | Wire feeding angle (deg) | Shielding gas(Ar) (L/min) | Wire current (A) |
|-----------------|------------------|-----------------------|----------------------------|--------------------------|---------------------------|------------------|
| 1.6*11 | 5.5 | 0.36 | 12 | 45 | 30 | 169 |

The sample was longitudinally cross-sectioned, ground with sand paper from 400 grit to 1500 grit, and then polished using a diamond polishing paste. Subsequently, the sample was immersed in an aqua regia solution (HCL: HNO₃: H₂O = 3: 1: 10) for 30s. The initial microstructure of the cladding material was observed by VHX-100 metallographic microscope (OM). A Sigma 300/VP scanning electron microscope with EBSD module was used to analyze the crystallographic characteristics of different sample regions (matrix, HAZ, and cladding layer), such as grain size, grain boundary type and grain orientation information. The emitted electron voltage was 20kV, the focal length was 18.5mm, and the scanning step length was 0.3μm. An M03XF22 X-ray diffractometer was used to determine the phase compositions of the different regions of the sample. An FV-110 Vickers hardness tester was used to measure the microhardness of the sample, and the distance between the test points was 0.25mm along the longitudinal section with 1 kg/Nm pressure. A SHIMADZU AG-I tensile

testing machine was used to test the tensile properties of the cladding material. The position and the schematic diagram of the tensile sample size were shown in Fig. 2-2. The tensile direction was parallel to the laser scanning direction. Three samples from each position were taken for the experiment, and finally took the average value to reduce the error. The experiment temperature was room temperature, and the stretching rate was 2mm/min. Took three samples from each position to test to reduce errors. JXA-8900 scanning electron microscope (SEM) was used to observe the fracture morphology of the sample after broken.

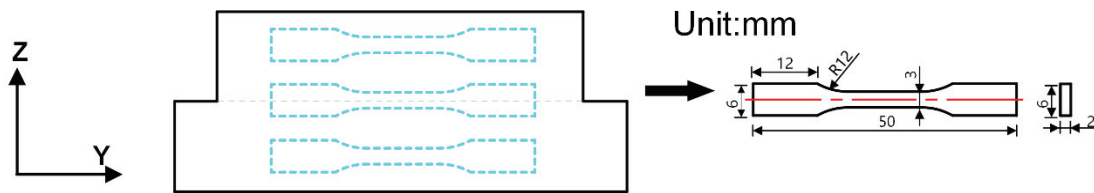


Figure 2-2. Schematic diagram of sampling location and size of tensile samples.

2.3 Results

2.3.1 Macro-morphologies and microstructures

Fig. 2-3 was the macroscopic morphology of the three-layer 308L stainless steel(SS) coating sample prepared by LHWC. It could be seen from Fig. 2-3 that the surface of the sample manufactured under the appropriate process parameters was smooth, and the metallurgical bond between the substrate and 308L SS was well. The width of HAZ was 11.45mm, which was almost same as the width of cladding layer, the height was 1.58mm, and the area was 14.28mm^2 . It had a regular shape, a small area, and no obvious defects such as looseness and holes. The height of the cladding layer was 11.84mm, and the metallurgical bonding between each cladding layer was good, with a relatively obvious boundary. The thickness of each layer was roughly identical, proving that the process was stable and had the potential for large-scale application.

To observe the microstructures and grain morphologies of the matrix, HAZ, and cladding zone in detail and to reveal the evolution of the structure during laser cladding, some specific regions were selected in the cross-section of the sample for further

observation of the metallographic structure, as shown in Fig. 2-4.

The microstructure of the cladding layer 308L was mainly composed of γ austenite, and there were a few δ ferrite phases in the middle of the γ austenite dendrites. The primary morphology was vermicular or skeletal structures, as shown in Fig. 2-4a-Fig. 2-4j, which was also confirmed by previous investigations^[21,22]. Due to the fast-cooling rate and non-equilibrium solidification during laser cladding, there was no sufficient time for δ ferrite to completely transform into austenite, so the cladding layer contained a small amount of residual ferrite at room temperature^[16]. Fig. 2-4k showed the connection between the substrate and the cladding layer. The line in the middle was the fusion line, and the two sides were the HAZ and the first cladding layer. No voids, cracks or other defects were observed near the fusion line. The matrix and the HAZ were dominated by ferrite. The ferrite in the matrix was mainly boned. Due to the action of recrystallization, the grain size of ferrite in the HAZ was significantly smaller than that of the matrix, and the grain morphology presents a random distribution, as shown in Fig. 2-4l and Fig. 2-4m.

In the cladding layer, the morphology of the crystal grains from the bottom of the first layer to the top of the third layer showed a periodic change, which was the result of the combined effect of the temperature gradient (G) and the grain growth rate (R)^[23, 24]. At the beginning of laser cladding, due to the irradiation of the laser, the hot wire was melted on the substrate to form a molten pool. Since the bottom of the molten pool was in contact with the substrate, the heat was mainly transmitted to the substrate by heat conduction. The substrate served as the first heterogeneous nucleation layer. At this point, G was maximum, R was minimum, and the crystal nucleation speed was fast. Therefore, in the center of the first layer, where the laser and the hot wire were in contact, some tiny planar crystals were generated, as shown in Fig. 2-4i. With the solid/liquid interface movement, owing to the decrease of G and the increase of R , the nucleation of columnar dendrites is promoted. When G was reduced to a particular value, the growth rate of the grain accelerated, resulting in a large number of columnar dendrites along the temperature gradient direction, as shown in Fig. 2-4h and Fig. 2-4j. Since the

solidification rate at the bottom was much faster than that at the top, there would be many columnar dendrites in every cladding track, and solidification would eventually be completed at the top. The G at the top was small, and the second layer melted the top region of the first layer in the cladding process, resulting in recrystallization. Therefore, the austenite grain size near the boundary between the two layers was small, and the grain morphology was mostly netlike or honeycomb, as presented in Fig. 2-4c and Fig. 2-4f. In Fig. 2-4b and Fig. 2-4e, the internal grain morphology of the second and third layer was similar to that of the first layer, and both of which were vertically-oriented columnar dendrites that grew along the direction of the temperature gradient. Fig. 2-4d was the fusion zone of the second layer and the third layer, figure. 2-4d clearly and intuitively illustrated the crystal grain morphology difference between the fusion zone and the interior of the third layer. A similar trend can also be seen in Fig. 2-4g. Fig. 2-4a demonstrated the heat at the top was transferred through the air and the solidified pool with a low cooling rate and a small G , thus forming fine equiaxed crystals.

In the first layer of the cladding layers, although the regions in Fig. 2-4i and Fig. 2-4j were both close to the fusion line, the grain morphologies of the two areas were different. Owing to the large temperature gradient in the region far from the center, the columnar dendritic morphology was mainly generated along the structural direction. Because of continuous heating, the wire melted near the center, the region had a slight temperature gradient. More deformation occurred during the cladding process, and some equiaxed crystals were generated.

The grain morphologies of the coatings from the bottom to the top were planar crystals, columnar dendrites, and equiaxed grains.

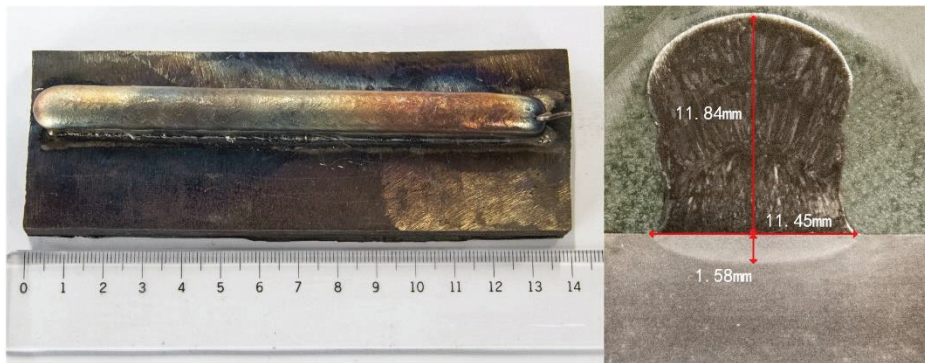


Figure 2-3. Macroscopic morphologies of 308 L stainless steel sample with three layers.

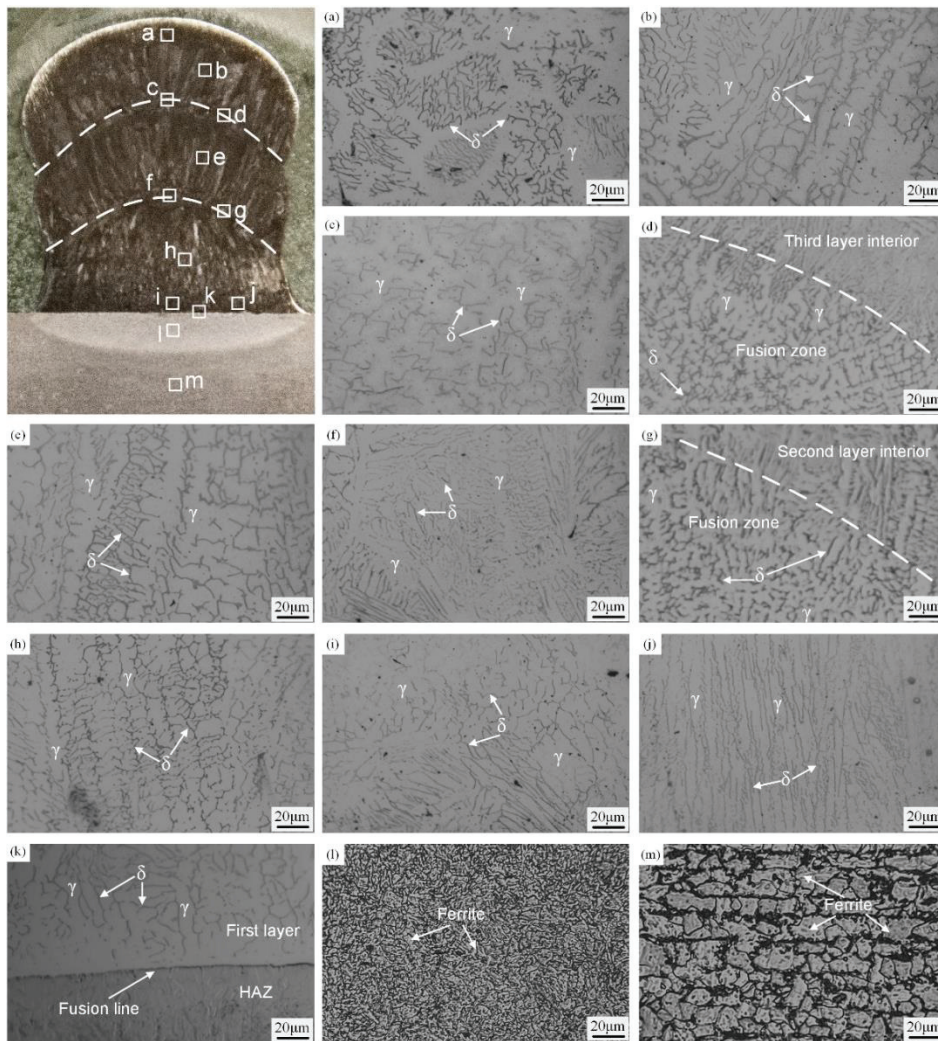


Figure 2-4. Microstructures of 308L stainless steel sample with three layers: (a-b) 3rd layer, (c-d) junction line between 2nd and 3rd layer, (e) 2nd layer, (f-g) junction line between 1st and 2nd layer, (h-j) 1st layer, (k) Fusion line, (l) HAZ, and (m) substrate.

2.3.2 EBSD results

Due to the limitation of the moving algorithm of the SEM sample stage, the field of view area collected by EBSD was usually in μm^2 . In previous research^[14, 25], it was necessary to select samples for observation on the substrate, HAZ, and the cladding layer, respectively, when performing EBSD analysis on laser cladding specimens. The small sampling location and area could only reflect the local tissue characteristics, resulting in incomplete data information, and the analysis results might be accidental. Since laser cladding was a constant process, the microstructure evolution and crystallographic characteristics from the substrate to the cladding layer was also a continuous process. A partial selection of samples was not sufficient to fully reflect the overall evolution mechanism. To solve the above problems, this study used the AZtec Large Area Mapping (LAM) technology developed by Oxford to scan the entire cross-section of the three-layer cladding sample. This technology realized the collection and analysis of crystallographic information in the selected area by precisely adjusting the X-, Y-, and Z-axis positions of the sample stage in the electron microscope. After the scanning was completed, the images were accurately edited and spliced using the Montaged function. Acquired complete, large-area cross-sectional EBSD images while achieving high resolution, which enabled more accurate and intuitive analysis of the crystal orientation, stress distribution, and grain size changes from the substrate to the cladding layer during the laser cladding process.

Fig. 2-5a showed the EBSD orientation map with LAM technology. Different colors represented the different orientations of the grains relative to the lattice, and each color had a unique corresponding relationship with the Euler angle. Therefore, the crystallographic orientation of the grains could be inferred from the color distribution. The closer the color, the closer the crystallographic orientation^[25].

It could be seen from Fig. 2-5a that the grain size distribution and the change process of the grain orientations. The inside of the cladding layer was mainly composed of columnar crystal grains that grew along the structural direction. The crystal grains were mostly coarse. According to the color distribution in Fig. 2-5a, the crystal

orientations on the left and right sides was quite different. The input hot wire produced different temperature gradients on both sides after melting. The fusion region between the cladding layer and the matrix and the junction between the cladding layers were mainly composed of refined grains. This was because these regions had a fast-cooling rate and a large temperature gradient, many refined columnar grains were formed. Besides, both the matrix and the HAZ had small equiaxed grains. The crystal orientations were randomly distributed, and there was no apparent preferred orientation. This was consistent with the grain morphology and distribution were seen in Fig. 2-4.

Peng et al.^[26] pointed out that the temperature gradient component perpendicular to the molten pool boundary was higher than the other directions, which led to the directional grain growth. Fig. 2-5a also clearly showed that columnar grains in the first and second layers grew along a direction almost perpendicular to the fusion line, which was parallel to the direction of the temperature gradient caused by the cooling effect of the substrate. The orientation of the grains in the third layer was flawed because the third layer was far away from the matrix, with a low temperature gradient and slow cooling rate. Therefore, the orientation of the grains was not as well as the two layers below, and the preferred orientation of the crystals appeared in the third layer.

Fig. 2-5b showed the misorientation angle between the grains of the sample cross-section. The interface between grains with misorientation angles in the range of 2° - 10° was regarded as low-angle grain boundaries (LAGB, red). The interface with misorientation angles of more than 10° was considered high-angle grain boundaries (HAGB, blue). As shown in Fig. 2-5b, a large number of red LAGBs were gathered near the fusion line of HAZ and each cladding layer. LAGBs played a strengthening role at the macro level. Numerous LAGBs would hinder the movement of dislocations in the sample stretching process, thus enhancing the strength of the sample. This could be reflected in subsequent mechanical performance tests.

The kernel average misorientation (KAM) of the cross-section derived from the EBSD data was shown in Fig. 2-5c. KAM was a calculation of the average misorientation between each pixel and its nearest neighbors. The KAM diagram

presented the strain by calculating local grain misorientation; it could be seen from Fig. 5c that the green region was mainly distributed in the HAZ and the interface between the cladding layers, indicating that these regions had more significant strain.

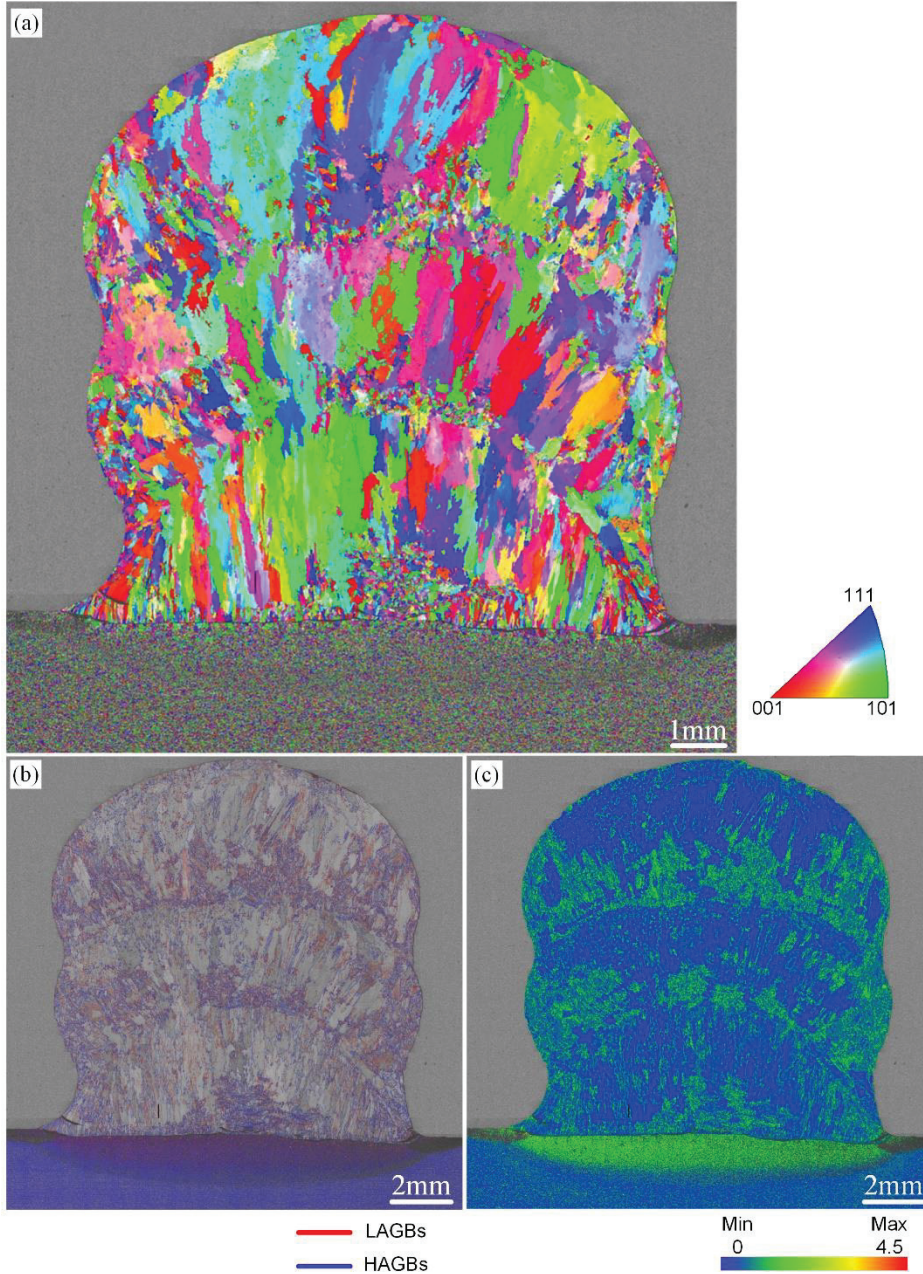


Figure 2-5. EBSD maps of 308 L stainless steel sample with three layers: (a) IPF map, (b) grain boundary map, and (c) KAM map.

Fig. 2-5 could only qualitatively reflect the grain size. To quantify the grain size, EBSD post-processing software was used to calculate the grain size distribution of the entire section. The grain size was defined as the average equivalent circle diameter of each grain, as shown in Fig. 2-6. From Fig. 2-6, it can be inferred that nearly 60% of the grain size of austenite (mainly distributed in the cladding layer) was more extensive

than 19.7 μm . The grain size of ferrite (distributed primarily on the matrix and the HAZ) was small, with more than 60% concentrated below 16.2 μm . This indicated that the coarse austenite grains were mainly distributed in the cladding layer, and the matrix and HAZ were primarily composed of refined ferrite grains.

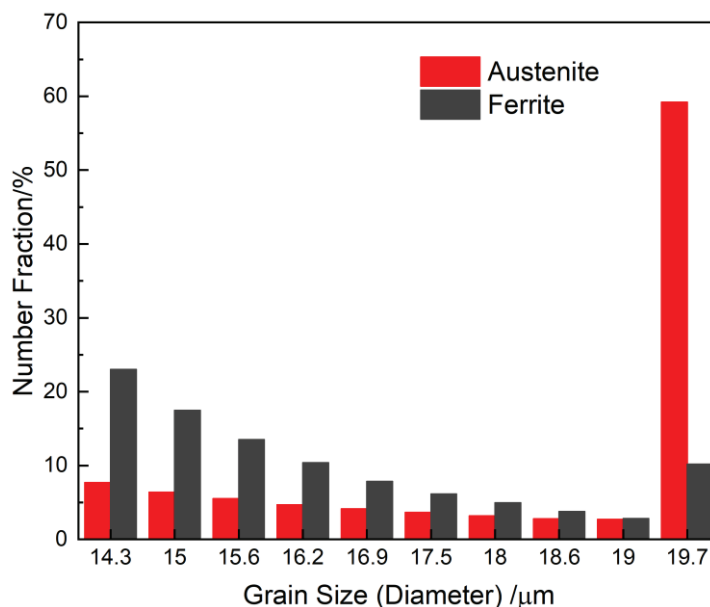


Figure 2-6. Grain size of 308 L stainless steel sample with three layers.

2.3.3 XRD

Fig. 2-7 performed the XRD patterns in different sample regions, from bottom to top; they were the matrix, HAZ, and cladding region. As shown in Fig. 2-7, only two peaks were detected in the matrix and the HAZ: α (110) and α (200), which indicated that the matrix and the HAZ were composed of ferrite. In the cladding layer, the γ (111) peak had the highest integral strength, and there were two austenite peaks: γ (220) and γ (200). In addition, α (110) was detected in the cladding layer, which indicated that the cladding layer was mainly composed of austenite and contained a small amount of ferrite.

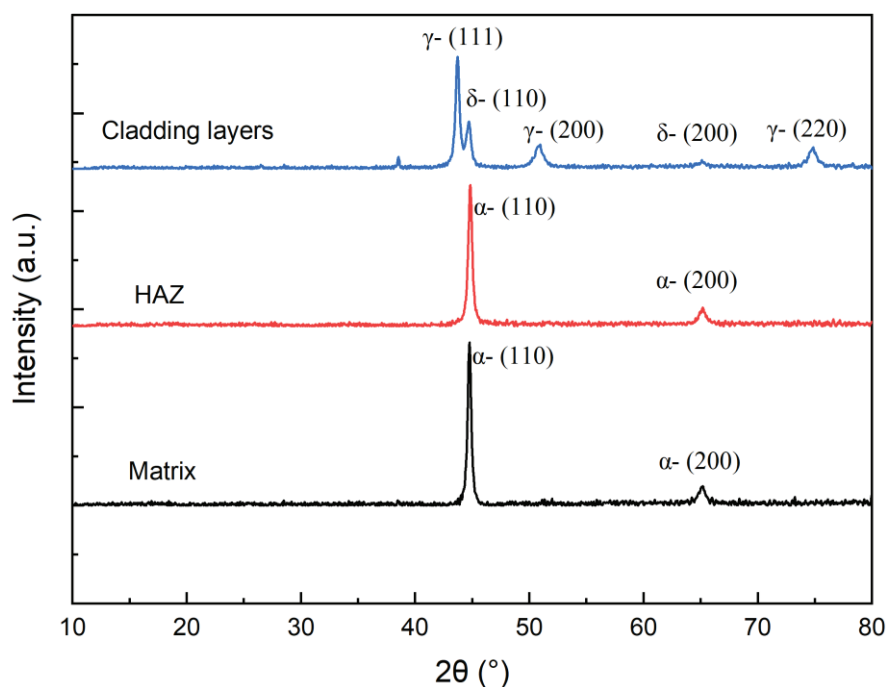


Figure 2-7. XRD patterns of the 308 L stainless steel sample with three layers.

2.3.4 Mechanical properties

Vickers microhardness measurements from different regions were depicted in Fig. 2-8. The hardness of the matrix in the sample was the lowest, gradually increased during the transition section to the HAZ, and reached its highest value in the HAZ. This was because the recrystallization led to a decrease in the grain size, and the refined grains played the role of fine-grain strengthening, which increased the hardness of HAZ. Fig. 2-6 showed the change of grain size from the matrix to the HAZ. From Fig. 2-6, we could conclude that the grain size from the matrix to the HAZ had an obvious decreasing process.

The hardness of the first layer of the cladding region was higher near the HAZ, and began to decrease with increasing distance. But the hardness did not decrease continuously, it first decreased to a certain level, remained stable, and then decreased again. From Fig. 2-5a, it could be inferred that inside the first layer, the area within 2mm from the fusion line was mainly refined equiaxed grains, which increased the strength of the specimen. Therefore, these areas were harder, and the area farther from the fusion line was mostly coarse dendritic crystals, which resulted in lower hardness.

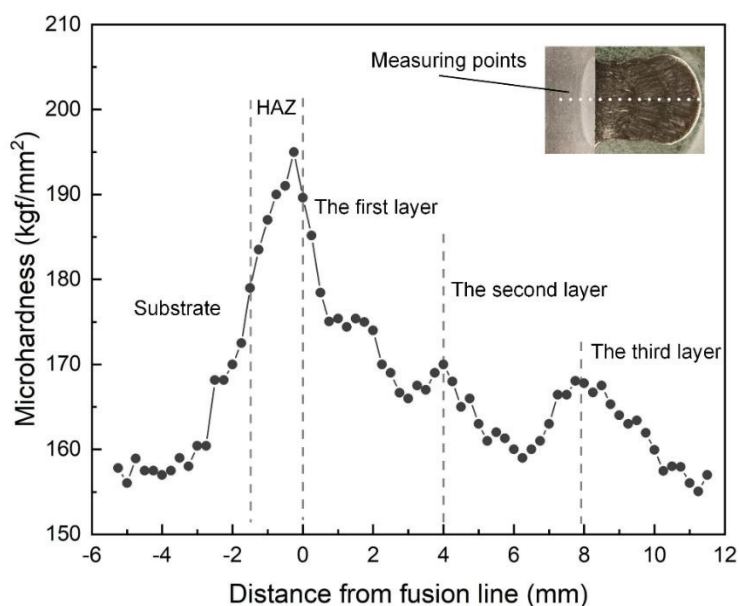


Figure 2-8. Microhardness profile of the 308 L stainless steel sample with three layers.

The hardness change trends of the second and third layers were similar to those of the first layer on the whole. However, it could be seen from Fig. 2-5a that there were no large-scale equiaxed crystals in the second and third layers, so there was no secondary decrease in the hardness change, and the hardness decreased linearly with distance. The hardness gradually increased in the layer-to-layer fusion zone, that was because a secondary HAZ was generated between the layers during the laser welding process. The grains in this region were recrystallized, so there were many refined γ -austenite grains, resulting in higher hardness. In combination with Fig. 2-5b, it could be seen that a large number of LAGBs were gathered in the region where the hardness suddenly increased, which also indicated the strengthening effect of LAGBs. The inside of the crystal grains changed into coarse columnar crystals, and the hardness gradually decreased.

Fig. 2-9a showed the tensile curve of the cladding layer, fusion zone and the matrix in the sample, and the specific sampling locations were shown in Fig. 2-2. A detailed comparison of the tensile strength, yield strength and elongation were shown in Fig. 2-9b. Due to the different materials and microstructures of the laser cladding coating and the substrate, their tensile properties were also different. As shown in Fig. 2-9a, the tensile curve of the substrate performed an obvious yield platform, which was a typical

tensile curve of low carbon steel. Due to the high plasticity and toughness of low-carbon steel, yielding occurred during the tensile deformation process, which was caused by the characteristics of low-carbon steel itself. Similar trends were observed in other studies on low-carbon steels^[27,28]. The yield strength of the matrix (400MPa) was higher than that of the fusion zone (288MPa) and the cladding layer (282MPa). Because the stretching direction of the stretching sample in the cladding layer was parallel to the laser scanning direction, the scanning track of each layer could be used as fiber to improve the tensile properties^[14]. Therefore, the elongation of the cladding layer (44.8%) was higher than that of the fusion zone (32.1%) and the matrix (20.4%). The tensile strength of the fusion zone was the highest (585MPa), which was 1.11 times that of the substrate (525MPa) and 1.05 times that of the cladding layer (558MPa). This was because the grain structure of the fusion zone was fine, which played a role in grain refinement strengthening and improved the strength. On the other hand, in combination with Fig. 2-5b, there were more LAGBs in the fusion zone, and LAGBs could increase the strength of the material, thereby improving the tensile strength of the fusion zone. In Fig. 2-2, half of the tensile samples in the fusion zone were cladding layers, half were HAZ, and the middle was the fusion line. The tensile strength and elongation of the fusion zone were significantly higher than those of the matrix, indicating that the process could dramatically improve the tensile properties of the matrix. On the other hand, it also indicated that the matrix and the cladding layer were firmly bonded, and the LHWC process was stable and reliable.

The corresponding fracture surfaces of the different samples were illustrated in Fig. 2-10. The failure mechanism of the specimen during the tensile test could be understood from the morphology of the tensile fracture surface^[29]. No defects such as holes or cracks were observed in the section view. This indicated a compact microstructure of the sample. This could also be seen in the metallographic images. The dimples could be seen in Fig. 2-10, which indicated that the fracture form of all samples was ductile fracture. There were some differences in the morphology of the dimples, Fig. 2-10a had a larger dimple size, a deeper depth, a more uniform size, and a uniform fracture direction. The macroscopic performance exhibited better plasticity and higher

elongation. Studies had shown that the dimples appeared because the interface bonding strength between austenite and δ -ferrite in 308L stainless steel was low^[16]. The cracks first appeared at the interface junction, then spread, and gradually formed dimples after the separation of the two phases. As shown in Fig. 2-4, austenite had many tiny δ -ferrites. Besides, according to the EBSD images, many austenite grains in the cladding layer had the same orientation, so some tear zones were observed in Fig. 2-10a.

Fig. 2-10b and Fig. 2-10c were cross-sectional images of the fusion zone sample near the sides of the fusion line. Fig. 2-10b showed the cladding layer side, and Fig. 2-10c presented the HAZ side. Compared with that in Fig. 2-10a, the samples in Fig. 2-10b had dimples of different scales. Most of the dimples were smaller in size. Due to the small grain size in the HAZ, there were small dimples with shallow depth. In Fig. 2-10d, although the dimple size was large, the depth was shallow, so the ductility was poor. This was consistent with previous results in this research.

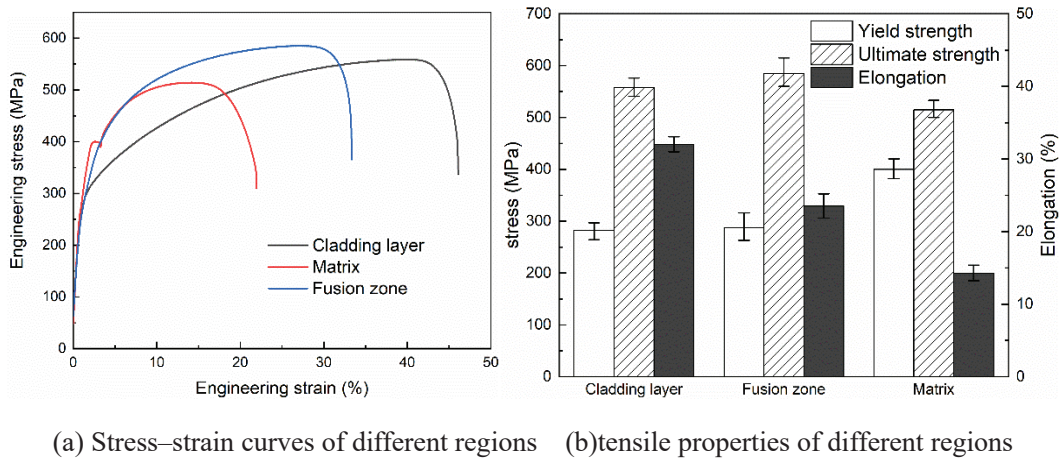


Figure 2-9. Tensile results of the 308 L stainless steel sample with three layers.

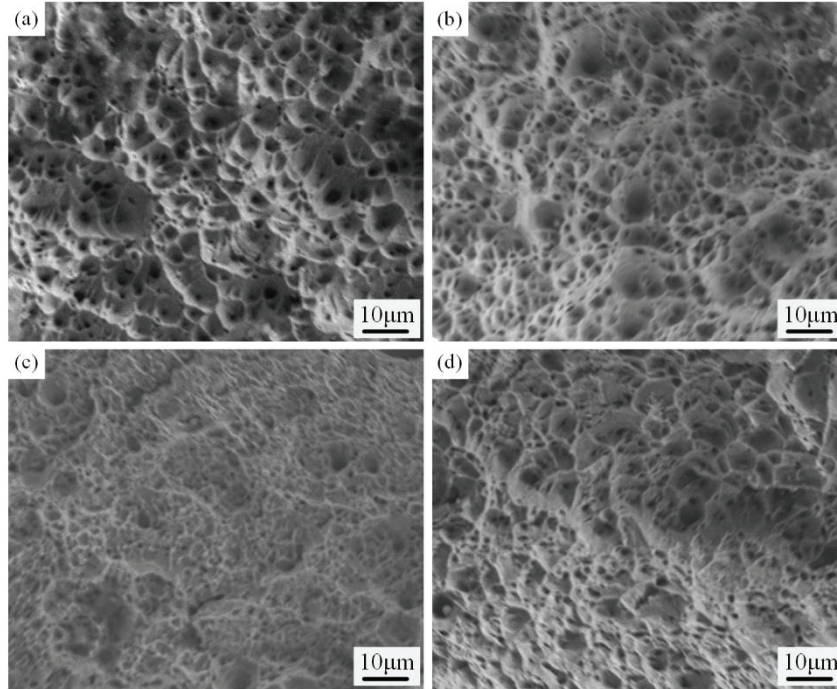


Figure 2-10. Typical tensile test fracture morphologies in different regions: (a) cladding layer, (b) the cladding layer side near the fusion line, (c) HAZ side near the fusion line, and (d) matrix.

2.4 Discussion

2.4.1 Solidification mode

According to the material chemical composition and welding process parameters, there were many solidification modes of austenitic stainless steel. The following four solidification methods had been reported^[21]:

$$\text{F mode: } Cr_{eq}/Ni_{eq}(\text{in wt.}\%) < 1.25, L + \gamma \rightarrow \gamma \quad (2-1)$$

$$\text{AF mode: } 1.25 < Cr_{eq}/Ni_{eq}(\text{in wt.}\%) < 1.48, L + \gamma \rightarrow L + \gamma + \delta \rightarrow \gamma + \delta \quad (2-2)$$

$$\text{FA mode: } 1.48 < Cr_{eq}/Ni_{eq}(\text{in wt.}\%) < 1.95, L + \delta \rightarrow L + \delta + \gamma \rightarrow \delta + \gamma \quad (2-3)$$

$$\text{A mode: } 1.95 < Cr_{eq}/Ni_{eq}(\text{in wt.}\%), L + \delta \rightarrow \delta \quad (2-4)$$

where Cr_{eq} was chromium equivalent, and Ni_{eq} was nickel equivalent. The chemical composition of austenitic stainless steel elements (except Fe) could be simplified using the two parameters. The following Schaeffler formula could calculate the value^[30, 31]:

$$Cr_{eq} = Cr + Mo + 1.5Si + 0.5Nb \quad (2-5)$$

$$Ni_{eq} = Ni + 30C + 0.5Mn \quad (2-6)$$

Substituting the element percentage content from Table 2-1 into the above formula

we obtain $Cr_{eq}=20.53$, $Ni_{eq}=11.08$, $Cr_{eq}/Ni_{eq}=1.85$. Therefore, the solidification mode of 308L stainless steel used in the current work was theoretically the FA mode. In other words, δ ferrite was the initial solidification phase during solidification.

On the other hand, studies had shown that if $Cr_{eq}/Ni_{eq}>1.69$ calculated according to the following WRC-1992 equivalent formula (formula x), then the primary solidification phase could also be considered as a δ ferrite phase [32]. The Cr_{eq}/Ni_{eq} calculated in this study was $1.94>1.69$, so it could be determined that the primary solidification phase in this study was the δ ferrite phase.

$$Cr_{eq} = Cr + Mo + 0.7Nb \quad (2-7)$$

$$Ni_{eq} = Ni + 30C + 20N \quad (2-8)$$

Because Cr, Mo, Si and other elements were ferrite-promoting factors, these elements were rapidly consumed to form δ ferrite at the beginning of the solidification of the 308L wire. The austenite was then formed through a peritectic-eutectic reaction. With the solidification process, most of the primary ferrite would be converted to austenite. However, owing to the rapid cooling rate, a small amount of δ ferrite did not have enough time to convert to austenite when the temperature dropped to room temperature and eventually existed in the form of residual ferrite. Therefore, the microstructure of the cladding layer was dominated by the austenite phase mixed with a small amount of the δ ferrite phase, which was consistent with the OM and XRD results mentioned above.

2.4.2 Detailed grain structures and crystallographic texture

Fig. 2-5 showed the overall large image. Due to the large scanning step size, it might be difficult to observe the small areas of the local grains. Therefore, a typical local location was selected along the central axis of Fig. 2-5 to create a detailed local map. The specific information was shown in Fig. 2-11. Compared with Fig. 2-5, Fig. 2-11 showed more details of the sample microstructure and the change process of the sample from the matrix to the cladding layer. The crystal orientations of the matrix (region d), HAZ (region c) and the region near the fusion line (region b) of the cladding

layer were randomly distributed, there was no apparent preferred orientation, and the grain size was small. The crystal grain size inside the cladding layer (region a) was more prominent, and there was a preferential crystal orientation. The proportion of LAGBs in regions b and c were significantly higher than those in the other two regions, so the strength and hardness of the region b and c were higher. From the color distribution of the KAM diagram, it could be concluded that more strains accumulated in regions b and c, which were close to the fusion line.

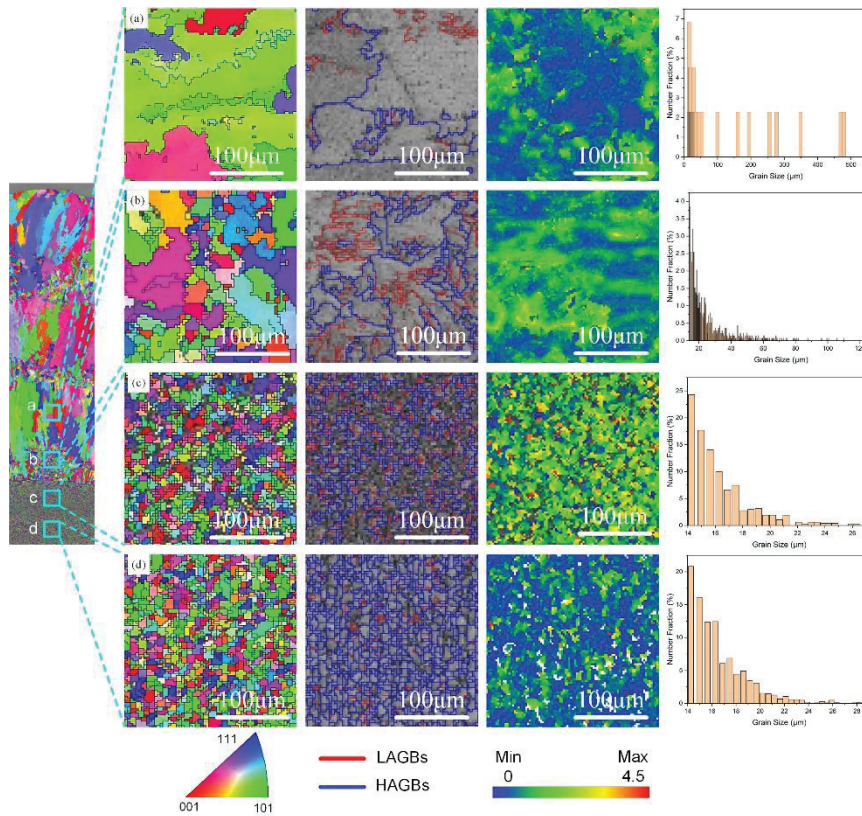


Figure 2-11. IPF map, grain boundary map, KAM map and grain size statistical histogram in different regions: (a) central of 1st layer, (b) bottom of 1st layer, (c) HAZ, and (d) matrix.

Many studies had shown that texture had a significant influence on material properties, such as strength and plasticity. Fig. 2-5 showed that although there was no preferred crystal orientation (texture) in the matrix, the preferred crystal orientation in the cladding layer was evident. To study the change in texture, six typical regions were selected along the central axis of the sample, and polar maps of different regions were obtained. As shown in Fig. 2-12, there was no preferred orientation in the matrix and the HAZ. The grains inside each layer of the cladding layer had an obvious preferred

orientation, and most of the crystal grains grew to the [100] crystal plane family. This was consistent with the results of previous studies^[33]. Although the crystal grains of the first layer of the cladding layer close to the fusion line had a certain tendency of preferential orientation, they were still randomly distributed on the whole.

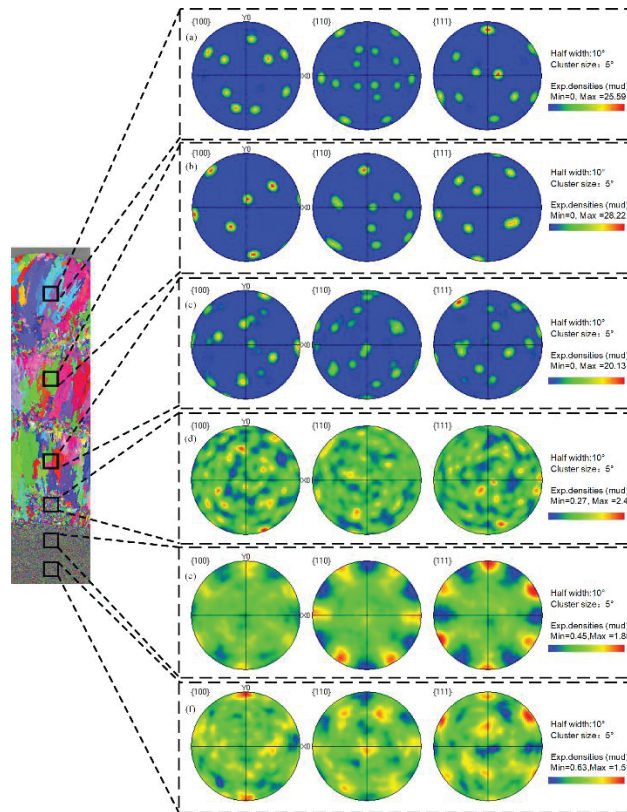


Figure 2-12. Texture of different regions in the 308 L stainless steel sample with three layers.

2.5 Summary

In this study, LHWC technology was used to successfully prepare a 308L stainless steel coating with a compact structure and without holes, cracks or other defects. The microstructure evolution and mechanical properties of the sample matrix, HAZ, and the cladding layer were studied. The conclusions were drawn as follows:

- (1) The surface of the 308L stainless steel coating sample prepared by LHWC technology under appropriate process parameters was smooth. The height of the HAZ was 1.58mm. The height of the cladding layer was 11.84mm. The metallurgical bonding between the substrate and the cladding layer was good, proving the stability and

reliability of the LHWC process.

(2) The solidification mode of 308L stainless steel coating was FA solidification mode. From the bottom of the first layer to the top of the third layer, the grain morphology showed periodic changes. Inside each layer, columnar dendrites grew along the structural direction. The crystal morphologies of the coating from the bottom to the top was plane crystal, columnar dendritic, and equiaxed grain.

(3) The interior of the cladding layer was mainly composed of columnar austenite grains that grew along the structural direction. 60% of the grains had a size larger than $19.7\mu\text{m}$, and the preferred orientation of the crystals in the cladding layer was evident. The matrix and the HAZ were refined equiaxed grains, with more than 60% concentrated below $16.2\mu\text{m}$, and the crystal orientations were randomly distributed without obviously preferred orientations. A large number of LAGBs were gathered near the fusion line of the HAZ and each cladding layer, which increased the strength macroscopically.

(4) The HAZ of the sample had the highest hardness, while the matrix had the lowest hardness. The hardness was higher in the layer-to-layer fusion zone, and then gradually decreased with the increase of the cladding height inside each layer. The elongation of the cladding layer (44.8%) was higher than that of the fusion zone (32.1%) and matrix (20.4%). The tensile strength of the fusion zone was the highest, which was 585MPa. From the dimples in the sample section, it could be concluded that the fracture form of the sample from the matrix to the cladding layer was ductile fracture.

2.6 References

- [1] G. Çam, M. Koçak, Progress in joining of advanced materials, International Materials Reviews 43(1) (1998), pp. 1-44.
- [2] G.R. Desale, C.P. Paul, B.K. Gandhi, S.C. Jain, Erosion wear behavior of laser clad surfaces of low carbon austenitic steel, Wear 266(9) (2009), pp. 975-987.
- [3] Y. Wang, S. Zhao, W. Gao, C. Zhou, F. Liu, X. Lin, Microstructure and properties of laser cladding FeCrBSi composite powder coatings with higher Cr content, Journal

- of *Materials Processing Technology* 214(4) (2014), pp. 899-905.
- [4] Z. Sun, X. Tan, S.B. Tor, W.Y. Yeong, Selective laser melting of stainless steel 316L with low porosity and high build rates, *Materials & Design* 104 (2016), pp. 197-204.
- [5] S.-F. Wen, X.-T. Ji, Y. Zhou, C.-J. Han, Q.-S. Wei, Y.-S. Shi, Corrosion behavior of the S136 mold steel fabricated by selective laser melting, *Chinese Journal of Mechanical Engineering* 31(1) (2018), pp. 1-11.
- [6] J.L. Bartlett, X. Li, An overview of residual stresses in metal powder bed fusion, *Additive Manufacturing* 27 (2019), pp. 131-149.
- [7] S.W. Williams, F. Martina, A.C. Addison, J. Ding, G. Pardal, P. Colegrove, Wire + Arc additive manufacturing, *Materials Science and Technology (United Kingdom)* 32(7) (2016), pp. 641-647.
- [8] P. Wen, Z. Cai, Z. Feng, G. Wang, Microstructure and mechanical properties of hot wire laser clad layers for repairing precipitation hardening martensitic stainless steel, *Optics and Laser Technology* 75 (2015), pp. 207-213.
- [9] E. Brandl, V. Michailov, B. Viehweger, C. Leyens, Deposition of Ti-6Al-4V using laser and wire, part I: Microstructural properties of single beads, *Surface and Coatings Technology* 206(6) (2011), pp. 1120-1129.
- [10] T.E. Abioye, D.G. McCartney, A.T. Clare, Laser cladding of Inconel 625 wire for corrosion protection, *Journal of Materials Processing Technology* 217 (2015), pp. 232-240.
- [11] S. Liu, W. Liu, M. Harooni, J. Ma, R. Kovacevic, Real-time monitoring of laser hot-wire cladding of Inconel 625, *Optics and Laser Technology* 62 (2014), pp. 124-134.
- [12] P. Wen, Z. Feng, S. Zheng, Formation quality optimization of laser hot wire cladding for repairing martensite precipitation hardening stainless steel, *Optics & Laser Technology* 65 (2015), pp. 180-188.
- [13] C.T. Kwok, H.C. Man, F.T. Cheng, K.H. Lo, Developments in laser-based surface engineering processes: with particular reference to protection against cavitation erosion, *Surface and Coatings Technology* 291 (2016), pp. 189-204.
- [14] X. Xu, G. Mi, Y. Luo, P. Jiang, X. Shao, C. Wang, Morphologies, microstructures,

and mechanical properties of samples produced using laser metal deposition with 316 L stainless steel wire, *Optics and Lasers in Engineering* 94 (2017), pp. 1-11.

[15] M. Li, T. Lu, J. Dai, X. Jia, X. Gu, T. Dai, Microstructure and mechanical properties of 308L stainless steel fabricated by laminar plasma additive manufacturing, *Materials Science and Engineering: A* 770 (2020), p. 138523.

[16] K. Li, D. Li, D. Liu, G. Pei, L. Sun, Microstructure evolution and mechanical properties of multiple-layer laser cladding coating of 308L stainless steel, *Applied Surface Science* 340 (2015), pp. 143-150.

[17] Z. Zhang, F. Kong, R. Kovacevic, Laser hot-wire cladding of Co-Cr-W metal cored wire, *Optics and Lasers in Engineering* 128 (2020), p. 105998.

[18] J. Nurminen, J. Riihimäki, J. Näkki, P. Vuoristo, Comparison of laser cladding with powder and hot and cold wire techniques, *International Congress on Applications of Lasers & Electro-Optics* 2006,1006(2006).

[19] J. Tuominen, J. Näkki, H. Pajukoski, J. Miettinen, T. Peltola, P. Vuoristo, Wear and corrosion resistant laser coatings for hydraulic piston rods, *Journal of Laser Applications* 27(2), pp. (2015).

[20] S. Wei, G. Wang, J. Yu, Y. Rong, Competitive failure analysis on tensile fracture of laser-deposited material for martensitic stainless steel, *Materials and Design* 118 (2017), pp. 1-10.

[21] Q. Xiong, H. Li, Z. Lu, J. Chen, Q. Xiao, J. Ma, X. Ru, Characterization of microstructure of A508III/309L/308L weld and oxide films formed in deaerated high-temperature water, *Journal of Nuclear Materials* 498 (2018), pp. 227-240.

[22] H. Ming, Z. Zhang, J. Wang, E.-H. Han, W. Ke, Microstructural characterization of an SA508–309L/308L–316L domestic dissimilar metal welded safe-end joint, *Materials Characterization* 97 (2014), pp. 101-115.

[23] L. Song, G. Zeng, H. Xiao, X. Xiao, S. Li, Repair of 304 stainless steel by laser cladding with 316L stainless steel powders followed by laser surface alloying with WC powders, *Journal of Manufacturing Processes* 24 (2016), pp.116-124.

[24] Y. Fu, N. Guo, C. Zhou, G. Wang, J. Feng, Investigation on in-situ laser cladding coating of the 304 stainless steel in water environment, *Journal of Materials Processing*

Technology 289 (2021), p. 116949.

[25] A. Yadollahi, N. Shamsaei, S.M. Thompson, D.W. Seely, Effects of process time interval and heat treatment on the mechanical and microstructural properties of direct laser deposited 316L stainless steel, *Materials Science and Engineering: A* 644 (2015), pp. 171-183.

[26] P. Guo, B. Zou, C. Huang, H. Gao, Study on microstructure, mechanical properties and machinability of efficiently additive manufactured AISI 316L stainless steel by high-power direct laser deposition, *Journal of Materials Processing Technology* 240 (2017), pp. 12-22.

[27] M. Jafarzadegan, A. Abdollah-zadeh, A.H. Feng, T. Saeid, J. Shen, H. Assadi, Microstructure and Mechanical Properties of a Dissimilar Friction Stir Weld between Austenitic Stainless Steel and Low Carbon Steel, *Journal of Materials Science & Technology* 29(4)(2013), pp. 367-372.

[28] U. Mayo, N. Isasti, J.M. Rodriguez-Ibabe, P. Uranga, On the characterization procedure to quantify the contribution of microstructure on mechanical properties in intercritically deformed low carbon HSLA steels, *Materials Science and Engineering: A*, 792(2020), p. 139800.

[29] J. Liu, Y. Song, C. Chen, X. Wang, H. Li, C.a. Zhou, J. Wang, K. Guo, J. Sun, Effect of scanning speed on the microstructure and mechanical behavior of 316L stainless steel fabricated by selective laser melting, *Materials & Design* 186 (2020), p. 108355.

[30] S. Kou, *Welding metallurgy*, New Jersey, USA (2003), pp. 431-446.

[31] J.C. Lippold, D.J. Kotecki, *Welding metallurgy and weldability of stainless steels*, 2005, p. 376.

[32] T. Lienert, J. Lippold, Improved weldability diagram for pulsed laser welded austenitic stainless steels, *Science and Technology of Welding and Joining* 8(1) (2003), pp. 1-9.

[33] Q. Wang, S. Zhang, C. Zhang, C. Wu, J. Wang, J. Chen, Z. Sun, Microstructure evolution and EBSD analysis of a graded steel fabricated by laser additive

manufacturing, Vacuum 141 (2017), pp. 68-81.

Chapter 3

Research on Interface Characteristics of 308L Stainless Steel

Coatings

| | | |
|-------|---|----|
| 3.1 | Introduction..... | 69 |
| 3.2 | Material and methods..... | 71 |
| 3.3 | Results | 74 |
| 3.3.1 | Macro morphologies..... | 74 |
| 3.3.2 | Microstructures..... | 74 |
| 3.3.3 | Grain structure and texture..... | 78 |
| 3.3.4 | Chemical Composition Across the Interfaces..... | 84 |
| 3.3.5 | Phase compositions in the HAZ and the first cladding layer..... | 86 |
| 3.3.6 | Microhardness..... | 87 |
| 3.4 | Discussion..... | 89 |
| 3.4.1 | Phase transformations..... | 89 |
| 3.4.2 | The relationship between mechanical properties and microstructural features | 92 |
| 3.4 | Summary..... | 95 |
| 3.5 | References..... | 96 |

3.1 Introduction

Laser cladding is a highly efficient surface engineering technology, which can be used for surface repair and additive manufacturing of parts. It is widely used in many industrial fields such as nuclear, automotive, oil, and gas^[1-3]. Laser cladding materials have two forms of metal powder and wire. Although powder materials have the advantages of high absorption rate and high smoothness, they can only be applied to small parts and have low productivity and material utilization, limiting their application^[4-6]. Using metal wire as cladding material significantly improves production efficiency and material utilization rate and avoid dust pollution caused by using powder. The combination of wire feeding mechanisms and intelligent mechanical arms can automate production and quickly produce high-quality products^[7-9]. In recent years, laser wire cladding (LWC) technology has been widely applied in many industries and fields^[10, 11].

There are two kinds of LWC: laser hot wire cladding (LHWC) and laser cold wire cladding (LCWC). LHWC has an additional electric heating device compared to LCWC, which heats the wire to a temperature close to the melting point, thus effectively reducing laser power consumption and improving deposition efficiency. Nurminen et al.^[12] compared the effect of cold and hot wires in the laser cladding process. They found that the deposition efficiency of LHWC was much higher than that of LCWC. The laser is irradiated on the substrate to create a molten pool on the substrate, and the heated wire is continuously input into the molten pool to form metallurgical bonding. After that, the team conducted in-depth research on LHWC and proved that trailing the wire with a high feeding angle provided a better deposition^[13]. Other researchers have also studied the LHWC. Wen et al.^[11] optimized the process parameters of LHWC, established the function of wire feeding speed and current and finally succeeded in obtaining a coating with low surface roughness and low dilution rate. Liu et al.^[7, 14] investigated the process parameters of Inconel 625 hot wire in the LHWC process. The authors obtained the ideal process parameters for Inconel 625 hot wire by real-time inspection of the laser cladding process. The authors concluded that

the heating device used to heat the wire should heat it to a temperature close to the melting point, thereby substantially increasing the deposition efficiency.

In our previous study^[15], the multi-layer 308L stainless steel coating sample was successfully prepared by LHWC technology. The microstructure evolution and mechanical properties of the sample's substrate, the heat-affected zone (HAZ), and the cladding layer were studied. However, the interface between the substrate and the cladding layer is less involved. Since the substrate and the cladding layer are different materials, the bonding at the interface between the two has a decisive influence on the overall life of the material. Several research works have been conducted on dissimilar material welded joints. Okonkwo et al.^[16] studied the microstructure and mechanical properties of the welded joint between low alloy steel 508 and 309/308L stainless steel. They revealed the microstructure evolution of the HAZ and the cladding layer at the welding interface. Besides, the correlation between the microstructure characteristics and mechanical properties of LAS 508 was determined, which presented an inverse relationship between yield strength and grain size. Dong et al.^[17] investigated the stress corrosion cracking behavior of SA 508-309 L/308 L-316 L dissimilar metal welded joints in a primary pressurized water reactor environment and reported the behavior of carbon migration from LAS508 to 309L stainless steel. Ming et al.^[18, 19] studied the microstructure of a series of dissimilar metal welded joints. In their study, Carbon-depleted zones and microstructure transition were found in the SA508 HAZ; Type-I and type-II boundaries existed in 52Mb at some places near the SA508-52Mb interface. From SA508 to 52Mb, a dramatic decrease of Fe and a sharp increase of Ni and Cr were observed at the interface. During the buttering process, the ferrite in the unmixed zone and the zone adjacent to the 309L-CF8A changed to a lamellar structure with intermixed ferrite and austenite strips. In addition, the distribution of microhardness in the interfacial region was also very heterogeneous. Qi et al.^[20] found that both ferrite - austenite solidification mode (FA mode) and austenite - ferrite solidification mode (AF mode) exist for 308L stainless steel. Research studies on the interface of dissimilar materials during laser cladding have been conducted just in the past few years, and still,

some aspects need to be addressed. In laser cladding, heat input, cooling rate, and other factors will change the microstructure of the HAZ and cladding layer. Changes in microstructure usually lead to changes in mechanical properties, which affect the performance of the product. It is necessary to study the microstructure and mechanical properties of the interface region (the HAZ and cladding layer) to evaluate the quality and properties of the prepared 308L stainless steel coating samples.

In this study, multilayer laser cladding samples were prepared using the LHWC technique with 308L stainless steel wire. The microstructure, crystal orientation characteristics and mechanical properties near the interface were investigated using optical microscopy (OM), electron backscatter diffraction (EBSD), microhardness and other analytical techniques. The relationship between microstructure and mechanical properties was discussed, which provided a theoretical basis for evaluating the mechanical properties.

3.2 Material and methods

The 308L stainless steel deposited sample was fabricated on the Low carbon steel (KD-40) with dimensions of 140 mm × 45 mm × 10 mm (length × width × thickness). The additive wire material was 308L stainless steel wire with a diameter of 1.2 mm. Contaminants on the KD-40 substrate surface will reduce the laser absorption of the surface, thereby affecting the surface quality of the sample; therefore, the substrate should be pretreated before the deposition process. The surface treatment methods commonly used in related research are polishing and cleaning with acetone^[10]. In this study, the substrate surface was polished with a handheld polisher to remove the surface contaminants. Then, acetone was degreased to improve the substrate surface laser absorptivity and guarantee the bonding strength. The chemical compositions of substrate KD-40 and 308L stainless steel are shown in Table 3-1.

Table 3-1 Chemical composition of 308L wire and KD-40 substrate (wt%).

| Materials | Cr | Ni | Mn | Si | Mo | P | C | S | Fe |
|-----------|-------|------|------|------|------|-------|------|-------|------|
| SUS308L | 19.87 | 9.98 | 1.60 | 0.38 | 0.09 | 0.024 | 0.01 | 0.001 | Bal. |
| KD-40 | 0.01 | 0.01 | 1.33 | 0.28 | 0.01 | 0.015 | 0.12 | 0.003 | Bal. |

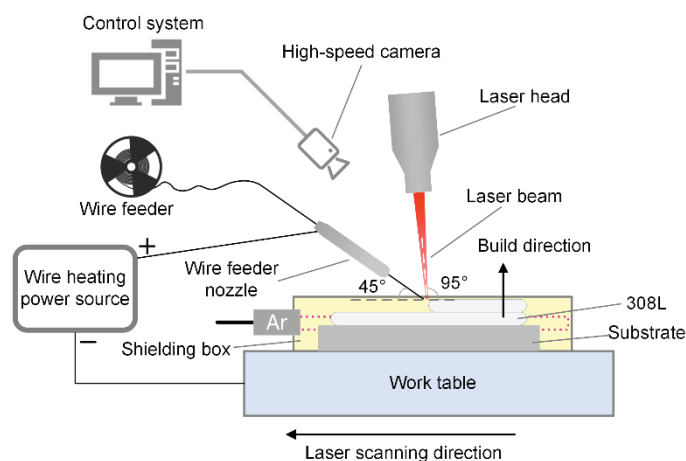


Figure 3-1. Schematic diagram of LHWC experimental equipment.

Fig. 3-1 presented the experimental equipment of LHWC in this study. This set of test equipment consisted of four parts: image acquisition system, robot system, wire feeding system, and laser system. The laser system used a diode laser as the laser source. A significant feature of the diode laser was that the laser shape could be rectangular; the laser spot size used in this experiment was $1.6 \text{ mm} \times 11 \text{ mm}$. The wire feeding system contained the wire heating equipment and the wire feeder. The wire feeder nozzle angle was 45° to the horizontal. The laser head was fixed to the six-axis high-precision industrial robot at an appropriate angle. In general, the laser head angle is set to 90° , but putting it to 90° will cause the laser to reflect to the laser focusing length and damage the laser equipment. Therefore, this angle was set to 95° to the horizontal for safety, as shown in Fig. 3-1. The wire position was in front of the laser spot. In the laser cladding process, the laser spot melted the substrate surface to form a molten pool, the wire heating equipment heated the cold wire to near the melting point. The wire feeder nozzle was aimed at the center of the melt pool and continuously delivered the hot wire to the melt pool. The 100% purity argon gas was blown into the shielding box to prevent oxidation of the cladding material during the laser cladding process. The cladding layer would build after solidification. A high-speed camera was connected to a computer to simultaneously observe and record the melting phenomenon during the LHWC process. Some exploratory experiments were conducted before the formal tests to determine the best process parameters^[21]. The results showed that laser power,

process speed and wire feeding speed impact the material utilization, the final molding quality, and the cladding layers shape. After several experimental comparisons, the most suitable experimental parameters were obtained, as shown in Table 3-2. When these parameters were used, the near net shape rate was the highest, which means high material utilization, good structure and properties of the final sample.

Table 3-2 Parameters of the experiment settings.

| Laser power (kW) | Process speed (m/min) | Wire feeding speed (m/min) | Wire feeding angle (deg) | Wire current (A) | Focal length of lens (mm) | Contact tip to workpiece distance (mm) | Shielding gas (Ar) (L/min) |
|------------------|-----------------------|----------------------------|--------------------------|------------------|---------------------------|--|----------------------------|
| 5.5 | 0.36 | 12 | 45 | 169 | 200 | 50 | 30 |

The sample for metallographic observation was cut along the longitudinal section. The specimen was set and polished with different grit sizes (from 400 grit to 2400 grit) of sandpaper and then polished with 3 μm and 1 μm diamond polishing paste, respectively, until the surface of the specimens was bright and free of scratches. Since the cladding material and the substrate material of the sample were dissimilar materials, the cladding material and the substrate material were etched with different solutions for better microstructure observation. The corrosion solution ratio for the cladding material was $\text{HCl}:\text{HNO}_3:\text{H}_2\text{O} = 3:1:15$; the corrosion time was about 40s. The corrosion solution used for the substrate material was 4% nitric acid alcohol solution, the corrosion time was 10-20s. Microstructures near the fusion line were observed by using the VHX-100 metallurgical microscope. The crystallographic features such as crystal orientation, grain boundary type, grain size, etc. Near the interface of the specimen was analyzed using a Sigma 500/VP scanning electron microscope with an EBSD module. The voltage of the transmitted electrons used in the test was 20 kV, the focal length was 18.5 mm. The phase composition of the different sample regions was determined by using the M03XF22 X-ray diffractometer (XRD). Vickers hardness tester model FV-110 was utilized for hardness testing. Three different locations near the fusion line were selected for testing, with every two tests point separated by 0.25 mm, using a pressure setting of 5 kg/Nm, and the dwell time is 10s.

3.3 Results

3.3.1 Macro morphologies

The macroscopic morphologies of 3-layer 308L stainless steel coating samples prepared by LHWC are shown in Fig. 3-2(a). Fig. 3-2(b) depicts the size of sample 2. Owing to the rectangular laser source with a width of 11 mm, sample 2 achieves a layer width of 11.25 mm, which significantly exceeds the sample size prepared by the conventional circular laser source^[22, 23]. In addition, the height of the cladding layer is 12.40 mm, and the length is 129.00 mm.

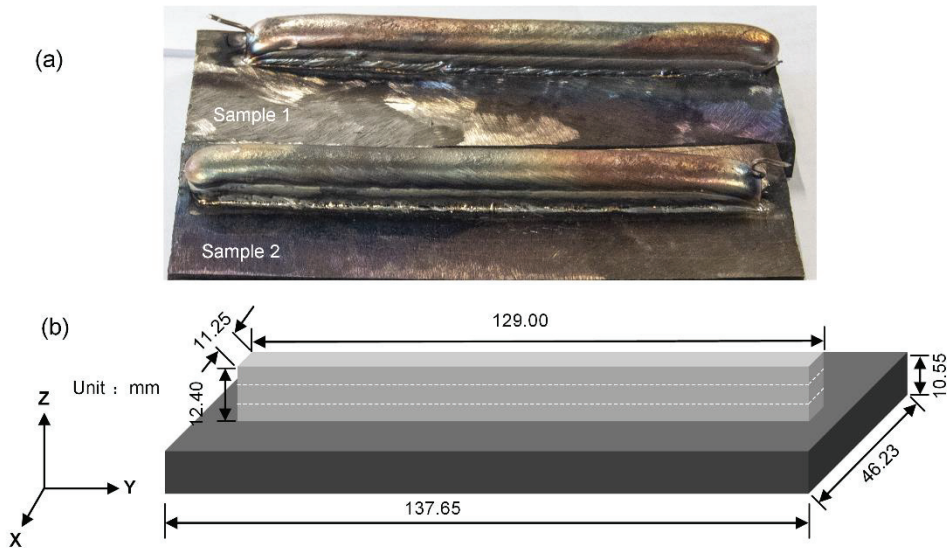


Figure 3-2. (a) Macroscopic morphologies of 308 L stainless steel samples with three layers, (b) dimension of Sample 2.

3.3.2 Microstructures

3.3.2.1 Microstructure of cladding material

Fig. 3-3 illustrates the microstructure of sample 2 at different magnifications in the ZX cross-section. Fig. 3-3(a-d) show the microstructure at low magnification corresponding to the selected area in the figure, and Fig. 3-3(e-h) perform the microstructure at high magnification corresponding to the selected area in the figure. The sample prepared by LHWC has an apparent interface between the substrate and the

cladding layer, and the fusion line is relatively flat and uniform. The substrate and the cladding metal are metallurgically combined well; there are no cracks, holes, or visible defects at the interface. Although the areas corresponding to Fig. 3-3(a-d) are taken from different locations at the interface, the interface's features are generally the same. Above the fusion line is the first cladding layer; the 308L cladding layer is mainly composed of dendritic austenite and columnar austenite; the δ ferrite is distributed among the austenite grains. Similar results have been found in numerous studies using 308L as a filler metal^[24-26]. No obvious precipitates and inclusions are found in the 308L cladding layer. Below the Fusion line is the HAZ, which is composed mainly of fine ferrite. Since the fine-grain morphology in the HAZ region is difficult to observe by optical microscopy, it will be described in detail in combination with EBSD.

More details of the interface region can be seen in the microstructure at high magnification. The fusion line is visible in the central region, as shown in Fig. 3-3(f) and (g). The fusion line of the edge region is relatively blurred, as illustrated in Fig. 3-3(e) and (h), more like a fusion band than a fusion line. The morphology of austenite in the central and edge regions is also different. Since the laser heat source is characterized by high heat in the center and low heat at the edges, the temperature gradient is smaller, and the molten metal cooling rate is slower in the central area. Therefore, as performed in Fig. 3-3(f) and (g), some equiaxed crystals are generated in the central part. While in the edge region, due to the large temperature gradient and fast cooling rate, the austenite is mostly columnar dendritic morphology along the build direction, as concluded in Fig. 3-3 (e) and (h). As presented in Fig. 3-3 (e)-(h), there is δ ferrite in the cladding layer. This is because the ferrite promoting elements such as chromium and molybdenum in the wire are rapidly consumed to form δ ferrite at the beginning of solidification of 308L wire. Then austenite is formed by the peritectic-eutectic reaction. However, due to the fast cooling rate, a small amount of δ ferrite does not have time to transform to austenite when the temperature is reduced to room temperature so that the δ ferrite can be seen in the cladding layer. Further, Heat input will affect the content of ferrite^[27]; the heat input is determined using the following equation^[21]:

$$\text{Heat input} = \frac{P}{A_s \cdot V_p} \quad (3-1)$$

Where P is the laser power, in W; A_s is the area of laser spot size, in mm^2 ; V_p is the process speed, in m/min. Although the shape of the diode laser heat source used in this experiment is rectangular, the laser energy is not distributed uniformly in the rectangle. The energy in the central region is higher than in the edge region, which means the laser power in the central region is more elevated. For the central and edge regions, the process speed and the area of laser spot size are the same. According to Eq. (1-1), higher laser power in the central region implies higher heat input. The central area has a slower cooling speed and a longer heat treatment time due to the higher heat input, resulting in less δ ferrite content, as shown in Fig. 3-3 (f). On the other hand, the edge region has low heat input and cools quickly, so many δ ferrites do not have enough time to transform into austenite, resulting in a higher δ ferrite content, as observed in Fig. 3-3 (e).

In addition, there is a light-colored area of uneven thickness on one side of the cladding layer, as presented in Fig. 3-3 (e)-(h). This region is characterized by a single austenitic phase. Related studies have also demonstrated an austenite-only zone at the interface^[16, 28]. One reason for the absence of the δ ferrite in this zone is that the content of Cr (ferrite promoting element) is less than in the inner region of the cladding layer. On the other hand, the migration of carbon (austenite promoting element) from the substrate to the cladding layer results in the absence of δ ferrite production^[28].

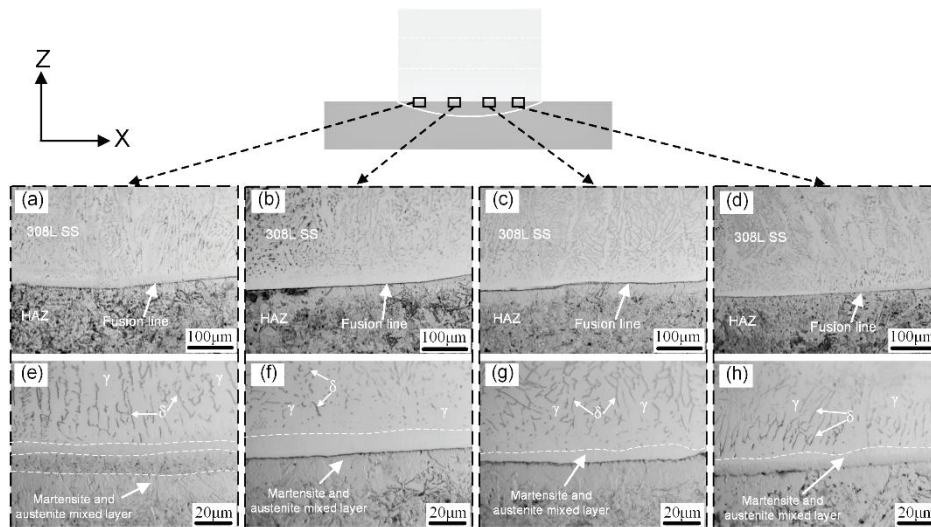


Figure 3-3. Microstructures of 308 L stainless steel: (a-d) Microstructure under low power microscope, (e-h) Microstructure under high power microscope.

3.3.2.2 Microstructure of the HAZ

The microstructure of the HAZ in the substrate is shown in Fig. 3-4. Fig. 3-4 (a) and Fig. 3-4 (c) are taken from different locations on the interface; Fig. 3-4 (b) and Fig. 3-4 (d) are corresponding local magnifications. The microstructure of the HAZ region consisted of ferrite and tempered bainite, and slatted martensite can be observed in part near the interface. The high heat input in the HAZ region near the interface leads to recrystallization during the laser cladding process, transforming bainite into martensite. Studies have shown that martensite is transformed into face-centered cubic austenite mainly through the body-centered cubic bainite structure of the base material and then into martensite with a high strain body-centered tetragonal structure^[29]. This transformation occurs due to the high heat input during the laser cladding process, which is followed by a quenching (rapid cooling) step. The martensite content in the HAZ can significantly increase the hardness in this region, as can be demonstrated in subsequent hardness tests.

The crystal morphology in the substrate away from the interface is significantly different from that of the HAZ near the interface, consisting mainly of ferrite, no martensite is found, and the grain size is larger, as depicted in Fig. 3-5.

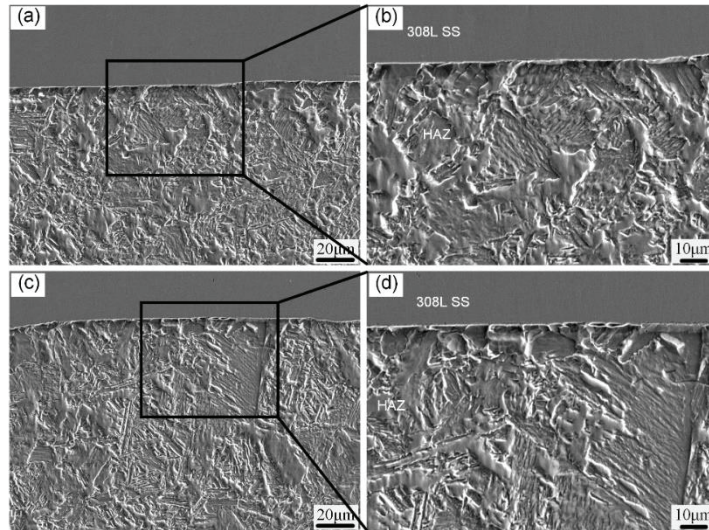


Figure 3-4. Microstructures with different magnifications in different positions of HAZ.

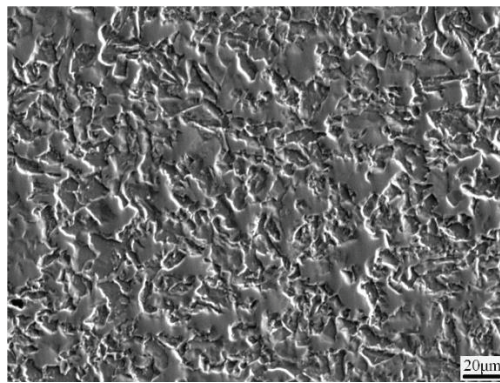


Figure 3-5. Microstructures of substrate material.

3.3.3 Grain structure and texture

The inverse pole figure (IPF) at the sample interface using the Large Area Map (LAM) technique is presented in Fig. 3-6 (a). There is a significant difference in grain size and morphology between the cladding layer and the HAZ area. The internal grain morphology of the cladding layer near the interface is also different. Owing to the high temperature and small temperature gradient, some relatively fine equiaxed crystals are generated near the central region. But on both sides are columnar crystals growing along the tectonic direction, which is caused by the large temperature gradient and high cooling rate^[30, 31]. Because of the small grain size in the HAZ region, it is challenging to observe the details of the grain morphology from Fig. 3-6 (a). To investigate the HAZ

grain morphology and distribution in detail and analyze the differences in crystal orientation and grain morphology at the interface, three regions of the ABC in Fig. 3-6 (a) are selected to make a detailed local map.

Fig. 3-6 (b), (c), (d) present the IPF diagrams of the three regions A, B, and C. There are noticeable columnar crystals near the edge of the cladding layer (region A and C), there is apparent crystal preferred orientation, and the growth direction of grains is consistent with the direction of the structure. This direction is the direction of the maximum temperature gradient and the direction where the grains are most likely to grow. The grain morphology tended to be more equiaxed near the central region (region B). There are small equiaxed crystals on the interface. According to the previous metallographic results, martensite is distributed in these areas. Compared with the cladding layer, the grain size in HAZ is smaller; the grain morphology is irregular. The crystal orientation is randomly distributed with both equiaxed and columnar crystals, and there is no apparent preferred orientation.

The Grain boundary character maps corresponding to the selected region are performed in Fig. 3-6 (e), (f) and (g). The cladding layer is dominated by blue high-angle grain boundaries (HAGBs, orientation difference angle $>10^\circ$), while the HAZ and the interface are surrounded mainly by red low-angle grain boundaries (LAGBs, orientation difference angle in the range of 2° - 10°). LAGBs have a positive effect on the mechanical properties of the material. During deformation, the numerous LAGBs hinder the movement of dislocations, thus improving the strength of the sample. This will be demonstrated in subsequent mechanical property tests.

The kernel average misorientation (KAM) of regions A, B, and C derived from EBSD data is illustrated in Fig. 3-6 (h), (i) and (j). KAM is a calculation of the average misorientation between each pixel and its nearest neighbors^[32, 33]. By calculating KAM, we estimated the residual strain and the energy stored in the deformed material, representing the dislocation density to a certain extent^[34]. According to Fig. 3-6 (h), (i) and (j), the KAM value near the interface and in the HAZ is larger, which indicates that these areas had high energy. High energy meant high residual strain and dislocation density, thereby increasing material strength. The maximum value of residual strain is

almost distributed at the interface. This is because the substrate and the cladding layer are different materials, and the different thermal expansion coefficients of the two can lead to shrinkage, resulting in higher local strains^[18]. The martensite in the HAZ has a high density crystallization defect, leading to a high strain in this region^[35].

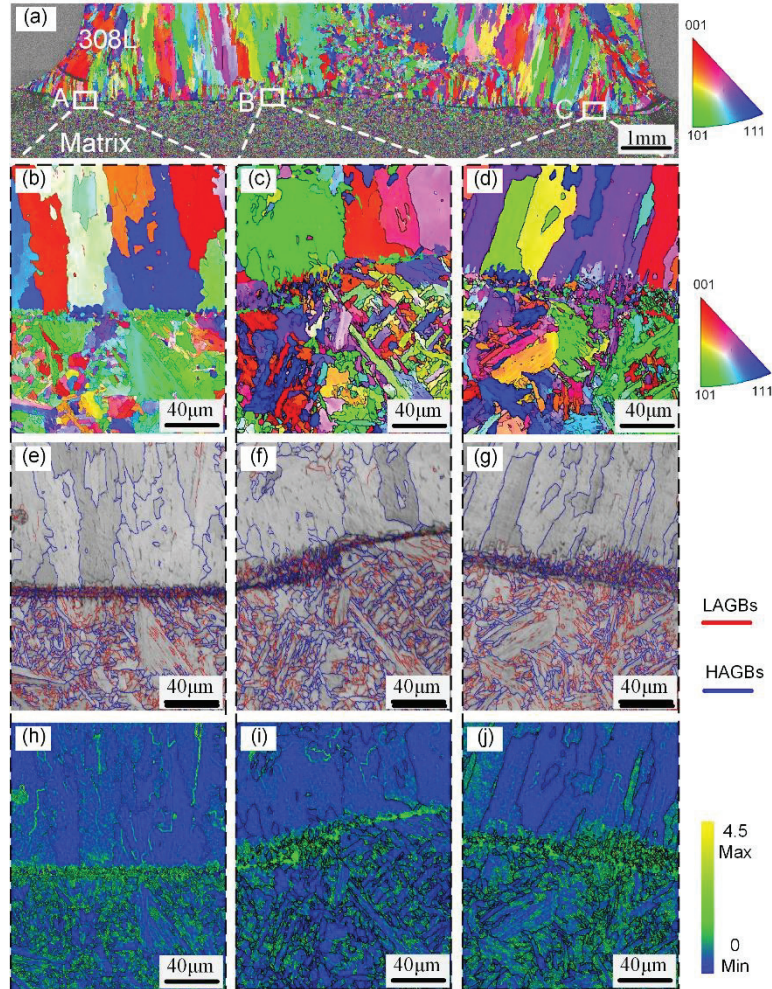


Figure 3-6. EBSD maps of the interface: (a) IPF map by LAM, (b), (c), (d) IPF maps of the three regions A, B, and C, (e), (f), and (g) grain boundary maps of the three regions A, B, and C, and (h), (i), (j) KAM maps of the three regions A, B, and C.

Fig. 3-7 (a), (b) and (c) displays the phase diagrams corresponding to the three regions A, B, and C in Fig. 3-6. The substrate is the single BCC ferrite phase (yellow), and the 308L cladding layer is mainly the FCC austenite phase (red), which contains a small amount of δ ferrite. This is consistent with the results of the microstructure, as mentioned earlier. The phase diagram shows that the boundary between the substrate and the cladding layer is not a straight line but that the BCC and the FCC are intertwined. Since both ferrite and martensite in the phase diagram are of BCC structure, the phase

diagram cannot determine whether it is near martensite or ferrite near the fusion line. Although it is challenging to identify ferrite and martensite by the crystal structure, compared with ferrite, the martensite usually had a higher density of crystal defects or more distorted lattice, which is more likely to generate residual stress during processing, resulting in poor diffraction pattern quality of martensite. In the Channel 5 EBSD data analysis software developed by Oxford, the Band Contrast (BC) and Band Slope (BS) components can indicate diffraction pattern quality; the higher the value, the better the pattern quality. Deformed regions and regions with significant lattice distortion usually have lower Band Contrast and Band Slope values. Therefore, the BC diagram and BS diagram of steel can be superimposed for numerical analysis. The results are shown in Fig. 3-7 (d), (e) and (f). The pattern quality is better in the region with higher values, the austenite or ferrite region (red part of the figure); the pattern quality is worse in the region with lower values, the martensite region (green part of the figure). From this, it can be indirectly determined that martensite is distributed near the fusion line and in the HAZ, similar to the distribution of martensite in Fig. 3-4. Similar findings have been reported in other studies^[28, 36].

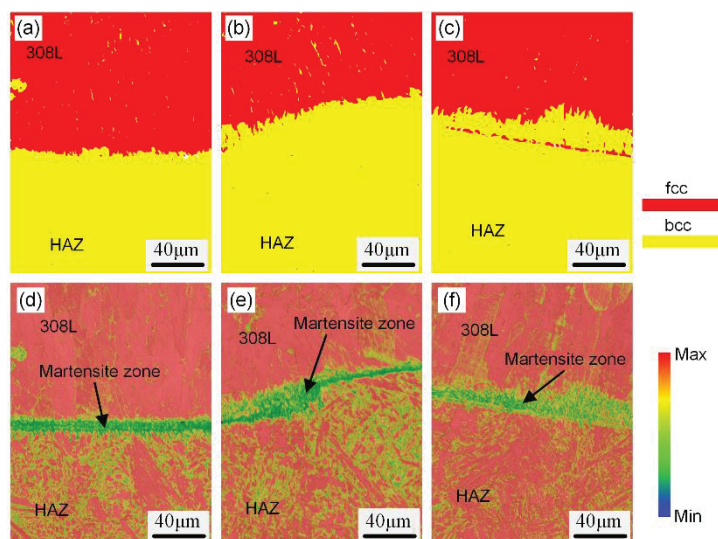


Figure 3-7. (a), (b), and (c) Phase maps corresponding to the regions of A, B, and C; (d), (e), and (f) Schematic diagrams of martensite corresponding to the regions of A, B, and C.

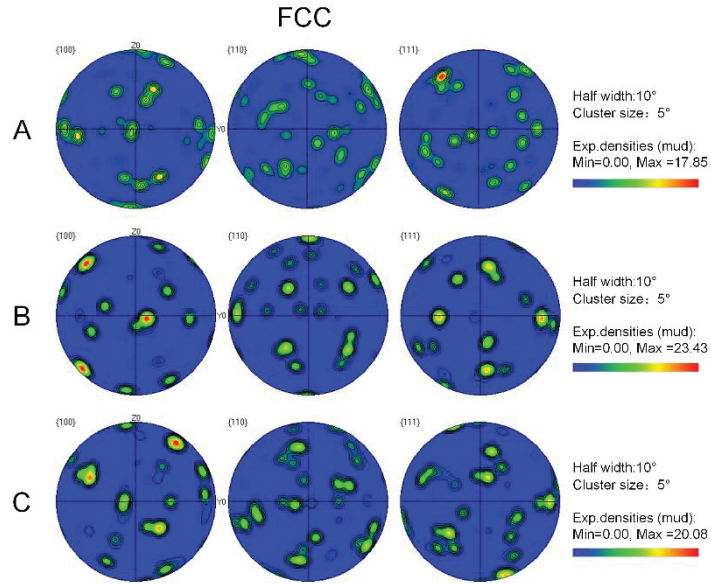


Figure 3-8. The pole figures corresponding to the part of the cladding layer in the A, B, and C area.

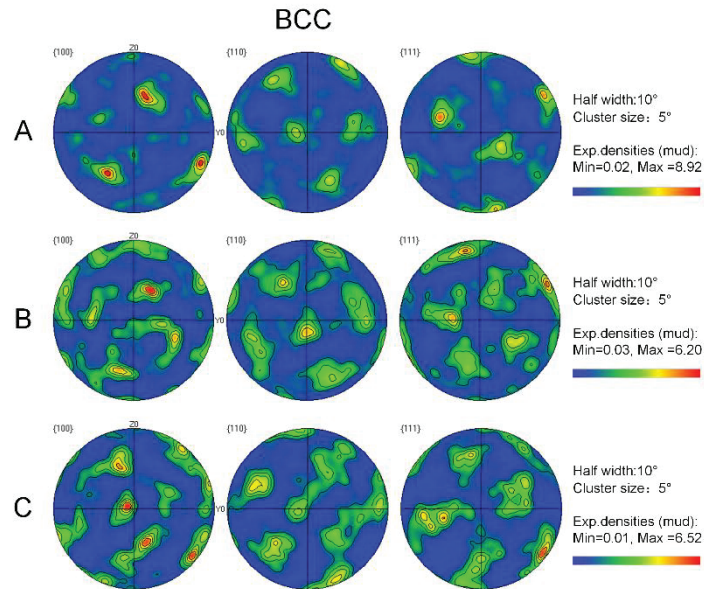


Figure 3-9. The pole figures corresponding to the part of the HAZ in the A, B, and C area.

Studies have shown that 20-50% of the material properties are affected by the texture. The texture has an essential effect on the elastic modulus, Poisson's ratio, strength, plasticity and toughness^[37]. Fig. 3-6 presents that the texture of the substrate and the cladding layer are different. Polar diagrams are made for the BCC region (substrate) and FCC region (cladding layer) to characterize the texture more accurately. A, B and C corresponds to the three regions of A, B and C in Fig. 3-6, as shown in Fig.

3-8 and Fig. 3-9. From the polar diagram, we can see that the texture in the cladding layer in the three regions of A, B and C is apparent. The maximum value is much larger than that of BCC, and most grains grow towards the family of crystal planes of [100]. This is consistent with previous findings^[20]. The texture in HAZ is not clear. The maximum orientation of region A is 8.92, and the maximum orientation of region B is only 6.2. This indicates that, in the HAZ, the texture of crystals closer to the edge is more pronounced. These regions are farther away from the heat source, the temperature gradient is more prominent, and the cooling rate is faster.

It is known from Fig. 3-6 that the austenite grain size in the cladding layer is large, while the ferrite grain size in the HAZ is small. The EBSD post-processing software was used to obtain the grain size of the three A, B and C regions in Fig. 3-6 to quantify the distribution pattern of the grain size, as depicted in Fig. 3-10. Table 3-3 shows the detailed data obtained from the statistics according to Fig. 3-10. Since the austenite (FCC) is all distributed in the cladding layer and the ferrite (BCC) is mainly distributed in the HAZ, separate statistics of FCC and BCC can represent the grain size of the cladding layer and the HAZ, respectively. The grain size distributions of BCC and FCC are different. Most of the grains in BCC are smaller than 5 μm , with a maximum value of 41.82 μm , and the average grain size is between 3.65 μm and 4.18 μm . The grain size of FCC is polarized. Half of the FCC grains having a grain size of less than 6 μm , although there are a considerable number of coarse grains ($>9 \mu\text{m}$), and this trend is most evident in the C region. The maximum grain size of FCC reached 115.13 μm , and the average grain size ranged from 14.65 μm - 24.4 μm . EBSD diagrams show that these refined austenite grains appear at the interface, and the austenite grains inside the cladding layer are large. Overall, the average grain size of bcc is much smaller than that of FCC, which indicates that the grain size of the HAZ is mostly smaller than 5 μm refined grains. Although the average grain size of FCC is much larger than that of BCC, the austenite grain size of the cladding layer at the interface is almost the same as that of the ferrite grain size in HAZ.

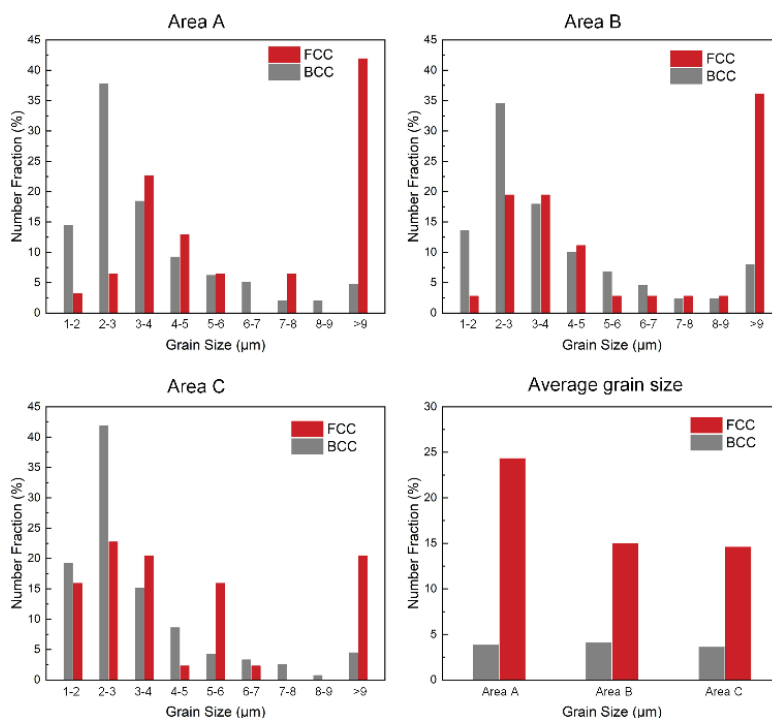


Figure 3-10. The grain size distribution map and average grain size map of the A, B, and C region.

Table 3-3 The grain statistics from the A, B, and C region (μm).

| | Region A | | Region B | | Region C | |
|--------------------|----------|--------|----------|--------|----------|--------|
| | BCC | FCC | BCC | FCC | BCC | FCC |
| Maximum | 41.82 | 111.93 | 24.73 | 115.13 | 39.62 | 111.38 |
| Minimum | 1.78 | 1.95 | 1.78 | 1.95 | 1.78 | 1.78 |
| Average | 3.90 | 24.4 | 4.18 | 15.07 | 3.65 | 14.65 |
| Standard deviation | 3.13 | 34.77 | 3.07 | 25.66 | 3.18 | 29.26 |

3.3.4 Chemical Composition Across the Interfaces

The elemental distribution from the HAZ to the cladding layer was measured using the EDS line scan, as observed in Fig. 3-11. The white horizontal line in Fig. 3-11 is the location of the line scan. The Fe content decreases significantly near the fusion line from the HAZ to the 308L cladding layer. In contrast, the Cr content increases significantly, and the Mn and Ni content also increase slightly. The variation of elemental content along the vicinity of the interface demonstrates that elemental migration does exist near the interface. Fig. 3-12 displays the corresponding EDS

mappings for Fe, Cr, Mn and Ni, which can visualize the differences in the distribution of the above elements on both sides of the fusion line.

Owing to the difference in carbon content between the substrate and the 308L stainless steel, there is a carbon activity gradient between the substrate containing low Cr and the 308L stainless steel which is rich in Cr content^[19]. Therefore, carbons migrate from the substrate to the 308L stainless steel side. The migration of carbon has been reported in other studies^[16, 17, 38, 39]. Cr has a strong affinity for carbon, and the significant increase of Cr content promotes carbon migration. The temperature will also affect the migration of carbon^[19]. The high heat input and long duration of high temperature during the laser cladding process will also promote the carbon migration. The migration of carbon from the substrate into the cladding layer promotes austenite formation, resulting in the zone containing only austenite near the fusion line, as shown in Fig. 3-3. In addition, carbon plays an essential role in the hardness and strength of metals^[19]. Higher carbon concentration usually means higher hardness and strength of metal materials. The carbon migration near the interface increases hardness and strength, which can be proved in the subsequent hardness tests. However, due to the low carbon content of the substrate (0.12%), the change of carbon content is not easily detected by EDS, so there is no significant change in carbon content seen in Fig. 3-11. In addition, as austenite stable elements, the increase of Mn and Ni content also promotes austenite formation.

The dilution of the 308L stainless steel by the substrate caused a drop in Fe concentration and an increase in Ni concentration across the interface, which enhanced the martensitic transformation^[40]. The martensite content in the HAZ can significantly increase the hardness in this region, as can be demonstrated in the subsequent hardness test. Furthermore, the migration of Ni element from the cladding layer to the HAZ promotes the refinement of the HAZ microstructure, resulting in the effect of fine-grain strengthening and increases the hardness near the interface^[41].

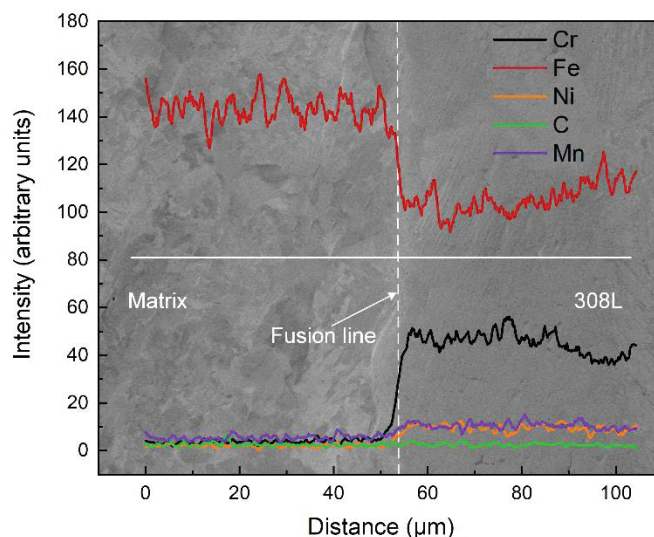


Figure 3-11. SEM-EDS line scan distribution of major elements across the interface.

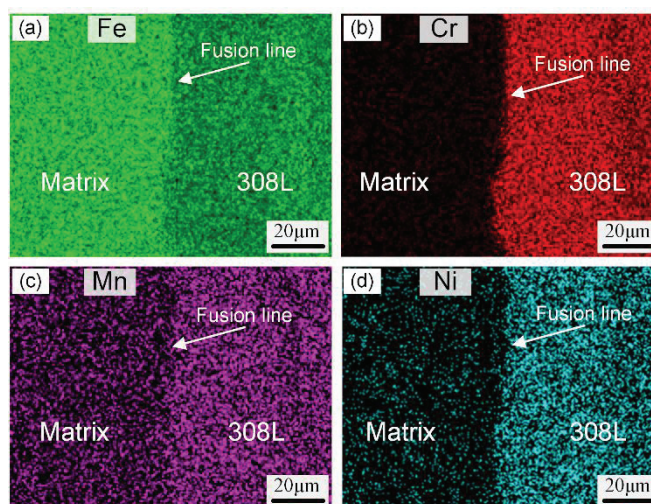


Figure 3-12. The corresponding EDS mappings for (a) Fe, (b) Cr, (c) Mn, and (d) Ni.

3.3.5 Phase compositions in the HAZ and the first cladding layer

Fig. 3-13 presents the XRD patterns obtained from the cladding layer and the HAZ of the substrate, respectively. As observed in Fig. 3-13, only two peaks, $\alpha(110)$ and $\alpha(200)$, are detected in the HAZ, which indicates that there is only BCC phase in the HAZ region of the substrate. The three austenite peaks with the highest integral strength in the cladding layer are $\gamma(111)$, $\gamma(220)$ and $\gamma(200)$. Two ferrite peaks, $\delta(110)$ and $\delta(200)$, are also detected. This indicates that the cladding layer is mainly composed of austenite and a small amount of δ ferrite, which is consistent with the findings of the microstructure in Fig. 3-3 and the phase diagram in Fig. 3-7.

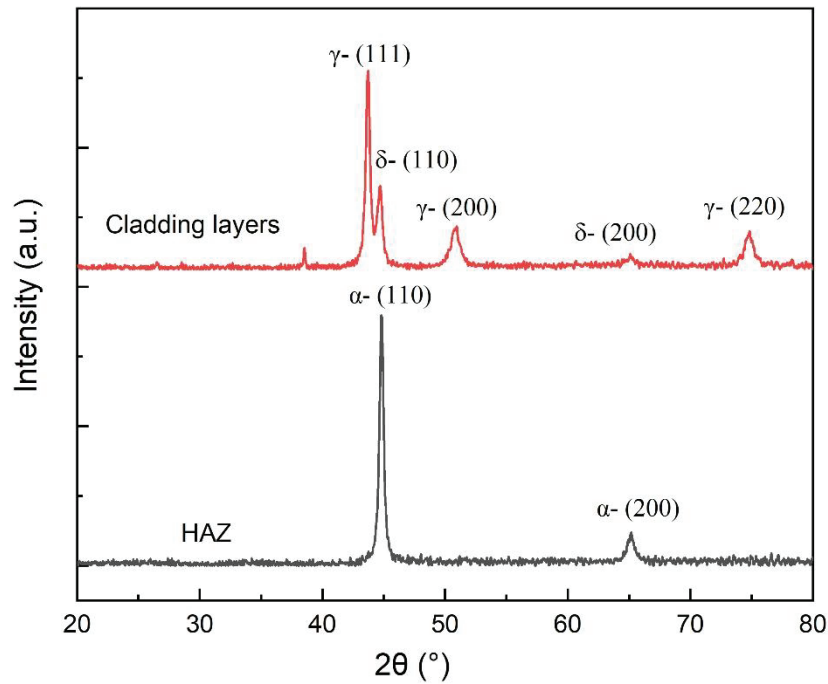


Figure 3-13. XRD patterns of the cladding layers and the HAZ in the substrate.

3.3.6 Microhardness

Microhardness has an essential influence on the wear resistance of materials^[2]. Three locations near the interface are selected for hardness testing, and the distribution of test points for the three sets of data (1, 2, 3) has been marked in the upper right corner of the figure. Vickers microhardness measurements are depicted in Fig. 3-14. The figure presents that the hardness changes obviously near the interface, with the highest hardness in and around the interface, with a maximum hardness of 218 HV5. As the distance to the interface increases, the hardness of both the substrate and the cladding layer shows a significant decrease. In sampling data 2 and 3, the hardness in the HAZ near the cladding layer is higher than the hardness at the interface, which is due to several reasons. The influence of element migration has been discussed in the previous section; The carbon migration near the interface increases the strength and hardness near the interface; the migration of Ni from the cladding layer to the substrate refines the grains, thereby increasing the strength. Furthermore, the laser cladding process also causes the microstructure transformation of the HAZ. During the cooling process, austenitic quenching results in the formation of harder martensite, which substantially

increases the hardness in this region. As is performed in Fig. 3-4, there is more slatted martensite in the HAZ.

Recrystallization leads to the decrease of grain size in the HAZ region, as shown in Fig 3-10. Most of the grains in the HAZ are small-size grains. According to the report, the hardness is inversely proportional to $d^{1/2}$, where d is the grain diameter^[18]. In other words, the smaller the grain size, the higher the hardness. Recrystallization also increases in the number of grain boundaries and higher grain boundaries' strength, limiting the movement of dislocations. The danger of repeating by Grain boundaries has proven to be the primary reinforcing mechanism for steel^[42]. According to the KAM diagram in Fig. 3-6, the KAM value of the HAZ is higher, and correspondingly, the dislocation density in this region is also higher. Combining Fig. 3-14 and Fig. 3-6, the regions with higher hardness all gather a large amount of LAGBs, indicating the enhancement effect of LAGBs on the strength. As sampling location 1 is close to the edge, the data points pass through a small area of the heat-affected zone and low martensite content, so the maximum hardness occurs at the interface with the smallest grain size.

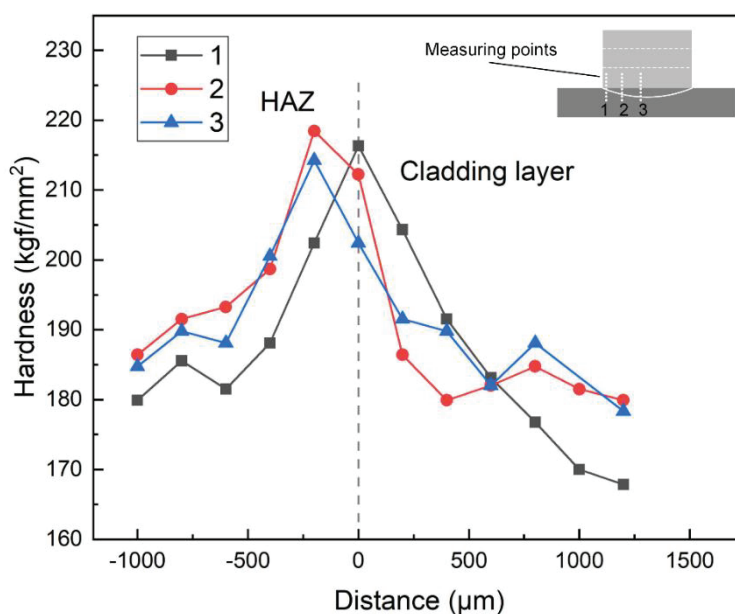


Figure 3-14. Microhardness profile of different areas across the interface.

In summary, the hardness increasing in the HAZ is caused by many factors, including element migration, microstructural transformation, changes in grain morphology, and dislocation density.

3.4 Discussion

3.4.1 Phase transformations

Fig. 3-3 presents that not only austenite but also δ ferrite precipitates in the 308L cladding layer. The content, morphology and distribution of δ ferrite in the cladding layer are related to the element composition of 308L stainless steel^[43]. The Schaeffler diagram is often used in research to predict δ -ferrite precipitate percentage in stainless steel^[43], as shown in Fig. 3-15. In Fig. 3-15, A is austenite, F is ferrite, M is martensite, and the horizontal coordinate indicates the Cr equivalents. The Cr equivalent can reflect the ferritization degree of laser cladding metal microstructure. Its value is according to the ferrite elements (such as chromium, molybdenum, silicon, copper, etc.) involved in the microstructure, converted into the sum according to the intensity of the ferrite action equivalent to several chromium. The formula is $Cr_{eq} = Cr + Mo + 1.5Si + 0.5Nb$ ^[43]. The Ni equivalent represents the vertical coordinate, reflecting the austenitizing degree of stainless steel cladding metal structure. Its value is according to the austenitic elements (such as nickel, carbon, manganese, etc.) contained in the cladding metal organization, converted to the equivalent of some nickel sums according to their intensity austenitizing effect. The formula is $Ni_{eq} = Ni + 30C + 0.5Mn$ ^[44]. According to calculation, the Cr_{eq} and Ni_{eq} of the cladding material 308L stainless steel in this study are 20.53 and 11.08, respectively. The position in Fig. 3-15 is marked with the red dot. The red dot position shows that the 308L stainless steel microstructures after solidification are austenite + ferrite, and the content of ferrite is 9%. This is essentially the same as the ferrite content we obtained from EBSD. According to EBSD, the ferrite content of 308L solidified tissue is 9.6%. The same results were found in other studies^[43].

On the other hand, researchers have reported four solidification modes based on the Cr_{eq} and Ni_{eq} ^[24]:

$$\text{A mode: } Cr_{eq}/Ni_{eq}(\text{in wt.}\%) < 1.25, L + \gamma \rightarrow \gamma \quad (3-2)$$

$$\text{AF mode: } 1.25 < Cr_{eq}/Ni_{eq}(\text{in wt.}\%) < 1.48, L + \gamma \rightarrow L + \gamma + \delta \rightarrow \gamma + \delta \quad (3-3)$$

$$\text{FA mode: } 1.48 < \text{Cr}_{\text{eq}}/\text{Ni}_{\text{eq}}(\text{in wt.}\%) < 1.95, \text{L} + \delta \rightarrow \text{L} + \delta + \gamma \rightarrow \delta + \gamma \quad (3-4)$$

$$\text{F mode: } 1.95 < \text{Cr}_{\text{eq}}/\text{Ni}_{\text{eq}}(\text{in wt.}\%), \text{L} + \delta \rightarrow \delta \quad (3-5)$$

Where L is the liquid, γ is austenite, and δ is delta-ferrite, respectively. The $\text{Cr}_{\text{eq}}/\text{Ni}_{\text{eq}}$ of the 308L cladding metal is 1.85. The $\text{Cr}_{\text{eq}}/\text{Ni}_{\text{eq}}$ of the 308L cladding metal is 1.85, indicating that the cladding metal's theoretical solidification mode is FA mode. During solidification, δ ferrite is the initial solidification phase and then transformed into austenite by a peritectic-eutectic reaction. As solidification progresses, most of the austenite replaces the initial ferrite until the temperature decreases and diffusion of elements is inhibited. After solidification, a small amount of ferrite is still not transformed into austenite, in the form of Lathy or skeletal, as shown in the metallographic diagram from Fig. 3-3. Previous studies have also demonstrated that the FA mode is the dominant solidification mode for austenitic stainless steels during laser cladding^[24, 45]. The microstructure after solidification is related to chemical composition and cooling rate, and heat treatment^[45]. The second and third cladding layers reheat the first layer during the cladding process, thus promoting element diffusion, with a decrease in δ -ferrite content and increasing austenite content. Fig. 3-3 b is the closest to the heat source, so the effect is the most obvious. The δ ferrite in Fig. 3-3 b is significantly less than that in Fig. 3-3 a.

It is worth mentioning that the austenite-ferrite (AF) solidification mode was also observed in localized areas, although the FA solidification mode was the dominant solidification mode in the cladding layer, as presented in Fig. 3-3 (e)-(h). Other studies have also found that FA mode and AF mode exist simultaneously in the same area^[46, 47]. In the solidification process of austenitic stainless steel, the cooling rate of the liquid metal determines the initial precipitation phase and solidification mode^[48]. Lin et al.^[49] reported that the AF mode dominated the solidification mode when the cooling rate was high because the austenitic phase (γ) as the dominant phase had higher stability. In addition, the substrate-to-cladding layer carbon migration that occurs at the boundary also leads to a lower $\text{Cr}_{\text{eq}}/\text{Ni}_{\text{eq}}$, which promotes the AF solidification mode^[18]. The different cooling rates of the cladding layers during solidification, and elemental

segregation lead to the coexistence of the FA and AF modes.

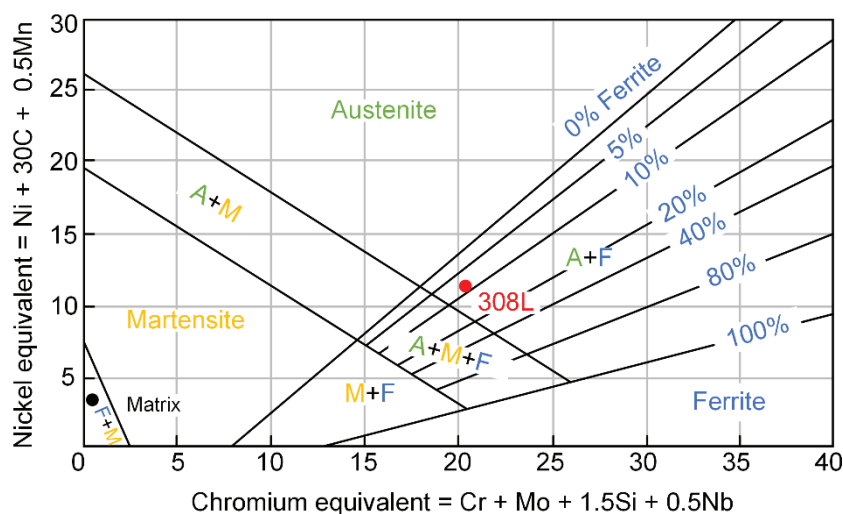


Figure 3-15. Schaeffler diagram^[50, 51].

3.4.2 The relationship between mechanical properties and microstructural features

The grain size data obtained from EBSD can also be used to predict the yield strength of the material. The relationship between grain size and strength generally obeys the Hall-Petch relationship. The Hall-Petch correlation is as follows^[29]:

$$\sigma_{HP} = \sigma_0 + k\alpha^{-1/2} \quad (3-6)$$

Where σ_{HP} is the yield strength, σ_0 is the friction stress constant which stands for the resistance of the lattice to dislocation; it is 527.44MPa obtained from empirical studies on steel^[42, 52], k is the Hall - Petch coefficient, which is 0.14MPa $m^{-1/2}$ obtained by fitting the least squares method^[42, 53], and α is the average grain size.

Each region's yield strength can be calculated using the average grain size data in Table 3-3, separately, as depicted in Table 3-4. It is worth noting that there is an inherent error in predicting the yield strength based on grain size using the Hall-Petch relationship equation. They are coupled with the fact that the coefficients used in Eq. (3-6) are not fully applicable to the materials in this study. Therefore, the dates in Table 3-4 are only predicted values, which may differ from the actual values and cannot be used as a strong indicator of yield strength. Despite the error, it is still possible to

compare and analyze the yield strength of different regions using this method. The view of dislocations can explain the role of grain size. It is known in crystal defects that dislocations are distributed in three dimensions in the crystal. The line segment of the dislocation network on the slip surface can become a dislocation source. Under stress, the dislocation source can continuously release dislocations, causing the crystal to slip. In the process of movement, barriers of the dislocation network must be overcome first. When the dislocation moves to the grain boundary, the grain boundary barriers must be overcome to transfer the deformation from one grain to another, leading to the object yielding. It follows that the yield strength of metal should depend on the force required to make the dislocation source act, the resistance given by the dislocation network to move the dislocation, and the resistance of the boundary between grains. Thus, the more refined the grain in the same metal volume, the more grain boundaries, and the more barriers. This requires an additional force to cause the crystal to slip. Therefore, the smaller the grain size, the greater the yield limit of the material. In summary, the correlation between the microstructure (grain size) and mechanical properties (yield strength) of the material can be established using the Hall-Petch relationship to demonstrate the effect of microstructure on mechanical properties^[54].

Table 3-4 The calculated yield strength of the regions of A, B, and C (MPa).

| | Region A | Region B | Region C |
|-----|----------|----------|----------|
| BCC | 598.33 | 595.91 | 600.62 |
| FCC | 555.78 | 563.50 | 564.00 |

As mentioned before, the texture has an important influence on the material properties, and there is a relationship between the texture and the yielding behavior of metallic materials, according to the Critical Resolved Shear Stress (CRSS) law^[55].

$$\mu = \tau_c / \sigma_s \tag{3-7}$$

Where μ is the tensile deformation orientation factor, and the value is equal to the product of the cosine of the angle between the tensile direction and the slip plane normal and slip directions, respectively; τ_c is the critical tangential stress, which is generally constant; σ_s is the yield strength. Eq. (3-7) presents that the yield stress and orientation

factor are inversely proportional; the larger the orientation factor, the smaller the yield strength. Fig. 3-16 and Fig. 3-17 provide the inverse pole figures of the three regions A, B and C in Fig. 3-6 using EBSD post-processing software. The contour lines represent the orientation factors, where preferred orientation is evident (red area). The larger orientation factor represents the value. Since FCC has a more pronounced preferred orientation than BCC, the maximum orientation factor is larger. According to Eq. (3-7), the yield strength of FCC is lower than that of BCC. This means that the yield strength on one side of the cladding layer is lower than that on the HAZ side. For the three regions of ABC, it can also be inferred from Fig. 3-9 and Fig. 3-16 that in BCC, since the crystal orientation in each region is close to randomly distributed, the maximum orientation factors of the three regions are not significantly different from each other, and the yield strength is not significantly different. The yield strength of region B in FCC is the smallest because of the significant orientation factor. The conclusion obtained by using Eq. (3-7) is consistent with the results in Table 3-4, which proves the accuracy of the relationship between texture and the yield behavior of metal materials and further proves the influence of microstructure on mechanical properties.

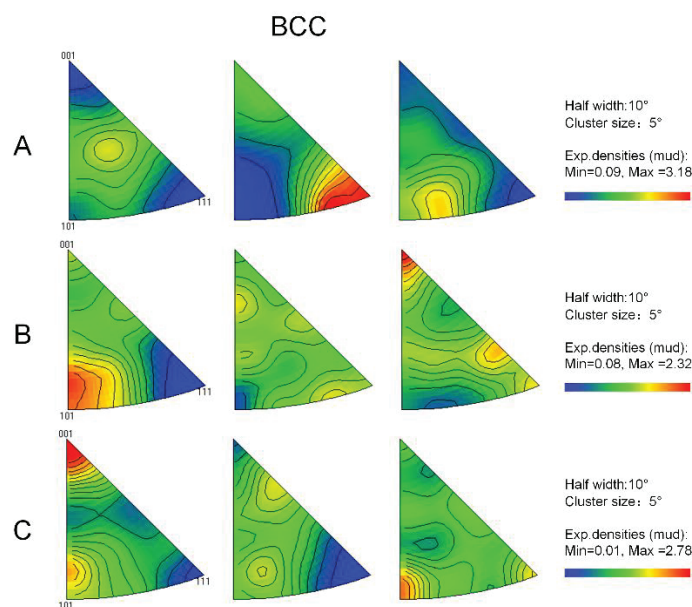


Figure 3-16. The inverse pole figures of BCC corresponding to the part of the HAZ in the A, B, and C area.

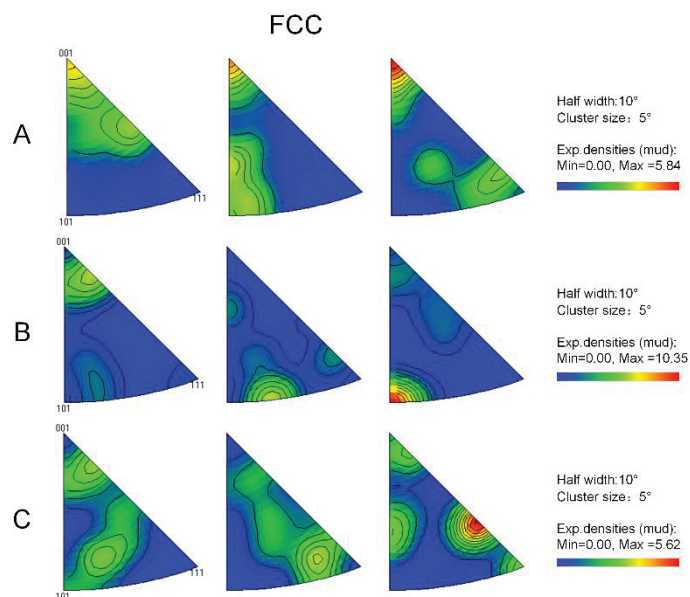


Figure 3-17. The inverse pole figures of FCC corresponding to the part of the cladding layer in the A, B, and C area.

3.5 Summary

308L stainless steel coatings are manufactured by laser hot wire cladding in this study. The microstructure evolution and microhardness change of the HAZ and the cladding layer near the interface were studied. The conclusions are drawn as follows:

- (1) 308L cladding layer consists mainly of dendritic austenite and columnar austenite, with δ -ferrite (content: 9%) distributed between the austenite grains. Equiaxed crystals are generated in the central region, and most of the columnar dendritic morphology in the edge region is located along the structural direction.
- (2) Both FA mode and AF mode exist in the cladding layer, and FA mode is the primary solidification mode. The coexistence of FA mode and AF mode is caused by the cladding layer's different cooling rates and element segregation during solidification.
- (3) The microstructure of the HAZ region consists mainly of ferrite and tempered bainite. Slatted martensite produced by recrystallization can be observed in the part near the interface, and the presence of martensite can be inferred both from the Schaeffler diagram and the EBSD data; The element migration at the interface not only enhances the transformation of martensite but also leads to a smaller grain size of HAZ.

No martensite was found in the substrate far away from the interface.

(4) The average grain size in the HAZ region is about 4 μm , while the average grain size in the cladding layer is above 14 μm ; Numerous factors such as smaller grain size, greater dislocation density, and microstructural transformation result in the highest HAZ hardness near the interface.

(5) Using the Hall-Petch relationship to establish the correlation between the material's microstructure (grain size) and mechanical properties (yield strength). The CRSS law proves the relationship between texture and yield behavior of metal materials, thus proving the influence of microstructure on mechanical properties.

3.6 References

- [1] K.Qi, Y. Yang, W. Liang, K. Jin, L. Xiong, Influence of the anomalous elastic modulus on the crack sensitivity and wear properties of laser cladding under the effects of a magnetic field and Cr addition, *Surf. Coat. Technol.* 423 (2021) 127575.
- [2] Z. Zhang, F. Kong, R. Kovacevic, Laser hot-wire cladding of Co-Cr-W metal cored wire, *Opt. Laser Eng.* 128 (2020) 105998.
- [3] S. Zhou, T. Xu, C. Hu, H. Wu, H. Liu, X. Ma, Effect of different topologies on microstructure and mechanical properties of multilayer coatings deposited by laser cladding with Inconel 625 wire, *Surf. Coat. Technol.* 421 (2021) 127299.
- [4] P. Wen, Z. Cai, Z. Feng, G. Wang, Microstructure and mechanical properties of hot wire laser clad layers for repairing precipitation hardening martensitic stainless steel, *Opt. Laser Technol.* 75 (2015) 207-213.
- [5] A. Khorram, Microstructural evolution of laser clad Stellite 31 powder on Inconel 713 LC superalloy, *Surf. Coat. Technol.* 423 (2021) 127633.
- [6] J.L. Bartlett, X. Li, An overview of residual stresses in metal powder bed fusion, *Addit. Manuf.* 27 (2019) 131-149.
- [7] S. Liu, W. Liu, M. Harooni, J. Ma, R. Kovacevic, Real-time monitoring of laser hot-wire cladding of Inconel 625, *Opt. Laser Technol.* 62 (2014) 124-134.
- [8] E. Brandl, V. Michailov, B. Viehweger, C. Leyens, Deposition of Ti-6Al-4V using

laser and wire, part I: Microstructural properties of single beads, *Surf. Coat. Technol.* 206(6) (2011) 1120-1129.

[9] T.E. Abioye, D.G. McCartney, A.T. Clare, Laser cladding of Inconel 625 wire for corrosion protection, *J. Mater. Process. Technol.* 217 (2015) 232-240.

[10] X. Xu, G. Mi, L. Chen, L. Xiong, P. Jiang, X. Shao, C. Wang, Research on microstructures and properties of Inconel 625 coatings obtained by laser cladding with wire, *J. Alloy. Compd.* 715 (2017) 362-373.

[11] P. Wen, Z. Feng, S. Zheng, Formation quality optimization of laser hot wire cladding for repairing martensite precipitation hardening stainless steel, *Opt. Laser Technol.* 65 (2015) 180-188.

[12] J. Nurminen, J. Riihimäki, J. Näkki, P. Vuoristo, Comparison of laser cladding with powder and hot and cold wire techniques, *ICALEO 2006 - 25th International Congress on Applications of Laser and Electro-Optics, Congress Proceedings, 2006* 4.

[13] J. Nurminen, J. Riihimäki, J. Näkki, P. Vuoristo, Hot-wire cladding process studies, *International Congress on Applications of Lasers & Electro-Optics, Laser Institute of America, 2007*, p. 1702.

[14] S. Liu, W. Liu, R. Kovacevic, Experimental investigation of laser hot-wire cladding, *Proceedings of the Institution of Mechanical Engineers, Part B: J. Eng. Manuf.* 231(6) (2017) 1007-1020.

[15] W. Li, K. Sugio, X. Liu, M. Yamamoto, Y. Guo, S. Zhu, G. Sasaki, Microstructure evolution and mechanical properties of 308L stainless steel coatings fabricated by laser hot wire cladding, *Mater. Sci. Eng. A* 824 (2021) 141825.

[16] B.O. Okonkwo, H. Ming, J. Wang, F. Meng, X. Xu, E.-H. Han, Microstructural characterization of low alloy steel A508 – 309/308L stainless steel dissimilar weld metals, *Int. J. Pressure Vessels Piping* 190 (2021) 104297.

[17] L. Dong, C. Ma, Q. Peng, E.-H. Han, W. Ke, Microstructure and stress corrosion cracking of a SA508-309L/308L-316L dissimilar metal weld joint in primary pressurized water reactor environment, *J. Mater. Sci. Technol.* 40 (2020) 1-14.

[18] H. Ming, Z. Zhang, J. Wang, E.-H. Han, W. Ke, Microstructural characterization

of an SA508–309L/308L–316L domestic dissimilar metal welded safe-end joint, *Mater. Charact.* 97 (2014) 101-115.

[19] H. Ming, Z. Zhang, J. Wang, E.-H. Han, Microstructure of a domestically fabricated dissimilar metal weld joint (SA508-52M-309L-CF8A) in nuclear power plant, *Mater. Charact.* 148 (2019) 100-115.

[20] Q. Xiong, H. Li, Z. Lu, J. Chen, Q. Xiao, J. Ma, X. Ru, Characterization of microstructure of A508III/309L/308L weld and oxide films formed in deaerated high-temperature water, *J. Nucl. Mater.* 498 (2018) 227-240.

[21] S. Zhu, Y. Nakahara, H. Aono, R. Ejima, M. Yamamoto, Derivation of Appropriate Conditions for Additive Manufacturing Technology Using Hot-Wire Laser Method, *Mate. P.* 3(1) (2021) 9.

[22] X. Xu, G. Mi, Y. Luo, P. Jiang, X. Shao, C. Wang, Morphologies, microstructures, and mechanical properties of samples produced using laser metal deposition with 316 L stainless steel wire, *Opt. Laser Eng.* 94 (2017) 1-11.

[23] X. Xu, G. Mi, L. Xiong, P. Jiang, X. Shao, C. Wang, Morphologies, microstructures and properties of TiC particle reinforced Inconel 625 coatings obtained by laser cladding with wire, *J. Alloy. Compd.* 740 (2018) 16-27.

[24] K. Li, D. Li, D. Liu, G. Pei, L. Sun, Microstructure evolution and mechanical properties of multiple-layer laser cladding coating of 308L stainless steel, *Appl. Surf. Sci.* 340 (2015) 143-150.

[25] M. Li, T. Lu, J. Dai, X. Jia, X. Gu, T. Dai, Microstructure and mechanical properties of 308L stainless steel fabricated by laminar plasma additive manufacturing, *Mater. Sci. Eng. A* 770 (2020) 138523.

[26] X. Lin, E.-H. Han, Q. Peng, W. Ke, Z. Jiao, Effect of post-irradiation annealing on microstructure and corrosion of proton-irradiated 308L stainless steel weld metal, *Corros. Sci.* 175 (2020) 108887.

[27] J.W. Fu, Y.S. Yang, J.J. Guo, Formation of a blocky ferrite in Fe-Cr-Ni alloy during directional solidification, *J Cryst. Growth* 311(14) (2009) 3661-3666.

[28] W. Zhong, J.-L. Lin, Y. Chen, Z. Li, K. An, B.J. Sutton, B.J. Heuser, Microstructure, Hardness, and Residual Stress of the Dissimilar Metal Weldments of SA508-

- 309L/308L-304L, *Metall. Mater. Trans. A* 52(5) (2021) 1927-1938.
- [29] B. Gwalani, V. Soni, M. Lee, S. Mantri, Y. Ren, R. Banerjee, Optimizing the coupled effects of Hall-Petch and precipitation strengthening in a Al_{0.3}CoCrFeNi high entropy alloy, *Mater. Des.* 121 (2017) 254-260.
- [30] Y. Fu, N. Guo, C. Zhou, G. Wang, J. Feng, Investigation on in-situ laser cladding coating of the 304 stainless steel in water environment, *J. Mater. Process. Technol.* 289 (2021) 116949.
- [31] L. Song, G. Zeng, H. Xiao, X. Xiao, S. Li, Repair of 304 stainless steel by laser cladding with 316L stainless steel powders followed by laser surface alloying with WC powders, *J. Manuf. Process.* 24 (2016) 116-124.
- [32] K. Fujiyama, K. Mori, D. Kaneko, H. Kimachi, T. Saito, R. Ishii, T. Hino, Creep damage assessment of 10Cr-1Mo-1W-VNbN steel forging through EBSD observation, *Int. J. Pressure Vessels Piping* 86(9) (2009) 570-577.
- [33] S. Rawat, B. Singh Rawat, A. Gupta, M. Kumar Pathak, A. Joshi, P. Rawat, P. Kumar Pant, EBSD studies on cryorolled LM6 Al alloy, *Mater. Today: Proc.* 44 (2021) 1969-1974.
- [34] N. Kumar, P.N. Rao, R. Jayaganthan, H.-G. Brokmeier, Effect of cryorolling and annealing on recovery, recrystallisation, grain growth and their influence on mechanical and corrosion behaviour of 6082 Al alloy, *Mater. Chem. Phys.* 165 (2015) 177-187.
- [35] K.-I. Sugimoto, M. Kobayashi, S.-I. Hashimoto, Ductility and strain-induced transformation in a high-strength transformation-induced plasticity-aided dual-phase steel, *Metall. Trans. A* 23(11) (1992) 3085-3091.
- [36] M. Mukherjee, T.K. Pal, Influence of Heat Input on Martensite Formation and Impact Property of Ferritic-Austenitic Dissimilar Weld Metals, *J. Mater. Sci. Technol.* 28(4) (2012) 343-352.
- [37] H.J. Bunge, R. Kiewel, T. Reinert, L. Fritsche, Elastic properties of polycrystals— influence of texture and stereology, *J. Mech. Phys. Solids* 48(1) (2000) 29-66.
- [38] M. Da Cunha Belo, M. Walls, N.E. Hakiki, J. Corset, E. Picquenard, G. Sagon, D. Noël, Composition, structure and properties of the oxide films formed on the stainless

- steel 316L in a primary type PWR environment, *Corros. Sci.* 40(2-3) (1998) 447-463.
- [39] W. Kuang, X. Wu, E.H. Han, Influence of dissolved oxygen concentration on the oxide film formed on 304 stainless steel in high temperature water, *Corros. Sci.* 63 (2012) 259-266.
- [40] T. Sarikka, M. Ahonen, R. Mougnot, P. Nevasmaa, P. Karjalainen-Roikonen, U. Ehrnstén, H. Hänninen, Microstructural, mechanical, and fracture mechanical characterization of SA 508-Alloy 182 dissimilar metal weld in view of mismatch state, *Int. J. Pressure Vessels Piping* 145 (2016) 13-22.
- [41] K.-H. Lee, S.-g. Park, M.-C. Kim, B.-S. Lee, D.-M. Wee, Characterization of transition behavior in SA508 Gr.4N Ni–Cr–Mo low alloy steels with microstructural alteration by Ni and Cr contents, *Mater. Sci. Eng. A* 529 (2011) 156-163.
- [42] K. Mao, H. Wang, Y. Wu, V. Tomar, J.P. Wharry, Microstructure-property relationship for AISI 304/308L stainless steel laser weldment, *Mater. Sci. Eng. A* 721 (2018) 234-243.
- [43] Z. Li, X. Zhan, X.-M. Bai, S.-C. Lee, W. Zhong, B.J. Sutton, B.J. Heuser, Modified microstructures in proton irradiated dual phase 308L weldment filler material, *J. Nucl. Mater.* 548 (2021).
- [44] Q. Wang, S. Zhang, C. Zhang, C. Wu, J. Wang, J. Chen, Z. Sun, Microstructure evolution and EBSD analysis of a graded steel fabricated by laser additive manufacturing, *Vacuum* 141 (2017) 68-81.
- [45] Y. Fu, N. Guo, C. Zhou, G. Wang, J. Feng, Investigation on in-situ laser cladding coating of the 304 stainless steel in water environment, *J. Mater. Process. Technol.* 289 (2021) 116949.
- [46] M. Sireesha, V. Shankar, S.K. Albert, S. Sundaresan, Microstructural features of dissimilar welds between 316LN austenitic stainless steel and alloy 800, *Mater. Sci. Eng. A* 292(1) (2000) 74-82.
- [47] R. Dehmolaei, M. Shamanian, A. Kermanpur, Microstructural characterization of dissimilar welds between alloy 800 and HP heat-resistant steel, *Mater. Charact.* 59(10) (2008) 1447-1454.
- [48] S.B. Tate, S. Liu, Solidification behaviour of laser welded type 21Cr–6Ni–9Mn

- stainless steel, *Sci. Technol. Weld. Joining* 19(4) (2014) 310-317.
- [49] X. Lin, H. Yang, J. Chen, W. Huang, Microstructure evolution of 316L stainless steel during laser rapid forming, *Acta Metall. Sin. (Chin. Ed.)* 42(4) (2006) 361.
- [50] A.L. Schaeffler, Constitution diagram for stainless steel weld metal, *Met. Prog.* 56(11) (1949) 680.
- [51] S. Kou, *Welding metallurgy*, New Jersey, USA 431(446) (2003) 223-225.
- [52] M.-Y. Seok, I.-C. Choi, J. Moon, S. Kim, U. Ramamurty, J.-i. Jang, Estimation of the Hall–Petch strengthening coefficient of steels through nanoindentation, *Scripta Materialia* 87 (2014) 49-52.
- [53] N. Nakada, M. Fujihara, T. Tsuchiyama, S. Takaki, Effect of Phosphorus on Hall-Petch Coefficient in Ferritic Steel, *ISIJ Int.* 51(7) (2011) 1169-1173.
- [54] E. Ghassemali, M.-J. Tan, C.B. Wah, S.C.V. Lim, A.E.W. Jarfors, Effect of cold-work on the Hall–Petch breakdown in copper based micro-components, *Mech. Mater.* 80 (2015) 124-135.
- [55] W. Mao, P. Yang, Chen, Leng, *Material texture analysis principle and detection technology*, Metallurgical Industry Press, Beijing, 2008,21-22, (in Chinese).

Chapter 4

Temperature Field Simulation and Solidification Structure During Laser Hot Wire Cladding Process

| | | |
|-------|---|-----|
| 4.1 | Introduction | 103 |
| 4.2 | Finite element modeling..... | 105 |
| 4.2.1 | Heat conduction equation and heat source model..... | 105 |
| 4.2.2 | Laser hot wire cladding process..... | 106 |
| 4.2.3 | Model description..... | 107 |
| 4.2.4 | Laser cladding simulation procedure..... | 107 |
| 4.3 | Results and discussion..... | 108 |
| 4.3.1 | Temperature field simulation results..... | 108 |
| 4.3.2 | Experimentally obtained microstructure..... | 111 |
| 4.3.3 | Crystal orientation..... | 113 |
| 4.4 | Summary..... | 115 |
| 4.5 | References..... | 116 |

4.1 Introduction

Laser hot wire cladding (LHWC) is an advanced additive manufacturing technology. Compared to powder-fed systems, LHWC has higher material utilization (almost 100%), lower costs, and less contamination^[1, 2]. Compared to conventional wire cladding, the LHWC system has a separate wire preheating source in addition to the laser energy source. The wire is heated to the temperature near the melting point, and then fed into the melt pool. Finally, the cladding layer is formed after solidification. This method reduces the dependence on high laser power, reduces heat input, and lowers dilution rates, thus minimizing defects and improving the quality and mechanical properties of the coating^[3, 4]. Therefore, this technology is widely used in additive manufacturing and surface repair^[5-8].

The highly localized solidification, rapid cooling rates, directional thermal gradients, and cyclic heat treatment of the molten cladding layer leads to complex, hierarchical microstructures^[9, 10]. These include fine solidification structures, site-specific elemental assignments and oriented solidification grains with a strong crystallographic texture^[11, 12]. In addition, due to the strong Marangoni convection in the melt pool (maximum velocity over 100 mm/s), the metal liquid is circulated several times before solidification^[4, 13]. This phenomenon significantly leads to the redistribution of elements, promotes the dissolution of high melting point particles, and further affects the solidification microstructure controlled by thermal parameters and solute concentration during solidification^[14, 15]. The complex microstructure inevitably leads to different textures, which affect the mechanical properties of materials. Consequently, it is essential to understand the solidification process of the cladding layer to control its performance^[4, 16].

Owing to the local high temperature and the complex transient characteristics, it is difficult to directly observe the temperature change and thermal cycle inside the molten material during the solidification process by conventional experimental method^[17, 18]. Many researchers have used numerical simulations to investigate the laser cladding

process^[19, 20]. In previous studies, researchers had developed various models to study the laser cladding process.

Zuo et al^[21]. established a three-dimensional temperature field model to explore the relationship between thermal behavior and grain evolution during laser cladding. The results show that the grain growth pattern along the deposited part is different in the multilayer deposition process, and the grain growth behavior of multilayer is different from that of the single layer. Li et al^[22]. analyzed and modeled the complete shape in the process of laser hot wire cladding. The model was experimentally validated to predict the full orbital profile based on process parameters and interfacial tensions between different phases. Song et al^[14]. established a new numerical model of laser cladding based on previous work. The model systematically reveals the relationship between laser-substrate-powder. In addition, the solidification process of the cladding layer and its macroscopic solidification morphology were analyzed based on the obtained thermal history. Mukherjee et al^[23]. calculated the residual stresses and transient temperature fields using a three-dimensional transient heat transfer and fluid flow model and compared the calculated results with experimental results. The results show that residual stresses can be significantly reduced by reducing the layer thickness during AM. Nie et al^[9]. developed a thermomechanical FEA model for laser hot wire(LHW) additive manufacturing numerical simulation. To validate the FEA model, temperature changes and substrate deformation were measured with thermocouples. The validation results show that the LHW model is feasible and accurate. Wei et al^[24]. proposed a comprehensive multiphase model to elucidate the evolution of the gas-liquid-solid interface during laser hot wire deposition. The simulation results include the geometry of the melt pool and cladding layer, the Marangoni outward flow effect, and the temperature evolution during deposition.

Although there are many relevant finite element models, the laser heat source model used in currently finite element simulation studies is mostly the Gaussian distribution model, which corresponds to a circular heat source, and there is a lack of relevant studies of rectangular laser heat sources. In addition, most of the models developed in current studies are designed to simulate the cladding process and predict

the trajectory shape, however, there are few studies on the effect of temperature field on the solidification microstructure morphology and crystal orientation.

Numerical simulation is an effective research method for demonstrating the change in coating temperature during laser cladding. The finite element model constructed in this paper used a heat source model specifically for rectangular laser heat sources. The temperature field evolution during the LHWC process was obtained, and the formation process of solidified microstructure was analyzed based on the microstructure obtained in the experiment. The influence of temperature field on the properties of solidified microstructure (grain morphology, grain size, and crystal orientation) was discussed.

4.2 Finite element modeling

4.2.1 Heat conduction equation and heat source model

The governing equation of heat transfer LHWC process is given as follows^[25]:

$$\nabla \cdot (k(T)\nabla T) + Q = \rho(T)c_p(T) \frac{\partial T}{\partial t} \quad (4-1)$$

where ρ , c_p and k are temperature-dependent density, specific heat capacity and thermal conductivities, respectively; T is the temperature; Q denotes the heat input of the laser heat source. The values of the above parameters are listed in the Table 4-1.

Table 4-1 Coefficients for density, specific heat and conductivity of 308L wire and KD-40 substrate.

| Materials | Specific heat capacity(c_p) [J/(kg·°C)] | Thermal Conductivity(k) [W/(m·°C)] | Density(ρ) [g/cm ³] |
|-----------|--|---|---|
| SUS308L | 500 | 15 | 7.93 |
| KD-40 | 460 | 34 | 7.85 |

The rectangular spot heat source equation is shown as follows:

$$Q = \begin{cases} \frac{\eta\beta P}{w \times l}, & -\frac{w}{2} \leq x \leq \frac{w}{2} \text{ and } -\frac{l}{2} \leq z - vt \leq \frac{l}{2} \\ 0, & \text{others} \end{cases} \quad (4-2)$$

where β is the absorption rate of the laser heat source; η is the efficiency of the laser heat source; P is the laser power; and w is the width of the rectangular spot; l is the

length of the rectangular spot; v is the laser scanning speed. The values of these parameters are listed in Table 4-2.

Table 4-2 Parameters of the heat source model.

| Absorption rate(β) | Efficiency of the laser heat source (η) | Laser power(P) [kW] | Laser scanning speed (v) [m/min] | Rectangular spot width(w) [mm] | Rectangular spot length(l) [mm] |
|----------------------------|--|-------------------------|--------------------------------------|------------------------------------|-------------------------------------|
| 0.4 | 0.8 | 5.5 | 0.36 | 1.6 | 11 |

4.2.2 Laser hot wire cladding process

The LHWC experiments in this study were conducted on an experimental platform built by ourselves. The schematic diagram of the LHWC process is shown in Fig. 4-1. Some of the experimental parameters are presented in Table 4-2. The most significant difference between this set of experimental equipment and the common LHWC device is that the laser source is a rectangular diode laser with 1.6mm*11mm. It can deliver more energy and produce larger coating size. After the diode laser heat source irradiated the substrate, the substrate was melted, and the molten pool was formed. The wire feeder nozzle continuously transported the wire heated by the electric heater into the melt pool, solidifying it to create the cladding layer.

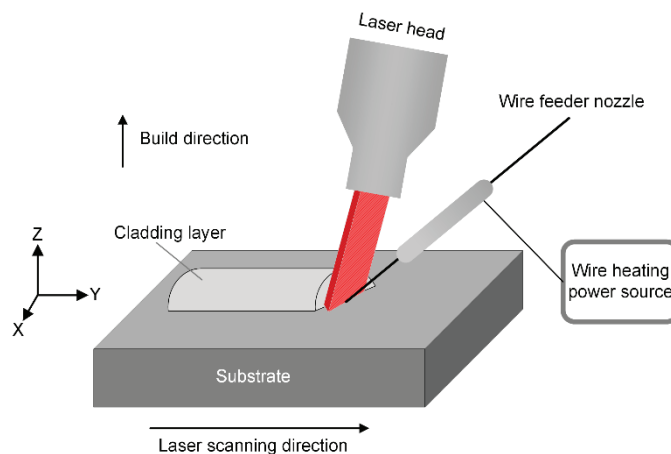


Figure 4-1. The schematic diagram of LHWC process used in this study.

4.2.3 Model description

Fig. 4-2 presents the schematic diagram of the laser clad sample drawn using ABAQUS simulation software, the model size is the same as the sample size in the experiment. The mesh density of the model determines the calculation accuracy and time. Different meshing strategies were adopted for the substrate and the cladding layer to save the calculation time, reduce the calculation cost, and ensure calculation accuracy. Since this study mainly explores the temperature field variation of the cladding layer, the accuracy of the substrate is not very high. Therefore, the meshes in the substrate are sparse, whereas the meshes in the cladding layers are dense. The total numbers of nodes and elements are 30,834 and 26,675, respectively. The ambient temperature was set to 20°C, and the substrate preheating temperature was 900°C.

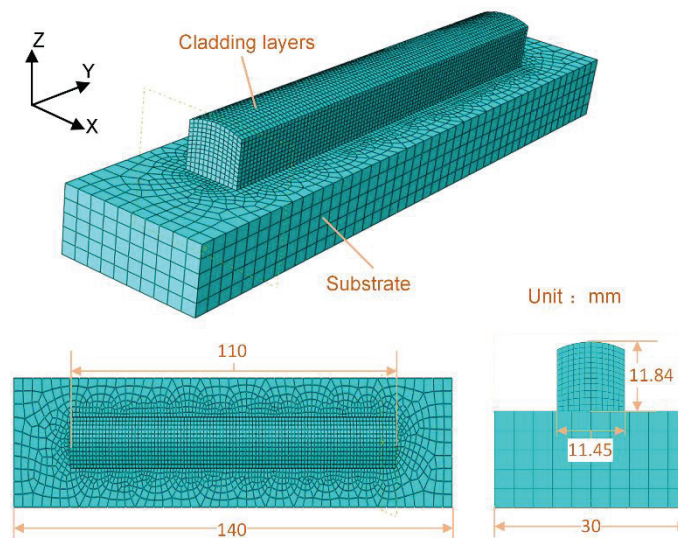


Figure 4-2. The established three-dimensional finite element model.

4.2.4 Laser cladding simulation procedure

Before printing, all units of the cladding layer were converted to inactive units. As the heat source moved, the inactive blocks were activated one by one, layer by layer. Therefore, Stepwise Activated Approach could simulate the process of gradual melting

and solidification deposition of materials, as shown in Fig. 4-3.

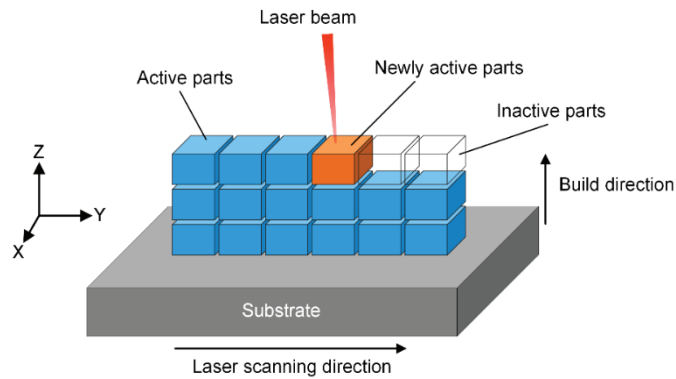


Figure 4-3. The schematic diagram of LHWC performed using a stepwise activated approach^[25].

4.3 Results and discussion

4.3.1 Temperature field simulation results

Fig. 4-4 reflects the temperature fields when the heat source moves to the first, second, and third layers. Two typical feature points in the center and edge of each layer are selected to make temperature change curves, as depicted in Fig. 4-5. The laser beam has high energy and is very concentrated. At the beginning of cladding, the laser beam shined on the substrate and formed a molten pool, and the temperature raised rapidly. As the laser beam moved away, the melt pool began to solidify. The heat was transmitted through heat conduction, heat convection, and heat radiation during solidification, and the temperature gradually decreased. It is worth noting that the heat of the rectangular diode laser heat source is not uniformly distributed inside the rectangle but is similar to the Gaussian distribution: high in the central region and low at the edges. Therefore, the temperature at the center was higher than the temperature at the edges.

Owing to the layer-by-layer cladding, the initially formed cladding layer acted as a preheat when the new cladding layer was formed, resulting in a higher peak temperature of the new cladding layer, indicating the heat accumulation in the rapid cladding process^[26]. At the same time, the new cladding layer transferred heat to the bottom layer again, and the temperature of the initially formed cladding layer went

through the process of rising and falling again, resulting in a thermal cycle. This was an important reason for the complex microstructure of solidified microstructure. It is clear from the temperature change curves that the cooling rate differs at different locations, which results in different solidification structures. The corresponding relationship is detailed in the following paragraphs.

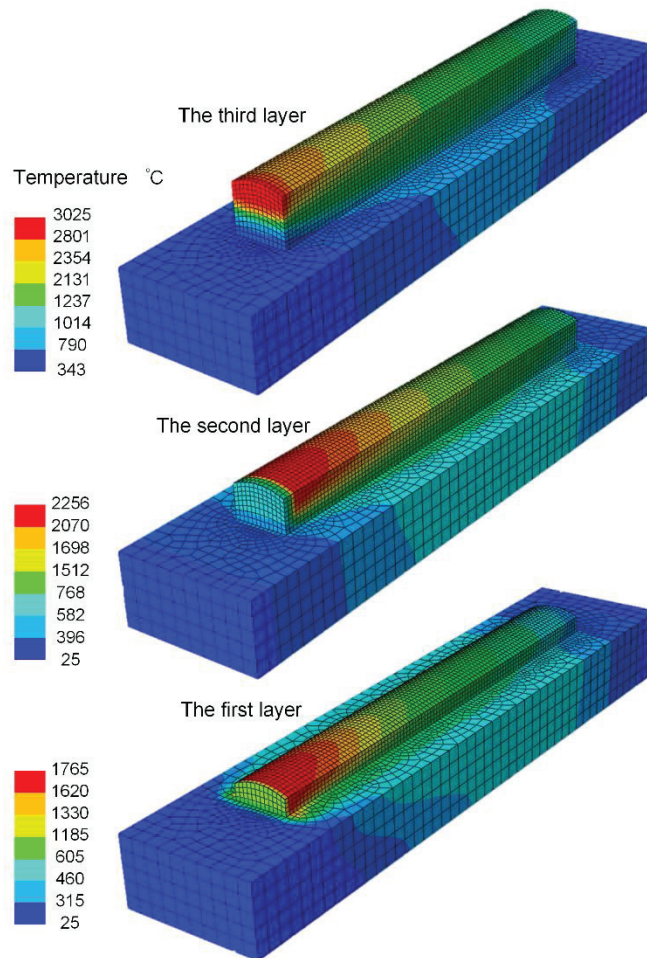


Figure 4-4. Temperature field simulation with different layers.

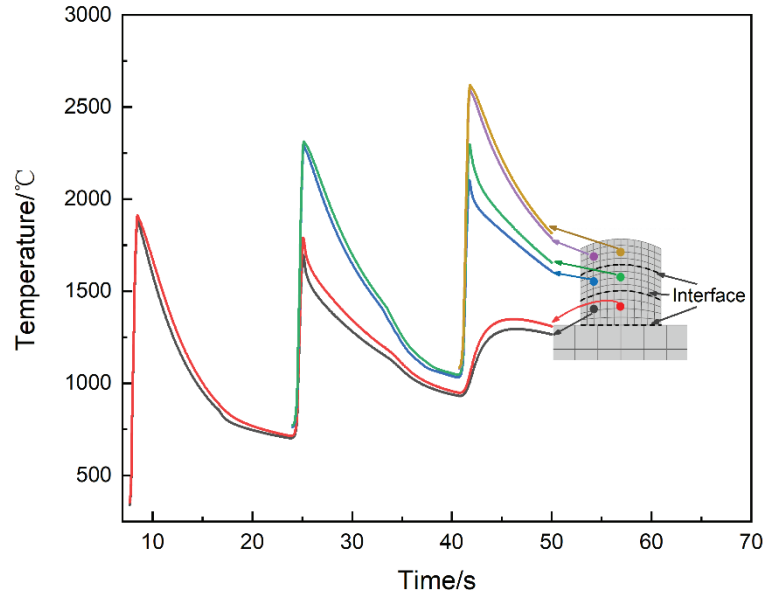


Figure 4-5. Thermal cycles at specific points of the cross-section.

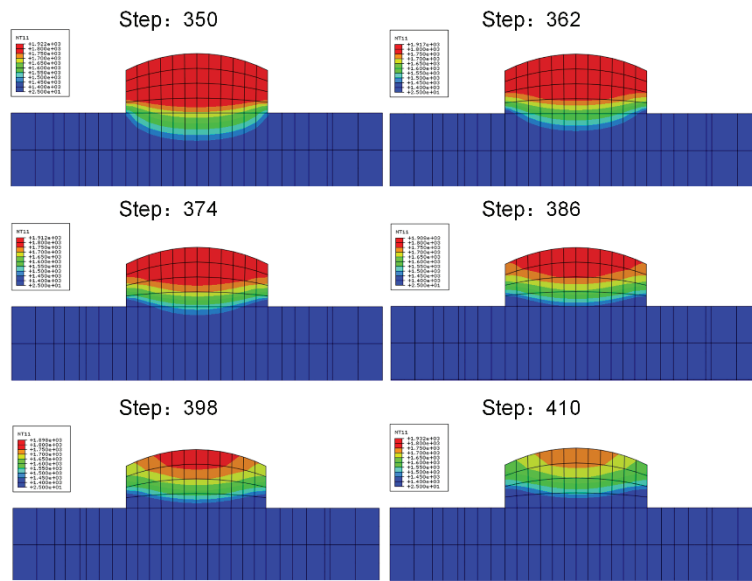


Figure 4-6. Temperature change during cooling of the first cladding layer.

To intuitively observe the temperature change process of the cladding layer, the cross section of the first cladding layer was selected to show the temperature field change process, as illustrated in Fig. 4-6. The numbers in the figure are simulated steps, which represent the time change. From the changes in the temperature field, the temperature of the part of the clad layer near the substrate decreased faster, and the temperature decreased the slowest inside and on top of the clad layer. This shows that in the cooling process of the cladding layer, the heat was mainly transferred down in

the way of heat conduction, and the heat dissipation was slow at the top in contact with the air, so the heat was most concentrated. This is consistent with previous study^[27]. Fig. 4-5 shows that the temperature profile trends of the second and third layers are similar to those of the first layer, indicating that the heat dissipation is similar to that of the first layer. In the cladding layer inside, The temperature drops faster in the edge region, indicating a faster cooling rate.

4.3.2 Experimentally obtained microstructure

Fig. 4-7 shows the microstructures of different regions of the cross section of the sample obtained by metallography. The light-colored area is austenite and the dark area is δ ferrite. Our previous study described experimental methods for obtaining microstructure in detail^[28]. The six typical regions selected for the microstructure correspond to the six regions of the output temperature curve in Fig. 4-5. The grain morphology of the central region is close to the equiaxed crystal, while the columnar crystal structure grew along the structural direction in the edge region, which is most apparent in the first and second cladding layers, as performed in Fig. 4-7. In other words, there is a columnar-to-equiaxed transition (CET) from the edge to the center of the coating. It is shown that the temperature gradient and solidification rate at the solid-liquid interface affect the CET. The appearance of columnar tissue depends on the following equation^[29]:

$$\frac{G^n}{R} > K_{CET} = \alpha \left\{ \sqrt[3]{\frac{-4\pi N_0}{3 \ln(1-M)} \frac{1}{n+1}} \right\}^n \quad (4-3)$$

where G is the temperature gradient; R is the solidification rate of the columnar front; n and α are material dependent parameters; K_{CET} is the critical value of CET; N_0 is the nucleation density in the liquid; The parameter M is defined as the critical value of areal fraction ahead of the advancing solidification front that is comprised of newly nucleated grains.

According to Eq. (4-3), when the G^n/R is large in a region, it is easier to form columnar crystal structure. On the contrary, the grains are mainly equiaxed crystal grains. The temperature gradient of the first cladding from the edge to the center is

demonstrated in Fig. 4-8. The temperature gradient results in a significant spatial gradient of surface tension, which drives the Marangoni flow of liquid metal and promotes thermal convection in the molten pool^[19]. The temperature gradient at the edge of the coating was the largest, thus the edge area is dominated by columnar crystals. From the edge to the center, the temperature gradient became smaller and smaller and gradually reached the boundary of CET. The microstructure gradually turned to be dominated by equiaxed crystals.

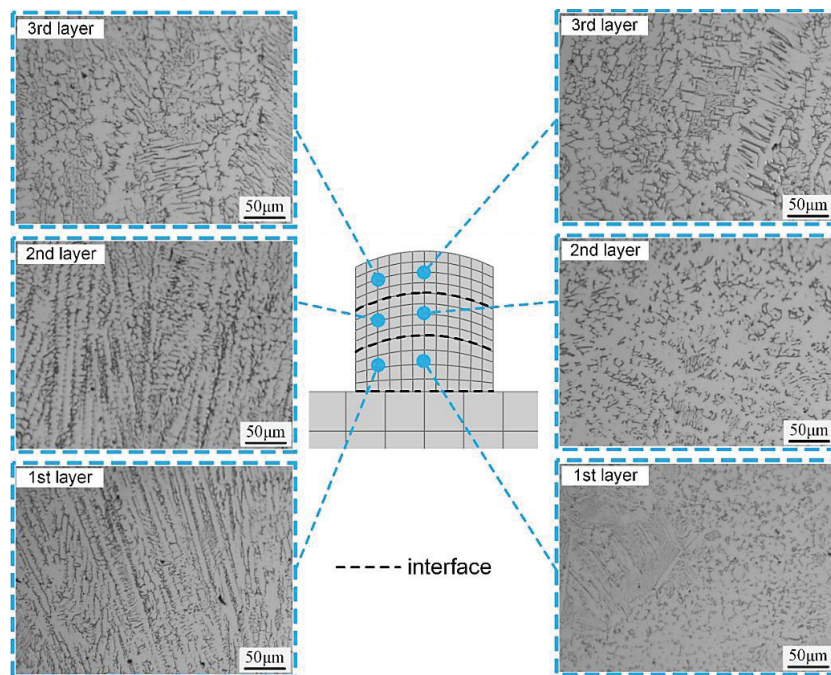


Figure 4-7. The microstructure of the cladding layers specific area obtained by the experiment.

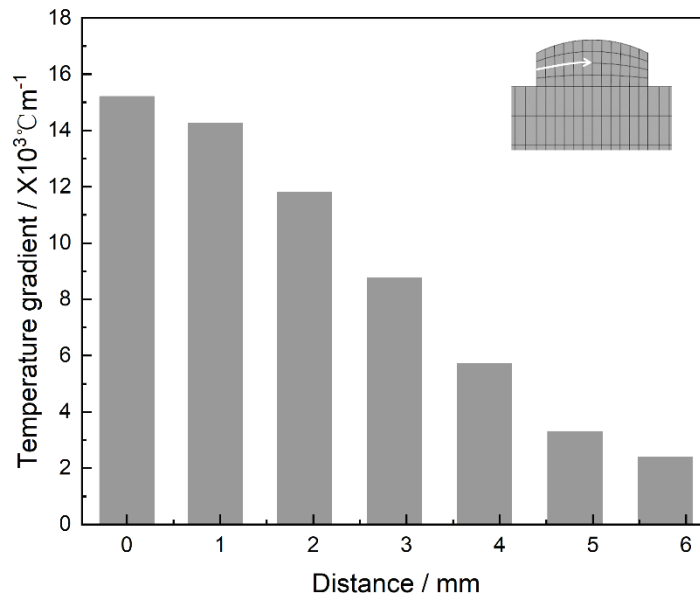


Figure 4-8. Temperature gradient from edge to the center.

4.3.3 Crystal orientation

Electronic backscatter diffraction (EBSD) technology can measure and analyze crystal orientation, micro-texture, and grain size in a huge area to characterize the solidification characteristics of the coating comprehensively^[30]. In this study, the EBSD Euler color orientation map of the whole sample cross-section was obtained by the EBSD technique, as shown in Fig. 4-9. Full Euler angular diagrams are commonly used to present crystal orientation information. According to the crystal symmetry, the Euler angles of different crystalline systems take different ranges^[31]. Different colors are assigned when the orientation difference between the proximal points is more than 10°. Therefore, the color difference in the figure represents the different orientation of the crystals. The smaller the color difference is, the more consistent the orientation of the two grains is, indicating the stronger crystal preferred orientation (texture). Generally, the texture is weak with a concentration of equiaxed crystals and strong in the regions with more columnar crystals. This is also demonstrated in Fig. 4-9, in the edge regions, where the texture is stronger, the columnar crystals are more concentrated. Peng et al^[32] pointed out that the temperature gradient components perpendicular to the melt pool boundary are higher than those along the other directions, leading to directional grain

growth. It is also clear from the figure that the columnar grains in each layer almost grow along the direction perpendicular to the fusion line, which is parallel to the temperature gradient direction caused by the substrate's cooling effect.

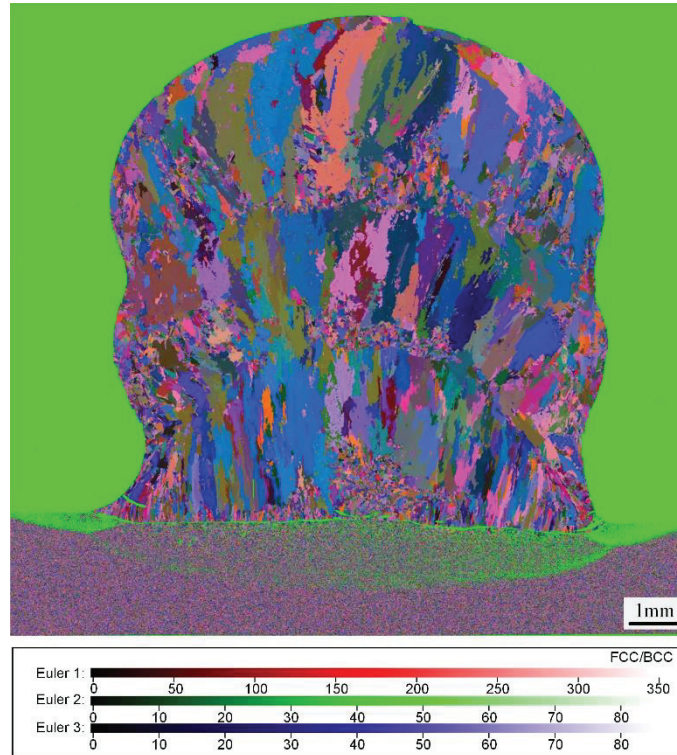


Figure 4-9. Total Euler angle diagram in the cross-section of the three-layer sample.

Another feature can be found in the microstructure diagram. As the number of layers increases, the grain size becomes larger and larger, as presented in Fig. 4-7. The difference in grain size in the cladding layer can be intuitively observed in the grain size diagram, as concluded in Fig. 4-10. This figure is based on the measured data by using EBSD post-processing software. The color changes in the picture represent the different grain sizes, with red representing the largest grain size and blue representing the smallest grain size. The grain size in each area of the cladding layer can be intuitively seen in the figure. Along the structural direction, the higher the number of layers, the larger the grain size. In the interior of each cladding layer, the grain size is large as it is closer to the center and small as it is closer to the edge. As mentioned before, the heat inside the cladding layer was mainly transferred by heat conduction, therefore, the closer to the substrate, the faster the heat conduction and the smaller the grain size. The third cladding layer is farthest from the substrate and has the slowest

heat transfer.

In addition, the substrate and initial cladding layer temperature gradually increased and the heat transfer rate decreased, leading to the lower average cooling rate due to the heat accumulation during the cladding process. The slow cooling rate provided sufficient time for grain growth, resulting in larger grain size and more equiaxed grain morphology. What's more, as mentioned earlier, the heat in the rectangular diode laser heat source was not uniformly distributed inside the rectangle, it is high in the central region and low in the edge region. For the cladding layer, the heat input in the central region of the cladding layer is higher than that in the edge region, and the heat transfer time to the substrate is longer, resulting in the larger grain size.

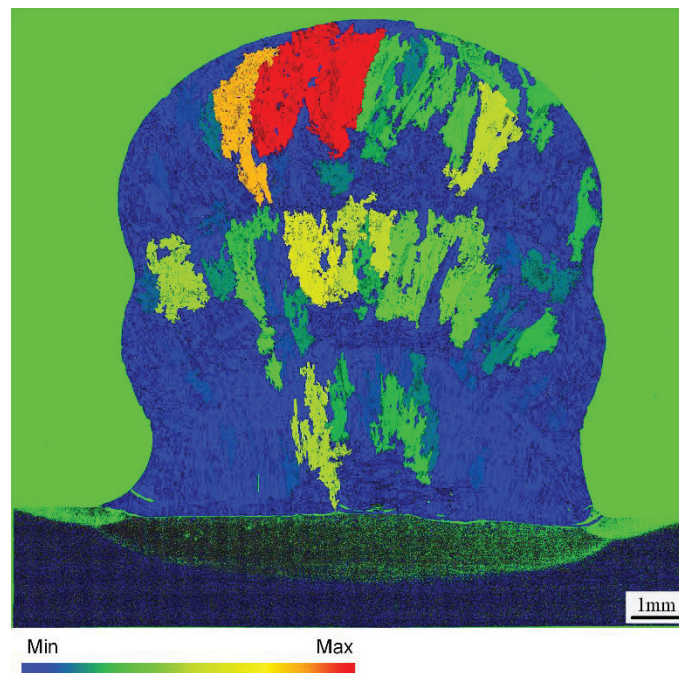


Figure 4-10. Grain size distribution in the cross-section of the three-layer sample.

4.4 Summary

In this study, temperature field simulations of the LHWC process were carried out using a heat source model specifically designed for rectangular laser heat sources. The thermal cycle curves of specific regions and temperature changes during solidification were obtained. The results showed that the heat was mainly transferred downward by heat conduction during the cooling of the cladding layer. The cooling rate was different

at different locations, and the temperature of the edge area dropped faster, in other words, the cooling rate was faster, resulting in different solidified structures. By combining the simulated temperature field with the experimental microstructure, it could be seen that the temperature gradient at the edge of the coating was the largest, consequently, the coating edge area is dominated by columnar crystals. From the edge to the center, the temperature gradient became smaller and smaller and gradually reached the boundary of CET; the microstructure gradually turned to be dominated by equiaxed crystals. In addition, the influence of temperature field on solidification microstructure was also discussed. The results showed that equiaxed crystals were concentrated in the center of the cladding layer, the preferred orientation of crystals was weak, and the grain size was larger. In contrast, the edge region with more columnar crystals had the stronger selective orientation but the smaller crystal size.

4.5 References

- [1] M. Ma, Z. Wang, D. Wang, X. Zeng, Control of shape and performance for direct laser fabrication of precision large-scale metal parts with 316L Stainless Steel, *Optics & Laser Technology* 45 (2013) 209-216.
- [2] M.S.F. de Lima, S. Sankaré, Microstructure and mechanical behavior of laser additive manufactured AISI 316 stainless steel stringers, *Materials & Design* 55 (2014) 526-532.
- [3] R. Sun, Y. Shi, X. Wang, Y. Guo, X. Zhou, Investigation of laser assisted ultra-high frequency induction deposition method: Processes, fluid flow, and microstructure characteristic, *Journal of Materials Research and Technology* 9(3) (2020) 2773-2792.
- [4] S. Wei, G. Wang, Y.C. Shin, Y. Rong, Comprehensive modeling of transport phenomena in laser hot-wire deposition process, *International Journal of Heat and Mass Transfer* 125 (2018) 1356-1368.
- [5] N. Li, S. Huang, G. Zhang, R. Qin, W. Liu, H. Xiong, G. Shi, J. Blackburn, Progress in additive manufacturing on new materials: A review, *J. Mater. Sci. Technol.* 35(2) (2019) 242-269.

- [6] W. Li, X. Liu, M. Yamamoto, Y. Guo, S. Zhu, K. Sugio, G. Sasaki, Research on interface characteristics of 308L stainless steel coatings manufactured by laser hot wire cladding, *Surface and Coatings Technology* 427 (2021) 127822.
- [7] P. Wen, Z. Feng, S. Zheng, Formation quality optimization of laser hot wire cladding for repairing martensite precipitation hardening stainless steel, *Optics & Laser Technology* 65 (2015) 180-188.
- [8] H. Jiang, C. Watanabe, H. Miura, N. Muramatsu, Microstructure and Mechanical Properties of the Heterogeneous-Nano Structured Cu–Be System Alloys, *Materials Transactions* 63(1) (2022) 21-26.
- [9] Z. Nie, G. Wang, J.D. McGuffin-Cawley, B. Narayanan, S. Zhang, D. Schwam, M. Kottman, Y. Rong, Experimental study and modeling of H13 steel deposition using laser hot-wire additive manufacturing, *Journal of Materials Processing Technology* 235 (2016) 171-186.
- [10] T.M. Yue, T. Li, Solidification Behaviour and the Evolution of Microstructure in the Laser Cladding of Aluminium on Magnesium Substrate, *Materials Transactions* 48(5) (2007) 1064-1069.
- [11] S.-H. Sun, T. Ishimoto, K. Hagihara, Y. Tsutsumi, T. Hanawa, T. Nakano, Excellent mechanical and corrosion properties of austenitic stainless steel with a unique crystallographic lamellar microstructure via selective laser melting, *Scripta Materialia* 159 (2019) 89-93.
- [12] Y.M. Wang, T. Voisin, J.T. McKeown, J. Ye, N.P. Calta, Z. Li, Z. Zeng, Y. Zhang, W. Chen, T.T. Roehling, R.T. Ott, M.K. Santala, Philip J. Depond, M.J. Matthews, A.V. Hamza, T. Zhu, Additively manufactured hierarchical stainless steels with high strength and ductility, *Nature Materials* 17(1) (2018) 63-71.
- [13] N. Tamanna, R. Crouch, S. Naher, Progress in numerical simulation of the laser cladding process, *Optics and Lasers in Engineering* 122 (2019) 151-163.
- [14] B. Song, T. Yu, X. Jiang, W. Xi, X. Lin, Development mechanism and solidification morphology of molten pool generated by laser cladding, *International Journal of Thermal Sciences* 159 (2021) 106579.

- [15] S. Dai, D.-w. Zuo, C. Fang, L. Zhu, H. Cheng, Y.-x. Gao, W.-w. Li, Characteration of Laser Cladded Fe-Mn-Cr Alloy Coatings Modified by Plasma Nitriding, *Materials Transactions* 57(4) (2016) 539-543.
- [16] S. Tekumalla, B. Selvarajou, S. Raman, S. Gao, M. Seita, The role of the solidification structure on orientation-dependent hardness in stainless steel 316L produced by laser powder bed fusion, *Mater. Sci. Eng., A* 833 (2022) 142493.
- [17] M. Luo, Y.C. Shin, Vision-based weld pool boundary extraction and width measurement during keyhole fiber laser welding, *Optics and Lasers in Engineering* 64 (2015) 59-70.
- [18] Q. Shi, D. Gu, M. Xia, S. Cao, T. Rong, Effects of laser processing parameters on thermal behavior and melting/solidification mechanism during selective laser melting of TiC/Inconel 718 composites, *Optics & Laser Technology* 84 (2016) 9-22.
- [19] Z. Gan, H. Liu, S. Li, X. He, G. Yu, Modeling of thermal behavior and mass transport in multi-layer laser additive manufacturing of Ni-based alloy on cast iron, *International Journal of Heat and Mass Transfer* 111 (2017) 709-722.
- [20] W.-X. Wu, L. Qu, B.-Y. Liu, W.-W. Zhang, N. Wang, X.-Q. Yu, Lipase-catalyzed synthesis of acid-degradable poly(β -thioether ester) and poly(β -thioether ester-co-lactone) copolymers, *Polymer* 59 (2015) 187-193.
- [21] P. Zuo, S. Chen, M. Wei, J. Liang, C. Liu, M. Wang, Thermal behavior and grain evolution of 24CrNiMoY alloy steel prepared by pre-laid laser cladding technology, *Optics & Laser Technology* 119 (2019) 105613.
- [22] J. Li, H.N. Li, Z. Liao, D. Axinte, Analytical modelling of full single-track profile in wire-fed laser cladding, *Journal of Materials Processing Technology* 290 (2021) 116978.
- [23] T. Mukherjee, W. Zhang, T. DebRoy, An improved prediction of residual stresses and distortion in additive manufacturing, *Computational Materials Science* 126 (2017) 360-372.
- [24] S. Wei, G. Wang, J. Yu, Y. Rong, Competitive failure analysis on tensile fracture of laser-deposited material for martensitic stainless steel, *Materials & Design* 118 (2017) 1-10.

- [25] P. Liu, X. Cui, J. Deng, S. Li, Z. Li, L. Chen, Investigation of thermal responses during metallic additive manufacturing using a “Tri-Prism” finite element method, *International Journal of Thermal Sciences* 136 (2019) 217-229.
- [26] H. Zhao, G. Zhang, Z. Yin, L. Wu, A 3D dynamic analysis of thermal behavior during single-pass multi-layer weld-based rapid prototyping, *Journal of Materials Processing Technology* 211(3) (2011) 488-495.
- [27] G. Chen, X. Shu, J. Liu, B. Zhang, J. Feng, Crystallographic texture and mechanical properties by electron beam freeform fabrication of copper/steel gradient composite materials, *Vacuum* 171 (2020).
- [28] W. Li, K. Sugio, X. Liu, M. Yamamoto, Y. Guo, S. Zhu, G. Sasaki, Microstructure evolution and mechanical properties of 308L stainless steel coatings fabricated by laser hot wire cladding, *Mater. Sci. Eng., A* 824 (2021) 141825.
- [29] Z. Liu, Z. Wang, Effect of substrate preset temperature on crystal growth and microstructure formation in laser powder deposition of single-crystal superalloy, *J. Mater. Sci. Technol.* 34(11) (2018) 2116-2124.
- [30] M. Groeber, S. Ghosh, M.D. Uchic, D.M. Dimiduk, A framework for automated analysis and simulation of 3D polycrystalline microstructures.: Part 1: Statistical characterization, *Acta Materialia* 56(6) (2008) 1257-1273.
- [31] K. Lücke, J. Pospiech, K.H. Virnich, J. Jura, On the problem of the reproduction of the true orientation distribution from pole figures, *Acta Metallurgica* 29(1) (1981) 167-185.
- [32] P. Guo, B. Zou, C. Huang, H. Gao, Study on microstructure, mechanical properties and machinability of efficiently additive manufactured AISI 316L stainless steel by high-power direct laser deposition, *Journal of Materials Processing Technology* 240 (2017) 12-22.

Conclusions

In this study, multi-layer 308L stainless steel samples were prepared using the LHWC technique. To comprehensively evaluate the samples, OM, EBSD, and other characterization techniques were used to determine the microstructure and crystal orientation of the whole sample section. The microstructure evolution of the matrix, HAZ, and the cladding layer, as well as the mechanical properties such as hardness and tensile properties of the multi-layer sample, were studied in detail. The solidification process was simulated in combination with numerical simulation techniques to determine the solidification mode of 308L stainless steel coating. In addition, the connection between microstructure and mechanical properties was explored, revealing the microstructure evolution law during the LHWC process. This study provides the theoretical basis for the 308L stainless steel coating application. The conclusions of this thesis are summarized as follows:

- 1) The surface of the 308L stainless steel coating sample prepared by LHWC technology under appropriate process parameters was smooth. The height of the HAZ was 1.58mm. The height of the cladding layer was 11.84mm. The metallurgical bonding between the substrate and the cladding layer was good, proving the stability and reliability of the LHWC process. The 308L cladding layer consists mainly of dendritic austenite and columnar austenite, with δ -ferrite (content: 9%) distributed between the austenite grains. Equiaxed crystals are generated in the central region, and most of the columnar dendritic morphology in the edge region is located along the structural direction. From the bottom of the first layer to the top of the third layer, the grain morphology showed periodic changes. Inside each layer, columnar dendrites grew along the structural direction. The crystal morphologies of the coating from the bottom to the top was plane crystal, columnar dendritic, and equiaxed grain. Both FA mode and AF mode exist

in the cladding layer, and FA mode is the primary solidification mode. The coexistence of FA mode and AF mode is caused by the cladding layer's different cooling rates and element segregation during solidification.

- 2) The interior of the cladding layer was mainly composed of columnar austenite grains that grew along the structural direction. 60% of the grains had a size larger than $19.7\mu\text{m}$, and the preferred orientation of the crystals in the cladding layer was evident. The matrix and the HAZ were refined equiaxed grains, with more than 60% concentrated below $16.2\mu\text{m}$, and the crystal orientations were randomly distributed without obviously preferred orientations. A large number of LAGBs were gathered near the fusion line of the HAZ and each cladding layer, which increased the strength macroscopically.
- 3) The microstructure of the HAZ region consists mainly of ferrite and tempered bainite. Slatted martensite produced by recrystallization can be observed in the part near the interface, and the presence of martensite can be inferred both from the Schaeffler diagram and the EBSD data; The element migration at the interface not only enhances the transformation of martensite but also leads to a smaller grain size of HAZ. No martensite was found in the substrate far away from the interface.
- 4) The HAZ of the sample had the highest hardness, while the matrix had the lowest hardness. The hardness was higher in the layer-to-layer fusion zone, and then gradually decreased with the increase of the cladding height inside each layer. The elongation of the cladding layer (44.8%) was higher than that of the fusion zone (32.1%) and matrix (20.4%). The tensile strength of the fusion zone was the highest, which was 585MPa. From the dimples in the sample section, it could be concluded that the fracture form of the sample from the matrix to the cladding layer was ductile fracture. Using the Hall-Petch relationship to establish the correlation between the material's microstructure (grain size) and mechanical properties (yield strength). The CRSS law proves the relationship between texture and yield behavior of metal materials, thus proving the influence of microstructure on mechanical properties.

- 5) The thermal cycle curves of specific regions and temperature changes during solidification were obtained. The results showed that the heat was mainly transferred downward by heat conduction during the cooling of the cladding layer. The cooling rate was different at different locations, and the temperature of the edge area dropped faster, in other words, the cooling rate was faster, resulting in different solidified structures. By combining the simulated temperature field with the experimental microstructure, it could be seen that the temperature gradient at the edge of the coating was the largest, consequently, the coating edge area is dominated by columnar crystals. From the edge to the center, the temperature gradient became smaller and smaller and gradually reached the boundary of CET; the microstructure gradually turned to be dominated by equiaxed crystals. In addition, the equiaxed crystals were concentrated in the center of the cladding layer, the preferred orientation of crystals was weak, and the grain size was larger. In contrast, the edge region with more columnar crystals had the stronger selective orientation but the smaller crystal size.

Acknowledgments

I would like to express my sincere gratitude to Professor Gen Sasaki for his guidance throughout this study. He gave me much positive help in the research, the scholarship application, and my personal life. I am also greatly indebted to Professor Motomichi Yamamoto. He gave me important support in my research, which played an important role in my professional and personal development. In addition, I want to express my heartfelt thanks to Professor Kazuhiro Matsugi, Assistant Professor Kenjiro Sugio, and Assistant Professor Yongbum Chio at Hiroshima University and Professor Xingang Liu at Yanshan University for their technical advice and experimental assistance.

Then, I would like to thank my wife, Dr. Ying Guo. It was her company, support, and encouragement from the beginning to the end that kept me motivated to finish my doctoral program. Moreover, I would like to thank all the past and present members of the Materials physics Laboratory in the Department of Mechanical Physical Engineering, Hiroshima University, for their enthusiastic help to my life and study. Special thanks to Dr. Wenchuang Liu, Dr. Song Zhu, Dr. Yan Zhao, Dr. Zixiang Qiu, and Dr. Di Wu.

Finally, I would like to thank Professor Sasaki again for his help in my research and my family for their support. I also owe my sincere gratitude to my friends who gave me their help and time in helping me work out my problems during the challenging course of the thesis.

Published Papers in Regards to This Thesis

1. Wenquan Li, Kenjiro Sugio, Xingang Liu, Motomichi Yamamoto, Ying Guo, Song Zhu, Gen Sasaki, Microstructure evolution and mechanical properties of 308L stainless steel coatings fabricated by laser hot wire cladding, *Materials Science and Engineering: A*, 824,2021,141825. (Chapter 2)
2. Wenquan Li, Xingang Liu, Motomichi Yamamoto, Ying Guo, Song Zhu, Kenjiro Sugio, Gen Sasaki, Research on interface characteristics of 308L stainless steel coatings manufactured by laser hot wire cladding, *Surface and Coatings Technology*, 427,2021,127822. (Chapter 3)
3. Wenquan Li, Pengwei Liu, Xingang Liu, Yingjie Zhao, Motomichi Yamamoto, Song Zhu, Kenjiro Sugio, Gen Sasaki, Temperature field simulation and solidification structure during laser hot wire cladding process. *Processing of the 202 International Conference on Materials Science and Engineering (CoMSE 2022)*. (2022). (Chapter 4)

Presentations

1. Microstructures evolution and mechanical properties of 308L stainless steel coatings fabricated by hot wire laser cladding with wire, Li Wenguan, Sugio Kenjiro, Yamamoto Motoichi, Guo Ying, Zhu Song, Sasaki Gen, 日本金属学会第 168 回講演大会, 2021 年 03 月 16 日, 通常, 英語, 日本金属学会, WEB, プレゼンテーション
2. Temperature field simulation and solidification structure during laser hot wire cladding process, Wenquan Li, Pengwei Liu, Xingang Liu, Yingjie Zhao, Motomichi Yamamoto, Song Zhu, Kenjiro Sugio, Gen Sasaki, the 2022 International Conference on Materials Science and Engineering (CoMSE 2022) , March 20, 2022. WEB, Oral presentation, Shanghai,China.